AN ABSTRACT OF THE DISSERTATION OF

Nurcan Keskin for the degree of Doctor of Philosophy in Electrical and Computer Engineering presented on March 24, 2017.

Title: RF Front End Tuning Methods for Wireless Power Transfer Systems.

Abstract approved: _____

Huaping Liu

Wireless power transfer (WPT) is a way to transfer power from one device to another without any wire or cable connections. Although the technology has been around for more than 100 years, it is gaining popularity in recent years due to the ever-increasing demand for faster and more frequent charging of various consumer electronics devices such as electric vehicles, medical implants, and wireless sensors.

Due to their relatively high-power transfer efficiency, freedom of movement and radio-frequency (RF) safety concerns, loosely coupled, inductive, wireless power-transfer technologies are the most promising category of battery-operated devices. Though tightly coupled systems with well-established design rules and system parameters have been used in industry and discussed in literature for decades, the same does not hold for loosely coupled systems. The system is a complex system with dynamic parameters that may require sophisticated control and tuning features.

This dissertation presents various studies of loosely coupled, wireless power-transfer systems, specifically in RF front end.

RF Front End Tuning Methods for Wireless Power Transfer Systems

by

Nurcan Keskin

A DISSERTATION

submitted to

Oregon State University

in partial fulfillment of
the requirements for the
degree of

Doctor of Philosophy

Presented March 24, 2017
Commencement June, 2017

Doctor of Philosophy dissertation of Nurcan Keskin presented on March 24, 2017.

APPROVED:

Major Professor, representing Electrical and Computer Engineering

---

Director of the School of Electrical Engineering and Computer Science

---

Dean of the Graduate School

I understand that my dissertation will become part of the permanent collection of Oregon State University libraries. My signature below authorizes release of my dissertation to any reader upon request.

Nurcan Keskin, Author

ACKNOWLEDGEMENTS

I wish to express my sincere appreciation to those who have supported me in one way or the other during this amazing journey.

I would like express my sincere gratitude to my advisor Professor Huaping Liu for his continuous encouragement and support of my Ph.D. study and related research, for his patience, and motivation.

Beside my advisor, I would like to thank rest of committee members: Prof.Temes, Prof.Hamdaoui, Prof.Zhang and Prof.Coop for their insightful comments, discussions, and time.

I thank Nicole Thompson, Graduate Coordinator at EECS, for her tremendous support and help.

I would like to thank two of my close friends Zeynep (PhD) and Aylin (PhD), they were the ones who gave me courage to continue and finish my study when times it felt like it was impossible.

I would like to express my deepest gratitude to my husband Mustafa Keskin for his endless technical discussions and support. He has been a constant source of strength and inspiration. It was his constant encouragement that ultimately made it possible for me to see this project through to the end.

I especially thank my mom, dad and sister. I know I always have my family to count on when times are rough.

Last but not least, my boys…Baha and Bera, they are the joy of life.

CONTRIBUTION OF AUTHORS

Wireless power transfer have been increasingly popular in a variety of consumer electronic applications such as sensor charging, implantable device charging, wearable electronics, tablet as well as smart phone charging.

Wireless power transfer system contains mainly receiver and transmitter blocks. These blocks contain different RF and analog circuits such as amplifiers, driver circuits, rectifiers, dc-to-dc converters, and antenna devices. One of the challenging research problems is to transfer power from the transmitter to the receiver efficiently.

The goal of this research is to propose, analyze, and implement new system and circuit level solutions to improve efficiency of wireless power transfer. These solutions are critical for future portable electronic systems such as internet of things. The main issue is to improve matching of RF front end devices between the transmitter and the receiver.

In this research, there are four topics covered. The main part of this research has focused on tuning of antennas by using hybrid capacitor networks. Utilization of different capacitor devices allowed designers to tune continuously or discretely with varactor or weighted capacitors. Second and third topics are still related to tuning of wireless power transfer system specifically with unit antenna arrays and complementary Class-E amplifiers. Finally, last research topic is to produce a novel wireless power charger system for battery charging.

After the system level studies and simulations, hybrid capacitor structure is implemented and tested in the lab to show greater tuning range even in the presence of misalignment or device mismatches.

TABLE OF CONTENTS

Page

TABLE OF CONTENTS (Continued)

Page

TABLE OF CONTENTS (Continued)

Page

LIST OF FIGURES

Figure Page

LIST OF FIGURES (Continued)

Figure Page

LIST OF FIGURES (Continued)

Figure Page

LIST OF FIGURES (Continued)

Figure Page

LIST OF FIGURES (Continued)

Figure Page

LIST OF TABLES

Table Page

1. Introduction

Battery-operated, power-hungry consumer electronics such as smart phones, tablets, laptops, digital cameras, and wearables with different adapters and cables have raised the possibility of wireless power transfer (also known as wireless charging). If the technology finds its way into the consumer market, it will provide a platform for easy, convenient, and simple charging for all.

In addition to consumer electronics, wireless power transfer (WPT) has a wide spectrum of applications such as medical implants, electric vehicles, electric toothbrushes, wireless sensors, and so on.

Research into most wireless power-transfer technologies focuses on power transfer efficiency, auto/self-tuning (due to different load conditions), and multi-receiver structures.

1.1 History of Wireless Power Transfer

In the early 1800s, Andre-Marie Ampere showed that an electric current produces a magnetic field, and Michael Faraday showed that changing magnetic flux is able to induce an electromagnetic force in a conductor. In the late 1800s, James Clerk Maxwell synthesized Ampere's and Faraday's Laws with his own contributions into Maxwell's equations, thereby combining electricity, magnetism, and optics into one unified, consistent theory, which is the basis of classical electromagnetic theory. Heinrich Rudolf Hertz discovered radio waves in 1888 and thereby confirmed Maxwell's theorem.

Based on the foundations of Ampere, Faraday, Maxwell, and Hertz, Nicola Tesla theorized about and experimented with wireless power transfer in 1899 when he powered a fluorescent lamp 25 miles away from the power source without the use of cables.

Unfortunately, Tesla's discoveries were cut short for security reasons and his personal financial problems.

Due to the lack of a device technology that could generate sufficient power (especially microwave power) or handle rectification, there were no significant developments in the area of wireless power transfer (WPT) until World War II. During the war, with the invention of radar, it was shown that point-to-point microwave power transmission is possible. In the 1960s, William C. Brown invented the rectenna, which converts microwaves to direct current (DC). He was able to demonstrate that, with use of a rectenna, a helicopter can be powered thorough microwaves. Later, a printed circuit board (PCB) version of the rectenna was used for the Stationary High Altitude Relay Platform. The purpose of the program was to develop an unmanned aircraft powered by microwave power. Towards the end of 1960s, the first cordless electrical toothbrushes were introduced by General Electrics for the consumer electronics market.

In the early 1970s, induction cookers were introduced in which a coil of copper wire is excited with alternating current (AC) passing through it. The oscillating magnetic field induced a magnetic flux that repeatedly magnetized a cooking pot (made out of ferromagnetic material) that behaved like one single, large coil. Large eddy currents were created in the pot, and because of the pot's own resistance, they heated it up. Induction cookers operate in a low-frequency (LF) band with operation frequencies changing from 20 to 100 kHz.

In 1992, the Microwave Lifted Airplane eXperiment—which involves a fuel-free airplane—was conducted by Kyoto University in Japan. A phased-array rectenna structure was assembled on the roof of a car. The car drove under the fuel-free airplane with a

microwave beam directed toward the plane, and the plane was controlled and monitored by a computer. The airplane flew approximately 10m above the ground. This was the first-ever field experiment with a phased array.

1.2 Modern Wireless Power Transfer Developments

In 2003, the first laser-powered aircraft was flown by NASA. After releasing a small airplane (of only 11 ounces) from a launching platform, a laser beam aimed at the panels of the plane converted laser wavelength into electricity. The power from the electricity was used to operate an electric motor that spun the propeller of the plane. The plane was flown inside a building to avoid any weather-related issues. Possible applications for laser-beam technology include small, unmanned aircraft, high-altitude planes, and space-based solar panels.

In 2007, Professor Marin Soljacic and a team of researchers from the Massachusetts Institute of Technology (MIT) demonstrated the powering of a 60W light bulb at a 2m distance by using magnetically coupled resonance technology. This technology was later adapted by WiTricity, a wireless power-transfer company, which became one of the supporters of this technology.

At the time of this writing, wireless power-transfer technology is still trying to find its way through various consumer markets. Organizations such as the Wireless Power Consortium (WPC-Qi Standard), Power Matters Alliance, and Alliance for Wireless Power (A4WP) promote technologies such as inductive and resonant coupling, which works at different operational frequencies. In the summer of 2015, The Alliance for Wireless Power (A4WP) and the Power Matters Alliance announced a combined organization called

AirFuel Alliance that aims to create a single multi-mode solution for wireless power transfer that is suitable for hand-held devices.

Even though there have been significant advances in wireless power transmission, commercial use of the technology is not up to speed compared to the vast area of research. This is due to a lack of standardization, to multi-device/mode solutions, to high cost and low efficiency, and to slow charging speeds (compared to wired counterparts).

1.3 Dissertation Outline

Chapter 2 provides background information on wireless power-transfer systems, parameter definitions, and system classifications.

Chapter 3 considers the tuning of a wireless power-transfer system and analyzes varactor-based capacitive tuning supported with simulation results.

Chapter 4 summarizes experimental results for tuning of a WPT system with a varactor-based structure and discusses the differences between simulated and real results.

Chapter 5 explores an application of WPT in a battery-charging system.

Chapter 6 explains other studies of WPT that discuss simulation results.

The Conclusion summarizes the studies and discusses possible future studies of the topic.

2 . Wireless Power-Transfer Systems

This chapter provides necessary background information on wireless power-transfer systems. Important system parameters and system operation are explained.

2.1 System Building Blocks

A wireless power-transfer system consists of three main building blocks as shown in Figure 2.1.

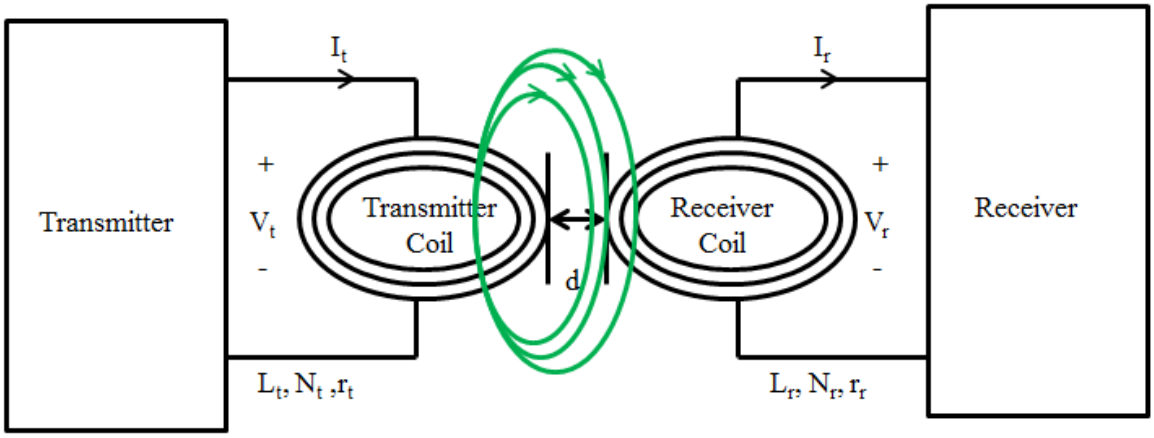

Figure 2-1: Main blocks of a wireless power-transfer system

- The transmitter block might consist of an AC-to-DC conversion block, a driver unit, and power amplifiers for the overall power system. It may also include a controller, and timing blocks such as phase locked loops (PLLs) and digital signal processing (DSP) circuits. It may or may not include some sensory circuits (such as voltage/current sensors) depending on the application and the complexity of the WPT system.
- An energy transfer block consists of both the transmitter and receiver antennas/coils and matching circuitries on both sides.

- The receiver block has an amplifier, a rectifier, and a low-pass filter (LPF) for the power unit in general. A voltage conditioning block such as a regulator may or may not be necessary based on the system. The receiver also has controller and timing circuits.

2.2 Near-Field and Far-Field

Electromagnetic waves have an electric field and a magnetic field component. Interactions of these fields are explained by the Maxwell Equations. The characteristics of these waves change with the distance from the antenna. Near the antenna, both fields exist, although one might be more dominant. Beyond the antenna, fields detach themselves as packets of energy and propagate independently. Multiple boundary definitions are discussed in literature to determine what type of signal occupies the space for a given distance from the antenna. Even though there is no formal definition for the near-field or far-field, both of these two models—the two-region model (near-field and far-field) and the three-region model (near-field, transition field and far-field)—are adapted as explained in [1]. The boundary line definition of near-field for electrically small (compared to wavelength) antennas is less than one wavelength for a given signal, as shown in Equation 2.1.

$$\text{The near-field boundary line} = \frac{\lambda}{2\pi} \tag{2.1}$$

where λ is the wavelength of the signal in meters and can expressed as in Equation 2.2:

$$\lambda = \frac{300}{f_m} \tag{2.2}$$

The constant *300* is the speed of light in meters/second, and f_m is the frequency of the signal in megahertz.

For the two-region model, the region called near-field is inside of this boundary line, and the region called far-field is outside of this boundary line. This concept is illustrated in Figure 2.2.

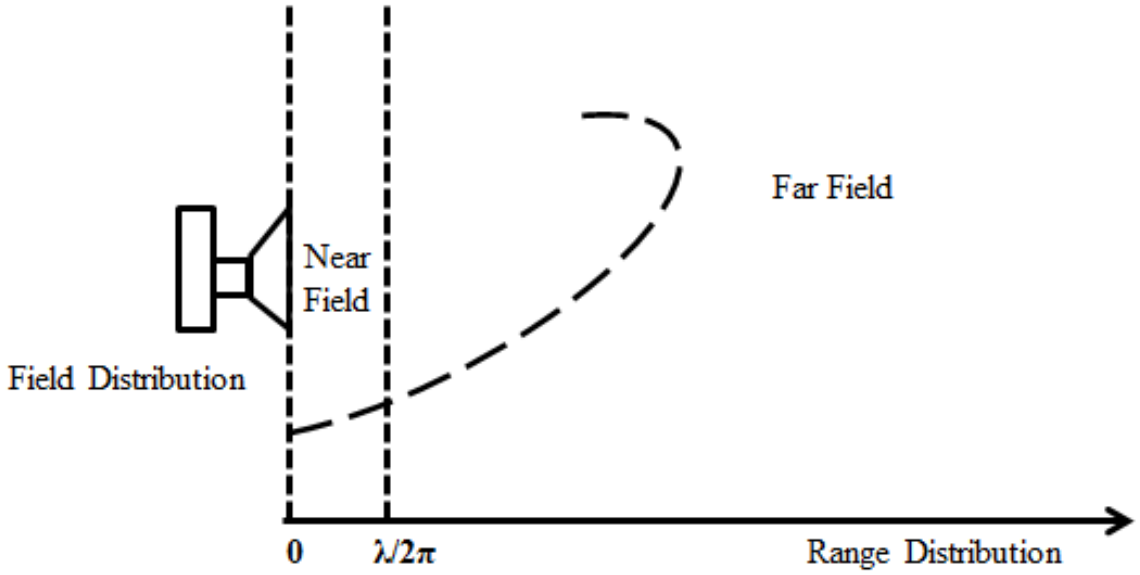

Figure 2-2: Identification of near-field and far-field in the two-region model

Magnetic field strength is stable up to the point of the radius, *r*, of the transmitter coil. As the distance increases, magnetic field strength will decrease exponentially with r^3 in the near-field. This relation is shown in Figure2.3

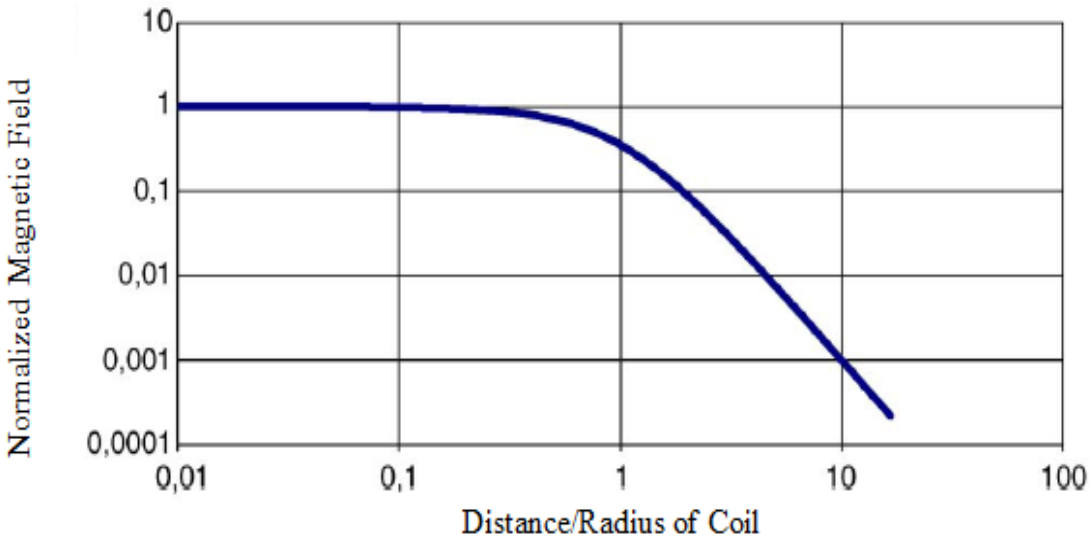

Figure 2-3: Relation between the magnitude of the magnetic field vs. distance/radius ratio

2.3 Categorization of WPT Systems

It is possible to categorize the technology in different ways, including the following:

- Distance (short, medium, long)
- Medium (air, water)
- Sector (consumer electronics, electric vehicle, medical, military and industry applications)
- Technology (laser, solar, electromagnetic radiation, electromagnetic induction)

The main categorization of the technology usually involves the distance between the transmitter and the receiver, as it is the key parameter required to understand the characteristics of the signal and the WPT system. Figure 2.4 shows a categorization of the technology based on distance with respect to the two-region model.

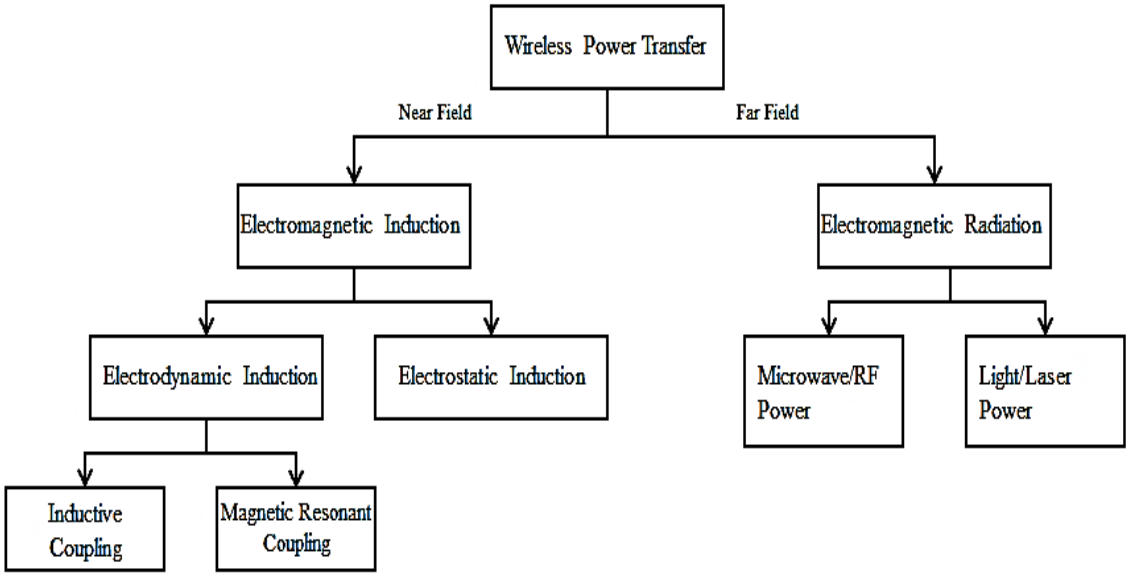

Figure 2-4: Categorization of WPT systems based on distance

Inductive coupling uses the creation of a magnetic field that operates based on a near-field transmission technique in which the operation distance is usually a few centimeters. Inductive coupling can deliver power ranging from a couple of microwatts (mW) to a couple of kilowatts (kW). It is very sensitive to the loading conditions of the receiver, which makes it difficult to design a system that can accommodate multiple receivers. Resonant coupling operates at mid-field, where the distance is couple of meters. Finally, electromagnetic radiation operates in a far-field region where the distance can be a couple of kilometers. Far-field techniques are good candidates for very low-power (less than 100mW) applications because of low efficiency due to RF emission safety regulations. Each method has its own advantages, challenges, and applications. Characteristics of these systems are summarized in the following table.

Table 2-1: Comparison of different wireless technologies

	Inductive Coupling	**Resonant Coupling**	**Electromagnetic Radiation**
Field	Magnetic	Resonance	Electro-magnetic
Method	Coil	Resonator	Antenna
Power	High	High	Low to high
Efficiency	High	High	Low to high
Distance	Short (cm)	Medium (m)	Long (m to km)
Safety	Magnetic	None	EM
Regulation	Under discussion	Under discussion	Radio wave

2.4 Coupled Inductors and Mutual Inductance

A charged coil can create a magnetic field that will induce a current signal in a neighboring coil. Here, coupled inductors are shown in Figure 2.5, where the first coil has N_1 turns and the second coil has N_2 turns. As the current I_1 flows through the coil, it creates a magnetic field of B_1. If the second coil is within the proximity of the first coil, some of the magnetic lines passing through the first coil will also pass through the second coil. The magnetic flux in one turn of the second coil due to current I_1 will be Φ_{21}. Varying I_1 results in varying Φ_{21} and creates an induced electromagnetic force, ε_{21}, in the second coil, as stated in Equation 2.4:

$$\varepsilon_{21} = -N_2 \frac{d\Phi_{21}}{dt} \tag{2.3}$$

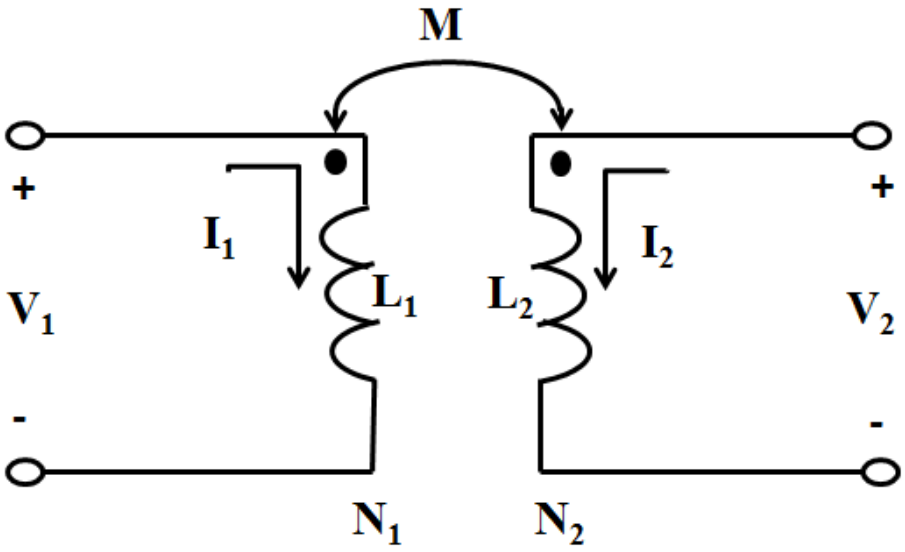

Figure 2-5 : Model of coupled inductors and mutual inductance

Clearly, the time rate of change of Φ_{21} is proportional to the time rate of change of current I_1, as summarized in Equation 2.5:

$$N_2 \frac{d\Phi_{21}}{dt} = M_{21} \frac{dI_1}{dt} \tag{2.4}$$

M_{21} is the mutual inductance between the first and second coils. Mutual inductance mainly dependent on the primary and secondary voltages and co-dependent on geometric properties. The unit of the mutual inductance is in Henry.

Similarly, if there is a changing current, I_2, in the second coil, it will induce an electromagnetic force in the first coil, as in Equation 2.6:

$$\varepsilon_{12} = -N_1 \frac{d\Phi_{12}}{dt} \tag{2.5}$$

Correspondingly, the time rate of change of Φ_{12} is proportional to the time rate of change of current I_2, as summarized in Equation 2.7:

$$N_1 \frac{d\Phi_{12}}{dt} = M_{12} \frac{dI_2}{dt} \quad (2.6)$$

Simply combining Ampere's Law and Bio-Savart's Law under ideal conditions, it can be shown that coupled inductors M_{12} and M_{21} are equal and can be denoted as M.

$$M_{12} = M_{21} = M \quad (2.7)$$

2.5 Coupling Coefficient

The amount of magnetic flux connected from the first coil to the second coil is defined as the coupling coefficient, *k*. The degree of coupling coefficient will determine whether the system is a tightly coupled system (also called strongly coupled or close coupled) or a loosely coupled system. The typical value of a coupling coefficient varies between 0 and 1.

Regular transformers, induction motors, and chargeable electric toothbrushes are good examples of tightly coupled systems in which there is a strong coupling (k>0.5) between the transmitter and receiver. Obviously, this strong coupling will result in power transfer with high efficiency. Strong coupling is achieved by precise alignment of the two coils via mechanical constraint; hence, these systems do not offer freedom of movement.

In loosely coupled systems, there is no iron core between transmitter and receiver. There is a small air gap between them; they are not fixed together, and the coupling coefficient is

low (k<0.1). In contrast to strongly coupled systems, loosely coupled systems provide freedom of movement without the bulky magnetic materials, but they suffer from low power-transfer efficiency. Some of the examples are non-contact vehicle battery chargers, roadway powered electric vehicles and medical implants. A comparison of tightly coupled and loosely coupled systems is shown in Table 2.2.

Table 2-2: Comparison of tightly and loosely coupled systems

Feature	Strongly Coupled Systems	Loosely Coupled Systems
Coupling Factor	k>0.5	k<0.1
Core	Ferrite	Air
Position of T_x vs. R_x	Precise alignment required	Precise alignment not required
Freedom of Movement	Not Available	Available
Efficiency	Strong	Weak
Design	Not complex	Complex

2.6 Leakage Inductance

Any magnetic flux that is not connected from the first coil to the second coil will be lost in the surrounding environment and negatively affect the system's power-transfer capacity. The amount of lost flux is called leakage inductance. As the name implies, it is modeled as an inductive element in the circuit, which is usually connected in series with the self-inductance, as shown in Figure 2.6.

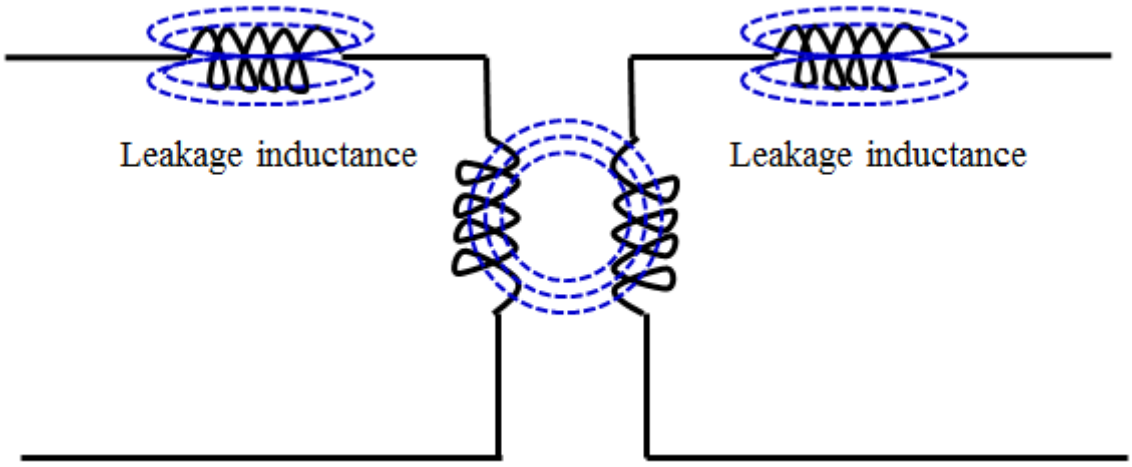

Figure 2-6: Model of leakage inductance in an ideal air-core transformer

Conceivably, the magnitude of leakage inductance in strongly coupled systems is less than that of mutual inductance due to a magnetic core, a tight alignment of transmitter and receiver, and the close proximity of each side. Contrarily, loosely coupled systems suffer from large leakage inductance caused by the substantial air gap between the two sides. The magnitude of the leakage inductance can be fairly large. It can be almost the same as mutual inductance and even bigger in some cases.

2.7 Compensation Topologies

To eliminate the effects of leakage inductance, a capacitor is usually added to the circuit. This additional element is called a compensation capacitor and can be connected in series or in parallel with the self-inductance. This method of adding a compensation capacitor has been applied in power systems for many years and is a well-known technique for overcoming the effects of leakage inductance. There are nine different compensation topologies [2], as shown in Figure 2.7. Based on the application or the complexity of the

system, compensation may or may not be used or both the series and parallel compensations may be used in a combined switchable configuration.

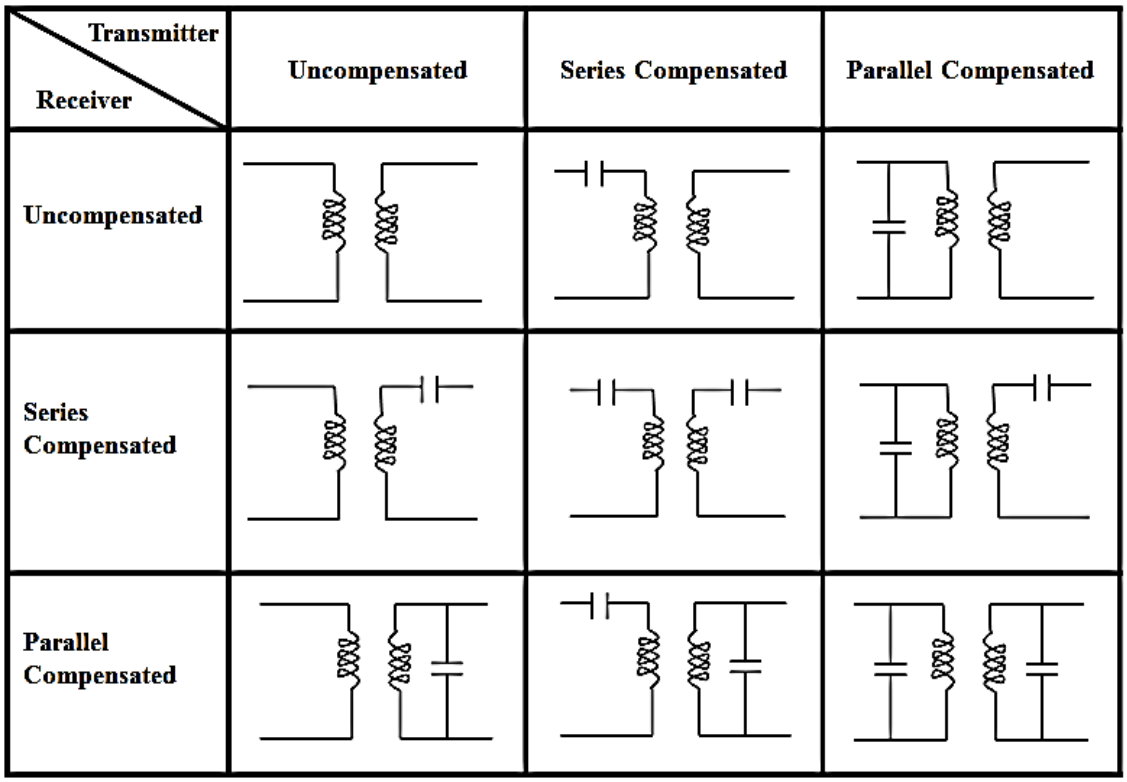

Figure 2-7: Compensation configurations for WPT systems

2.8 Resonance

Fundamentally, resonance causes an object to vibrate with a larger amplitude when the energy of a certain frequency is applied. In WPTS, resonant inductive coupling occurs when both transmitter and receiver antennas are tuned to the same frequency of resonance. Numerous studies [3] [4] [5] [6] compare different compensation topologies and the effects of resonance. Even though there are some cases in which resonance may not be the most

critical parameter for the system [7], it is shown that, for most topologies, transfer efficiencies can be one of the most critical parameters when the resonance occurs between transmitter and receiver.

2.9 Quality Factor

The quality factor (*Q*) of an inductor can be defined as the ratio of its inductive reactance to its serial equivalent resistance at a particular frequency. It can also be defined as the energy loss due to the resistance of the inductor. This loss reduces the amount of energy stored within the inductor. It is a dimensionless parameter, and in most cases, the high *Q* is desired.

The *Q* value for an inductor can be expressed as in Equation 2.9:

$$Q = \frac{X_L}{R} \text{ where } X_L = L * \omega_0 \text{ , } \omega_0 = 2\pi f_L \tag{2.8}$$

For a tuned LC circuit, a *Q* value will change depending on the compensation type of the circuit.

For a parallel compensated circuit, a peak occurs at resonance, and the quality factor can be expressed as in Equation 2.10:

$$Q_p = \frac{1}{R}\sqrt{\frac{C}{L}} \tag{2.9}$$

For a series-compensated circuit, a dip occurs at resonance, and the quality factor can be expressed as in Equation 2.11:

$$Q_s = \frac{1}{R}\sqrt{\frac{L}{C}} \tag{2.10}$$

2.10 Loosely Coupled Inductive Systems

This section explains a loosely coupled system and its operation basics. As mentioned in earlier sections, a loosely coupled system will have a very low coupling coefficient due both to the lack of a magnetic core between the transmitter and receiver and to the air gap between the two. The size of the receiver coil might be considerably smaller than the transmitter coil, especially for size-limited applications such as medical implants. The selection of an operation frequency can change considerably from kHz (kilohertz) to GHz (gigahertz) based on the application.

2.10.1 System Operation

The basic block diagram of an inductively coupled WPT system is shown in Figure 2.1. In this system, the transmitter drives and excites the transmitter coil with voltage $V_{t,}$ at a specific operation frequency, which creates a current signal I_t. Changing magnetic flux, due to I_t in the transmitter coil will induce a voltage, $V_{r,}$ in the receiver coil. If a load is connected, then I_r starts flowing, which will charge a load (usually a battery). The two coils in proximity form an air-core transformer that works on the principles of inductive coupling in the near-field.

Coupling effects between a transmitter and a receiver can be studied based on three different models: coupled-mode theory, lumped-circuit theory, and reflected-load theory (a mutual inductance model). Coupled-mode theory is suitable for tightly coupled systems in which the leakage inductance is low. Lumped circuit theory is used mostly in mid-range systems where a compensation source is added both in the transmitter and receiver sides. Reflected load theory uses induced and reflected voltages to describe the coupling between

transmitter and receiver. This theory is suitable for loosely coupled inductive systems where leakage inductance can be large; therefore, system's voltage parameters are expressed in terms of mutual inductance, as shown in Equations 2.12-2.14:

$$V_t = j\omega L_t I_t + j\omega M I_r \tag{2.11}$$

$$V_r = j\omega L_r I_r + j\omega M I_t \tag{2.12}$$

$$M = k\sqrt{L_t}L_r \tag{2.13}$$

where,

M is mutual inductance between two coils

k is coupling coefficient

ω is circular frequency

f is operation frequency

V_t is transmitter voltage

V_r is induced voltage in the receiver

I_t is transmitter current

I_r is receiver current

L_t is self-inductance of transmitter coil

L_r is self-inductance of receiver coil

Induced voltages can be increased by increasing the mutual inductance, which is co-dependent on the coupling coefficient. The coupling coefficient is mostly affected by the geometry of the coils. It depends, for example, on their sizes (both individually and relative to each other), the shape of the coils, and their relative orientation of alignment.

The intensity of the magnetic field from the transmitter coil can be varied by changing the number of its turns N_t, the radius of the coil, r_t, and the transmitter current, I_t, as seen in Equation 2.15. Decreasing the distance, d, between the transmitter coil and the receiver coil will also increase the magnitude of magnetic field:

$$H_t = \frac{r_t^2 N_t I_t}{2\sqrt{(d^2 + r_t^2)^3}} \tag{2.14}$$

Designing a robust, loosely coupled inductive system that can transfer energy with high efficiency and with a lateral degree of freedom is very challenging. Adjusting any of the system parameters arbitrarily may result in catastrophic system failures and in damage to the nearby environment.

3 .Tuning of a Wireless Power-Transfer System with a Hybrid Capacitor Array

3.1 Introduction

The optimum system operation point in terms of power transfer has been heavily studied in literature. [8] [9] [10] [11] [12] One important element in this area is the RF front end matching circuitry where either impedance or frequency tuning is achieved through different system architectures.

3.2 Impedance Tuning vs. Frequency Tuning

A resonant-mode WPT system requires dynamic tuning to maintain its resonance. Based on the type of the system—i.e., on whether it is closely coupled or loosely coupled—the selection of tuning technique can change [13]. Closely coupled systems use frequency tuning in which both source and load impedances are fixed and antenna impedances are matched to them for a fixed distance. Frequency is constantly modified to keep the system tuned within this range. Loosely coupled systems benefit from impedance matching in which the capacitive, LC, or a different combination of LC structures are used to adjust the impedance mismatch while keeping the resonant frequency constant as much as possible.

3.3 Variable (Tuning) Capacitors for Radio Frequency Applications

Variable capacitors are used in high-frequency circuits such as voltage-controlled oscillators (VCOs), LC tank circuits, frequency synthesizers, and tunable filters. They are also known as tuning capacitors due to their ability to control signals.

Variable capacitor diodes have been used in electronic circuits since the 1960s. These are types of diodes designed to operate in a reverse-biased state so that DC current flows through the device to control the thickness of the depletion zone and hence the capacitance.

Down scaling of the metal-oxide-semiconductor field-effect-transistor (MOSFET) makes it possible to have an increased number of applications for wireless RF technology [14] [15]. This facilitates single transceiver solutions with limited numbers of external components, which is critical for mobile applications such as smart phones for which space and cost are very critical.

3.3.1 Complementary-Metal-Oxide-Semiconductor (CMOS) Capacitors

There are three categories of capacitors based on CMOS technology. These are the following:

1. P-N junction capacitors
2. Conductor-insulator-conductor capacitors (such as metal-insulator-metal (MIM) caps, polysilicon-oxide-polysilicon (poly-poly) caps)
3. MOSFET gate capacitors

3.3.2 MOS Capacitor

A MOS capacitor is made of a substrate (a semiconductor body), an insulator (usually silicon-dioxide, SiO_2) and a conductor surface (which used to be a kind of metal such as aluminum, but with the latest device technologies, heavily doped, highly conductive polycrystalline silicon placed metals are used). The conductor surface is structured as one of the terminals of the capacitor (the gate) while the connection between source/drain and bulk is the other terminal [16].

3.4 System Properties

A parallel-primary parallel-secondary wireless power-transfer system is studied under no-load conditions (Figure 3.1). The system is assumed to have no resistive losses. A sinewave with a 13.56MHz frequency and a 2V peak-to-peak amplitude is applied to the primary. The self-inductances of primary and secondary antennas (L_p and $L_{s)}$ are both selected as 500nH. Resonance frequency is chosen also as 13.56MHz.

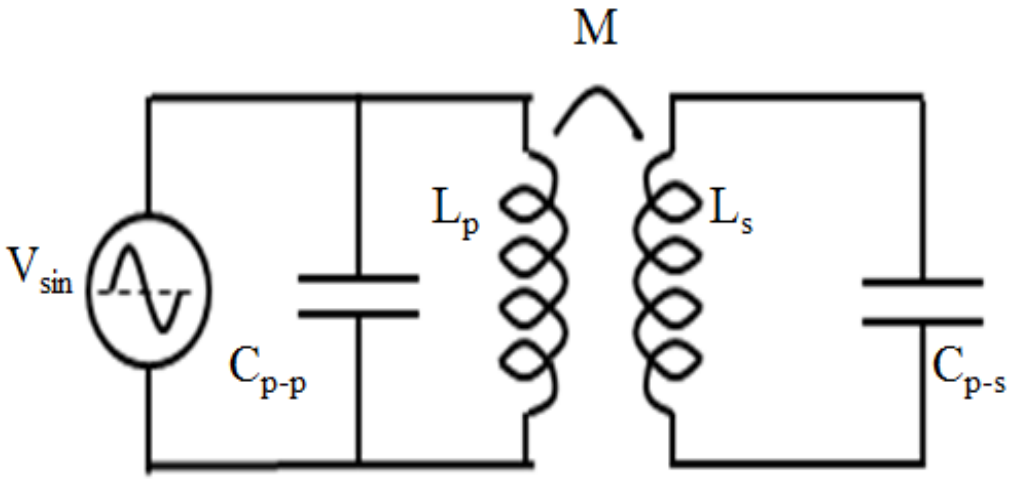

Figure 3-1: Parallel-primary (C_{p-p}) parallel-secondary (C_{p-s}) wpt system

It is assumed that this system is de-tuned from the resonance frequency due to various conditions such as component mismatches, leakage inductance, load variations, and environmental disruptions. The main focus of this study is to understand the impact of different capacitor structures on the re-tuning of the system; hence, how the system de-tuned is outside the scope of this work.

3.5 Proposed System Architecture

In the literature, different capacitive tuning methods such as switchable capacitor arrays or variable capacitor diode structures were used to re-tune a wireless power-transfer system. In our proposed capacitive tuning structure [17], we are combining a high-Q capacitor, a MOSCap variable capacitor, and a switchable capacitor array as a hybrid solution to provide coarse tuning (through a MOSCap) and fine tuning (through a switchable capacitor array), as shown in Figure 3.2.

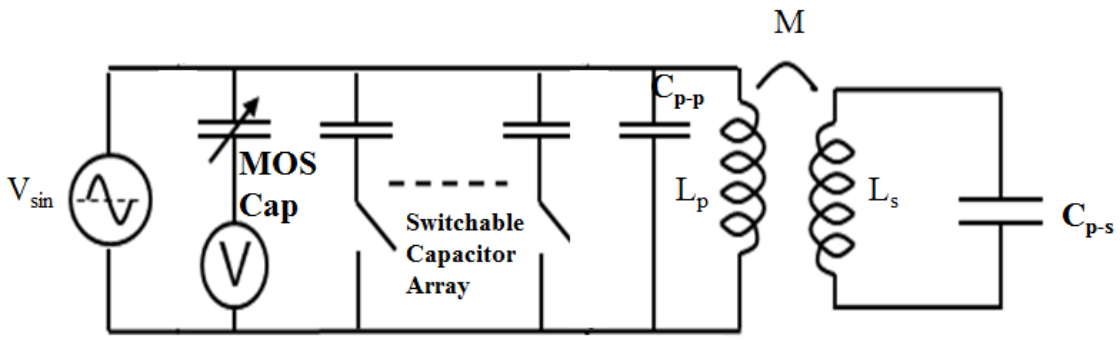

Figure 3-2: Proposed capacitor structure for tuning

In this structure, C_{p-p} is the compensation capacitor in parallel with the self-inductance of primary, $L_{p.}$ This capacitor has the main role of providing a high *Q* value for the circuit, whereas MOSCap and capacitor array will have lower *Q* values due to other component connections.

3.6 Simulation Results

Initial simulations were run to understand the behavior of a MOSCap. The center frequency of the MOSCap is determined by varying the bias voltage from -1V to 1V, as shown in Figure 3.3. Simulation result shows that center frequency can be changed from 11MHz to

almost 15MHz. Simulation results confirm that the desired resonance frequency of 13.56MHz of the proposed system is well within the tuning range of MOSCap.

The range-of-capacitance value is determined by running a simulation in which Vbias is varied as shown in Figure 3.4. The main capacitance value is around 165 pF.

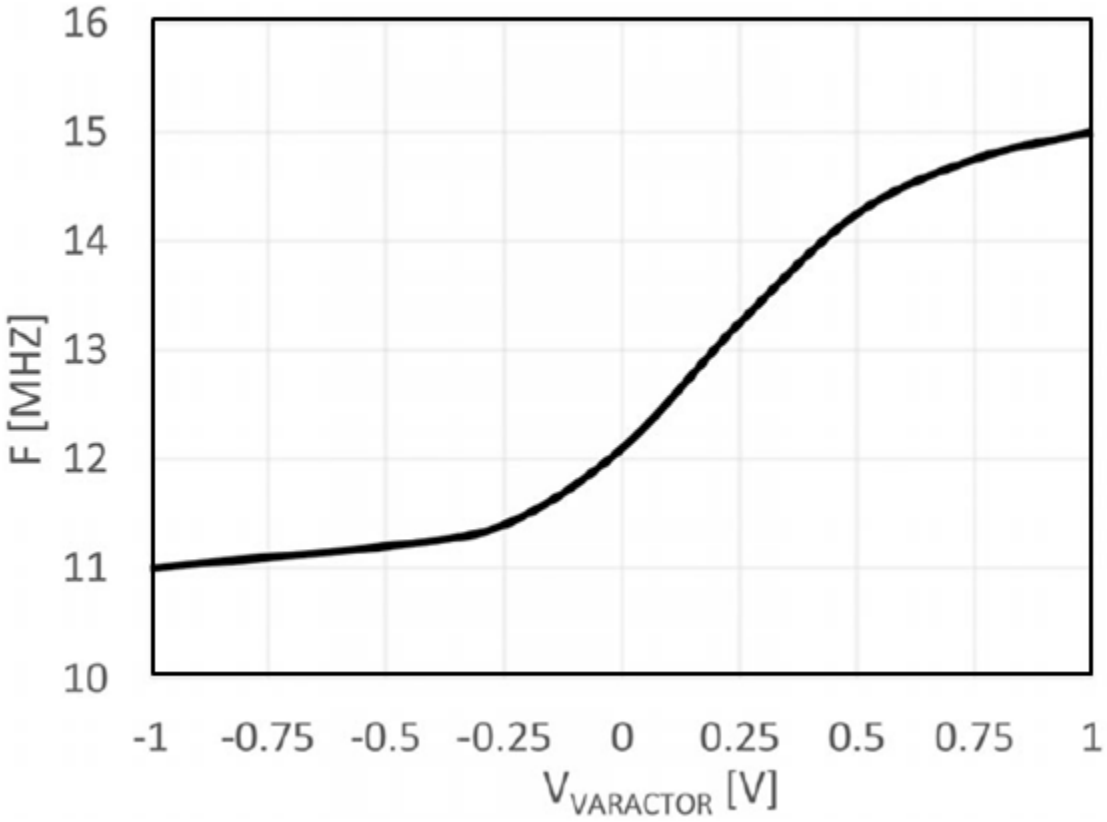

Figure 3-3: Bias voltage vs resonant frequency of MOS Cap

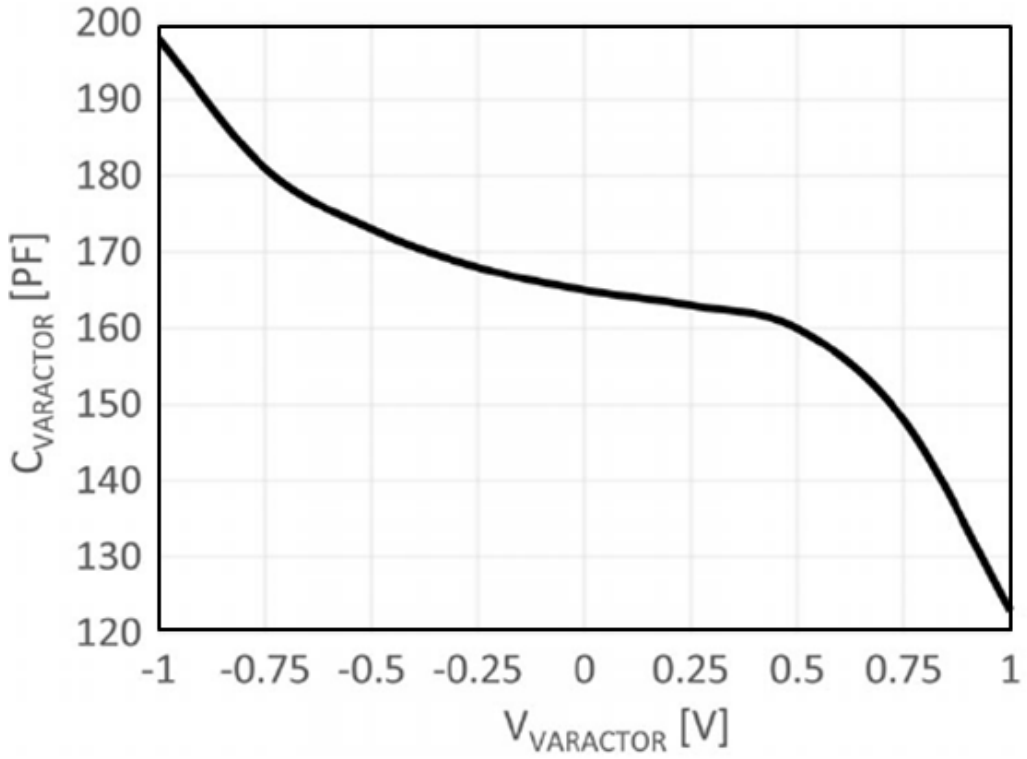

Figure 3-4: Vbias vs. Capacitance of MOSCap

For a linear operation, we need to increase the tunability range of MOSCap beyond 0.7V on the higher side and -0.5V on the lower side of the graph, as seen in Figure 3.3. To achieve this, a weighted capacitor array is included in the circuit. The total capacitance for the new configuration (Equation 3.1) will be as follows:

$$C_{total} = C_p + C_{MOSCap} + C_{array} \tag{3.1}$$

The proposed architecture is simulated to further investigate the tunability range. The bias voltage of MOSCap is varied from -0.5V to 1V, while capacitor arrays are added in four steps as 84pF, 136pF, 188pF, and 240pF. As shown in Figure 3.5, with the proposed hybrid structure, the center frequency can now be varied from 10MHz to 19.4 MHz compared to 11MHz to 15MHz with previous MOSCap only structure.

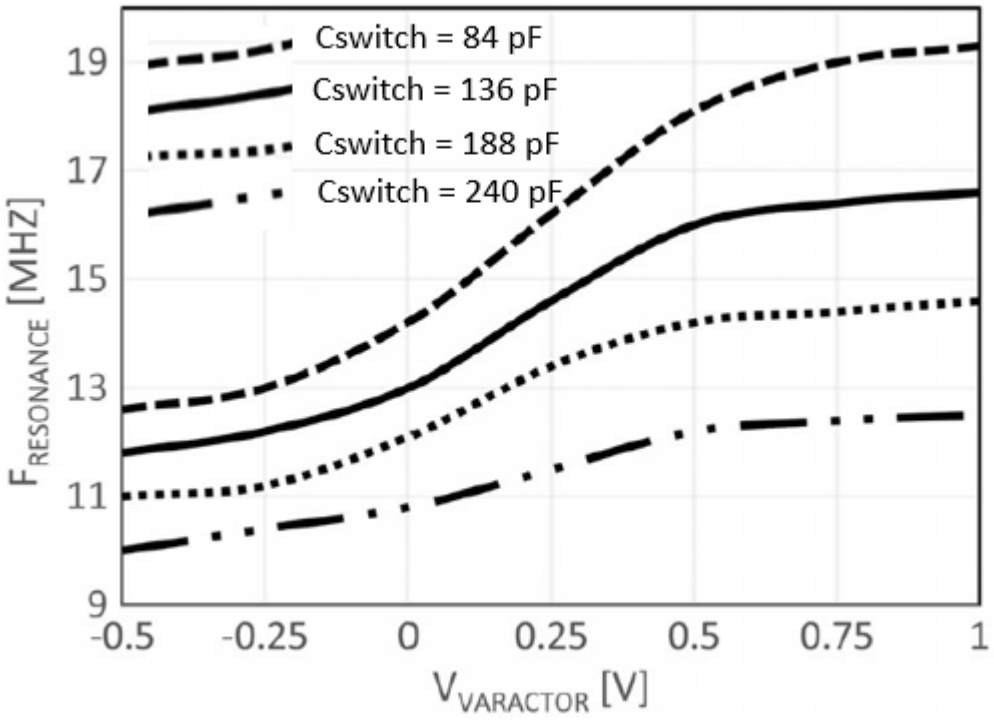

Figure 3-5: Vbias vs. center frequency of proposed hybrid structure

The new structure has several advantages over MOSCap only structure:

1. Tunability range is improved to +/- 35% from +/- 10%.

2. Finer steps for frequency adjustments are achieved with the addition of a capacitor array.

3. Extended range for frequency tuning is obtained with more linear transitioning points.

Figure 3.6 shows the current signal transmitted from the transmitter antenna ($45mA_{pp}$) and the current signal received at the receiver antenna ($5mA_{pp}$). Figure 3.7 shows the voltage at the transmitter antenna ($2V_{pp}$) and the induced voltage at the receiver antenna ($0.2V_{pp}$).

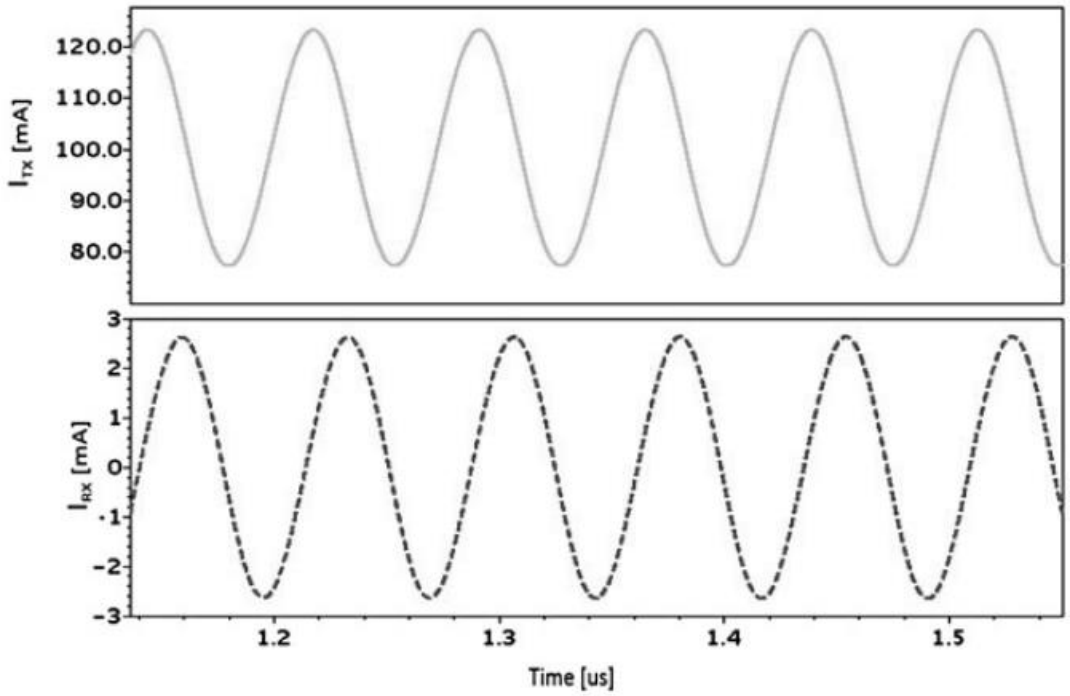

Figure 3-6: Transmitted (top) and received (bottom) current waveforms

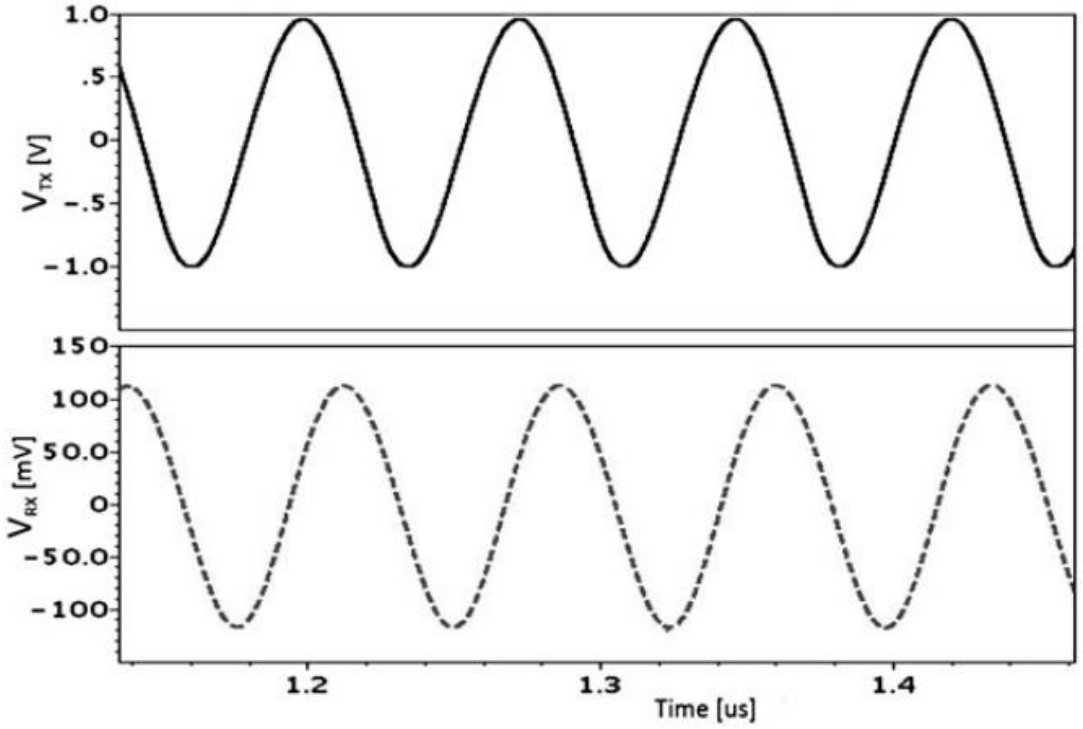

Figure 3-7: Transmitted (top) and received (bottom) voltage waveforms

3.6.1 Detuning of a Wireless Power-transfer system and Simulation Results

Initially, an ideal case of WPT system with no resistive losses is considered the baseline in simulations. Secondly, for de-tuning purposes, to emulate a leakage inductance, an additional 100nH is introduced into the system. This value represents an approximately 20% deviation from the nominal self-inductance of the antenna coil. After the system is de-tuned, the proposed hybrid structure is utilized to re-tune the system back to its resonance frequency. The circuit element values for different transmitter structures are shown in Table 3.1.

Table 3-1: Circuit elements for different cap structures at the transmitter

Circuit	**C_{main} (pF)**	**C_{switch} (pF)**	**$C_{varactor}$ (pF)**	**L_{tx} (nH)**	**$L_{leakage}$ (nH)**	**V (V)**
Baseline	138	-	164	500	-	0
De-tuned	138	-	164	500	100	0
Proposed Structure (re-tuned)	92	46	164	500	100	0.1

Figures 3.8 shows power curves for three different cases when the transmitter is at desired resonance (baseline), de-tuned and re-tuned. It is clear that the proposed structure can be used for de-tuning of the transmitter with an amplitude advantage.

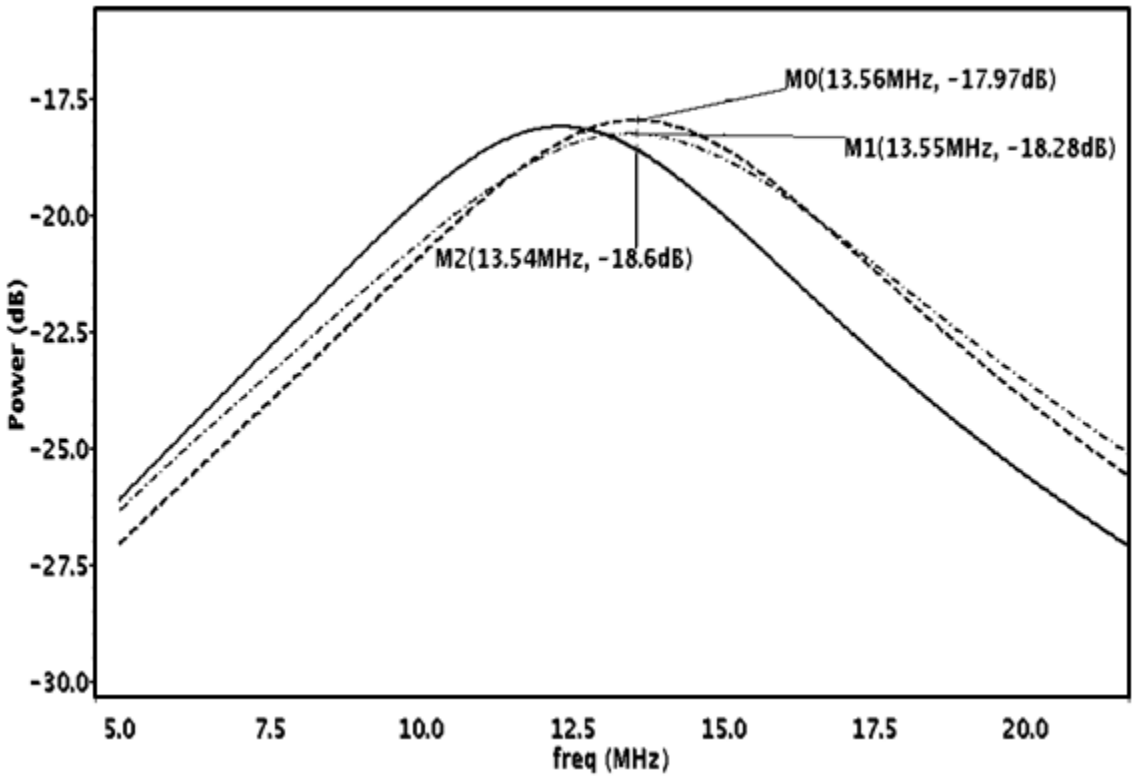

Figure 3-8: Transmitted power curves; baseline (dashed, peak=-17.97dB), de-tuned (solid, value=-18.6dB at 13.54MHz), re-tuned (dashed-dotted, peak=-18.28dB)

Received power signals for k=0.1 are shown in Figure 3.9. For the de-tuned signal, the amplitude of the signal is approximately 0.5 dB lower than the baseline. By using the hybrid structure the signal can be improved in terms of amplitude (only 0.13 dB less than the baseline). The waveform is also improved and it follows the baseline closely.

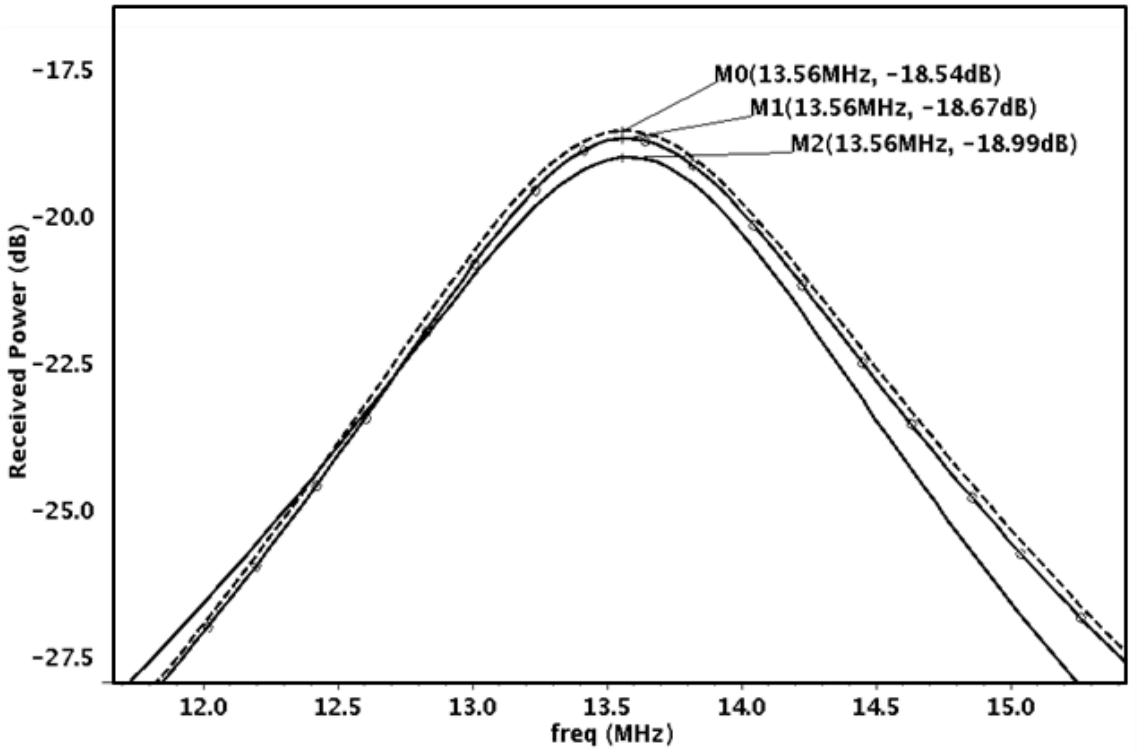

Figure 3-9: Received power curves: baseline (dashed, peak=-18.54dB), de-tuned (solid-lowest peak=-18.99dB), re-tuned (solid-middle peak=-18.67dB) when k=0.1

Another simulation is also run when k=0.01. Obviously, because of a very low coupling coefficient, the amplitudes of the received signals are significantly lower than when k=0.1. The effect of hybrid structure is more dominant, as shown in Figure 3.10.

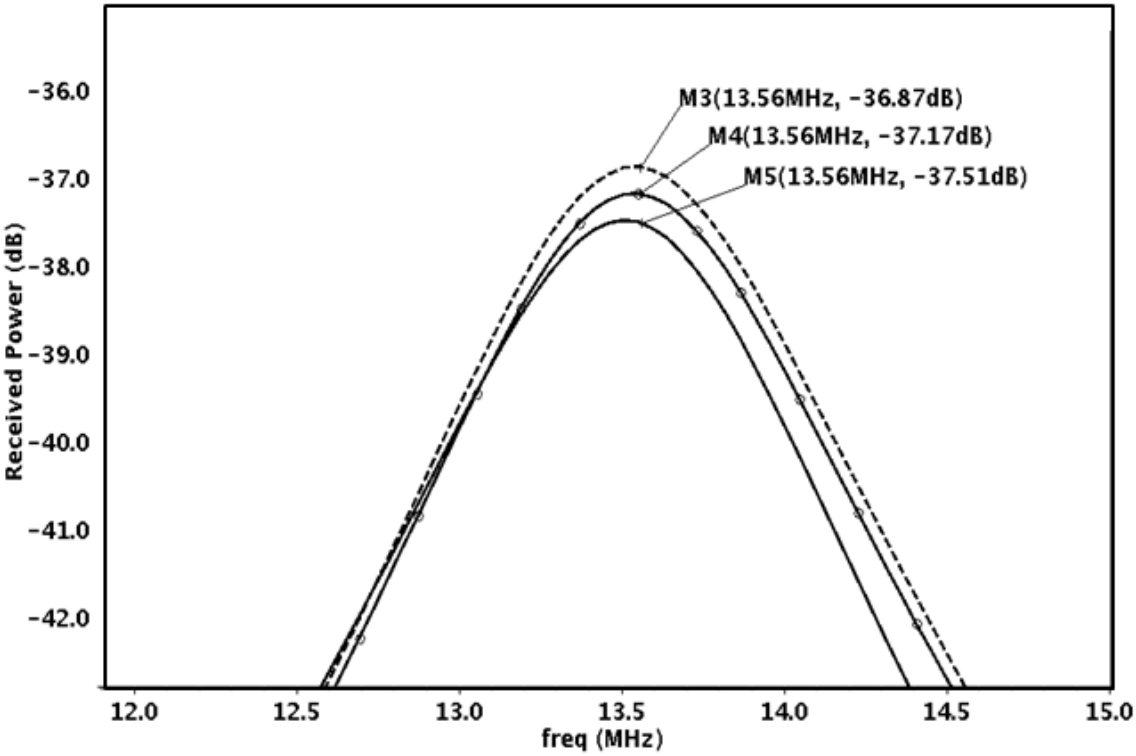

Figure 3-10: Received power curves: baseline (dashed peak=-36.87dB), de-tuned (solid-lowest peak=-37.51dB), re-tuned (solid-middle/circle peak=-37.17dB) when k=0.01

As the next step, the amplitude of leakage inductance is increased from 100nH to 200nH. To find the optimum value, both voltages (0.1-0.2V) of the varactor and also the number (1-6) of binary capacitors are swept, as seen in Figure 3.11. The largest received power is observed when V is equal to 200mV and the number of binary capacitors is 4, which is close to 30pF of the binary cap value for this particular leakage inductance. In this case, received power is improved more than 1 dB, as shown in Figure 3.12.

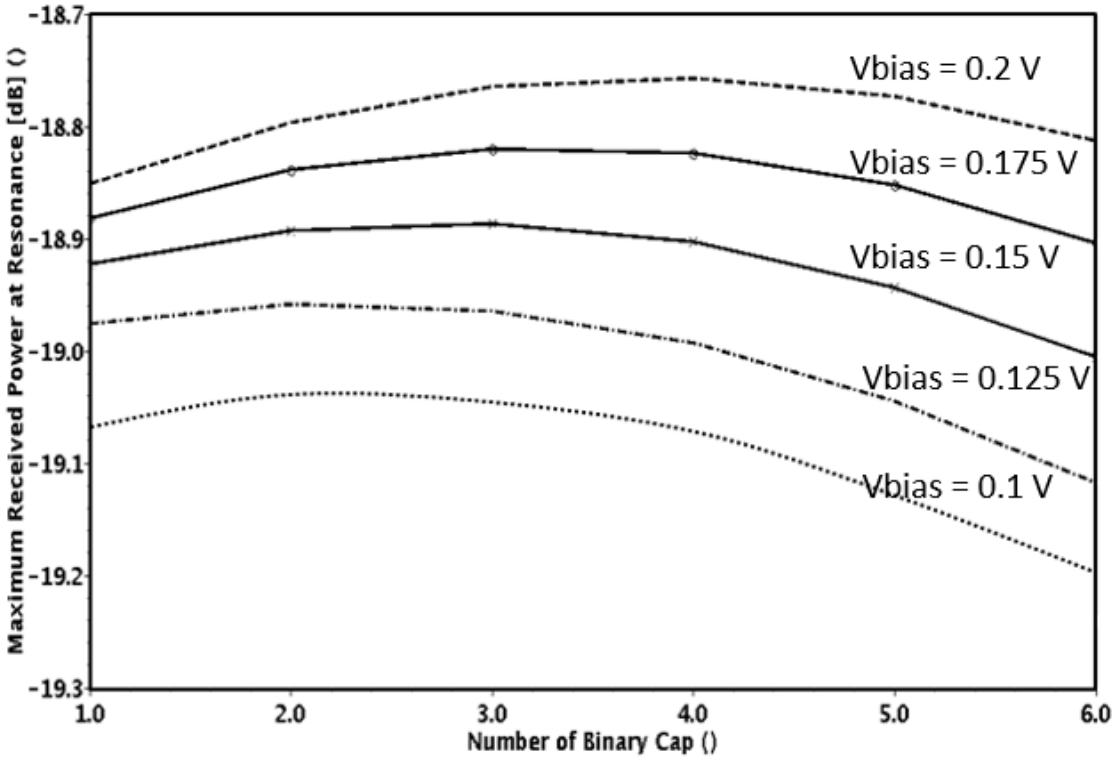

Figure 3-11: Received power of proposed architecture when number of caps in binary array and bias voltage of Varactor (100mV, 125mV, 150mV, 175mV, and 200mV) is varied (k=0.1, $L_{leakage}$=200nH)

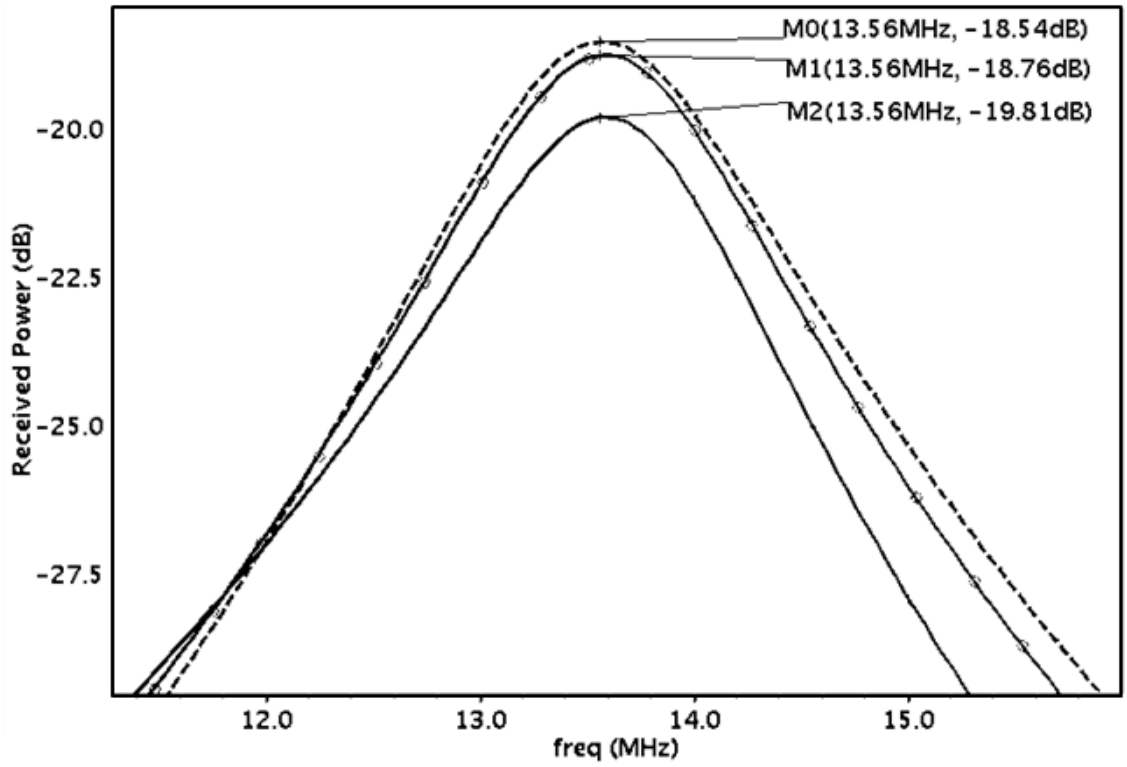

Figure 3-12: Received power curves: baseline (dashed, peak=-18.54dB), de-tuned (solid-lowest peak=-19.81dB), re-tuned (solid-middle/circle peak=-18.76dB) (k=0.1, $L_{leakage}$=200nH)

Different capacitive tuning structures are compared in Table 3.2.

Table 3-2: Comparison of WPT systems with different capacitive tuning structures

Reference	**F_{center} (MHz)**	**Tuning Range**	**C_{main}**	**C_{switch} range**	**C_{MOSCap}**
[8]	13.84	not available	158 pF	95-374 pF	None
[18]	13.56	+/- 46%	213 pF	9-470 pF	none
[19]	2400	+/- 10%	6 pF	none	26-70.7 fF
[20]	0.085	+/- 7%	175 nF	1.6-52 nF	none
[17]	13.56	+/- 35%	92 pF	2184 pF	120-164 pF

4 Experimental Results

4.1 Initial Baseline Components and Measurement Equipment

Experiments are performed on the system that is utilizing discrete components. These discrete components are purchased from various seller sites, such as Fry's Electronics, Digikey, and Amazon.

4.2 Transmitter and Receiver Coils

The most important part of the experiments is the transmitter and receiver coils. For this reason, they are handmade using wires. Two hand-wrapped coils with 26 AWG wire are shown in Figure 4.1.

Figure 4-1 Hand-wrapped transmitter and receiver coils

First, the self-inductances of coils are calculated with an available online calculator after entering several parameters, as seen in Figure 4.2.

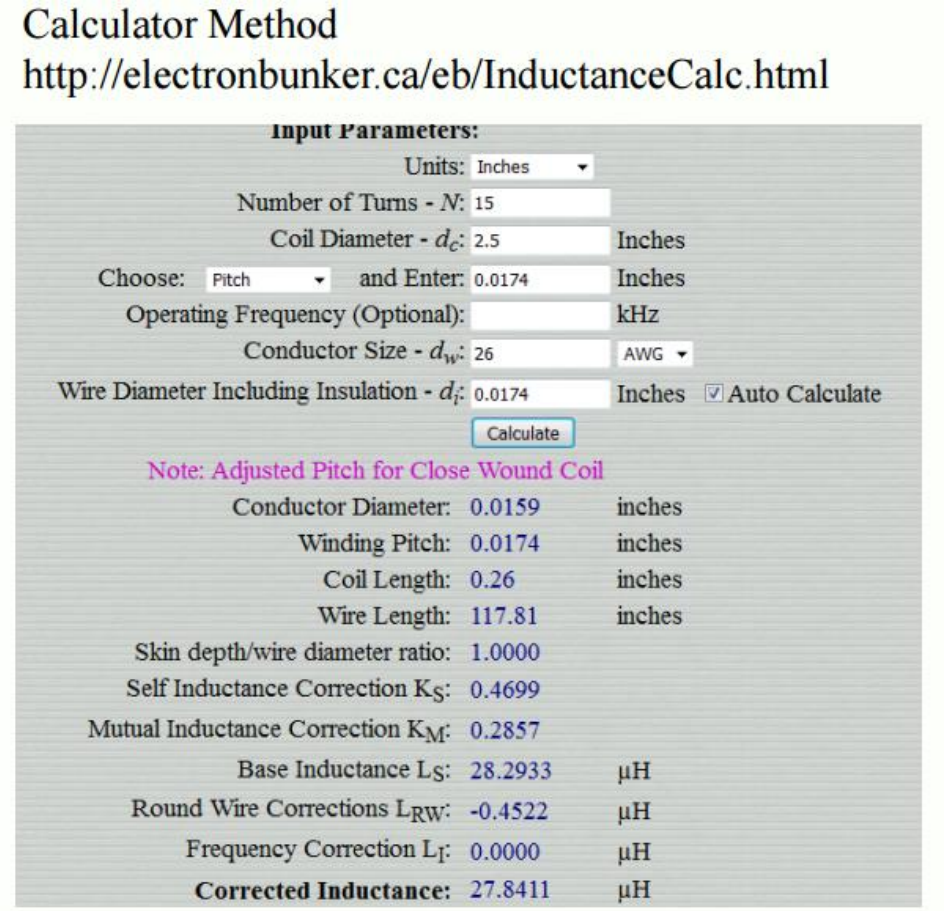

Figure 4-2: Self-Inductance Calculation

Second, as a verification step, self-inductances are measured with an LCR meter (model 885 by BK Precision), as seen in Figure 4.3. Both calculated and measured self-inductances are in agreement. They are approximately 28 µH.

Figure 4-3: Measurement of the self-inductance of the coil with an LCR meter

4.2.1 Measurement Equipment and Others

A Volmate digital LCD voltmeter/ammeter/ohmmeter/Multimeter, AC/DC tester, a SainSmart DDS120 portable/handheld PC-based USB digital storage oscilloscope (20MHz bandwidth 50M/S), a breadboard (in Figure 4.4), and jumper cables are used to set up the experiment.

Figure 4-4: SainSmart USB oscilloscope

4.2.2 IC Discrete Components

NTE955MC CMOS timing circuit is used as shown in Figure 4.5.

NTE955MC
Integrated Circuit
CMOS Timing Circuit

Description:

The NTE955MC is a monolithic timing circuit in an 8–Lead DIP type package fabricated using CMOS process. This timer is fully compatible with CMOS, TTL, and MOS logic and operates at frequencies up to 2MHz. Because of its high impedance, this device uses smaller timing capacitors than those used by the NE555. As a result, more accurate time delays and oscillations are possible. Power consumption is low across the full range of power supply voltage.

Like the NE555, the NTE955MC has a trigger level equal to approximately one–third of the supply voltage and a threshold level equal to approximately two–thirds of the supply voltage. These levels can be altered by use of the control voltage terminal (Pin5). When the trigger input (Pin2) falls below the trigger level, the flip–flop is set and the output goes high. If Pin2 is above the trigger level and the threshold input (Pin6) is above the threshold level, the flip–flop is reset and the output is low. The reset input (Pin4) can override all other inputs and can be used to initiate a new timing cycle. If Pin4 is low, the flip–flop is reset and the output is low. Whenever the output is low, a low–impedance path is provided between the discharge terminal (Pin7) and GND. All unused inputs should be tied to an appropriate logic level to prevent false triggering.

While the CMOS output is capable of sinking over 100mA and sourcing over 10mA, the NTE955MC exhibits greatly reduced supply–current spikes during output transitions. This minimizes the need for the large decoupling capacitors required by the NE555.

Figure 4-5: NTE955MC CMOS timing circuit

NTE Discrete ceramic and variable capacitors from 10pF to 1nF for tuning are used.

The CML Series is a range of radial lead conformally coated non-polarized multilayer ceramic capacitors. These flame retardant capacitors are most commonly used for filtering, coupling, and bypass applications.

RATINGS

Capacitance Range: 10pf to 2.2uf
Voltage: 50VDC and 100VDC

PERFORMANCE SPECIFICATIONS

Operating Temperature Range:

Z5U	+10°C to +85°C
X7R	-55 °C to 125°C
NPO	-55 °C to 125°C

Tolerance Range:

CML103M50 - CML225M50	±20%
CML102K100 - CML154K100	±10%
CML100J100 - CML473J100	±5%

Figure 4-6: Ceramic capacitors

Description:
These diodes are designed for high volume requirements of FM Radio and TV tuning and AFC, general frequency control and tuning applications; providing solid−state reliability in replacement of mechanical tuning methods.

Features:
- High Q with Guaranteed Minimum Values
- Controlled and Uniform Tuning Ratio
- Standard Capacitance Tolerance – 10%

Figure 4-7: Varactor capacitors

4.3 Test Setup

The complete test setup is shown in Figure 4.8. Capacitors and tuning capacitors are placed on the breadboard. A SainSmart USB scope is connected to the USB port of the test computer. This scope has its custom GUI, as shown in the display of the test computer. A simple 9V alkaline battery is used to power the NT955MC IC, which produces a square

wave with a maximum clock frequency of 1MHz. The SainSmart scope has two input ports to measure signals, and these are connected to transmitter and receiver sides. Transmitter (TX) and receiver (RX) coils are separated below for clearer illustration.

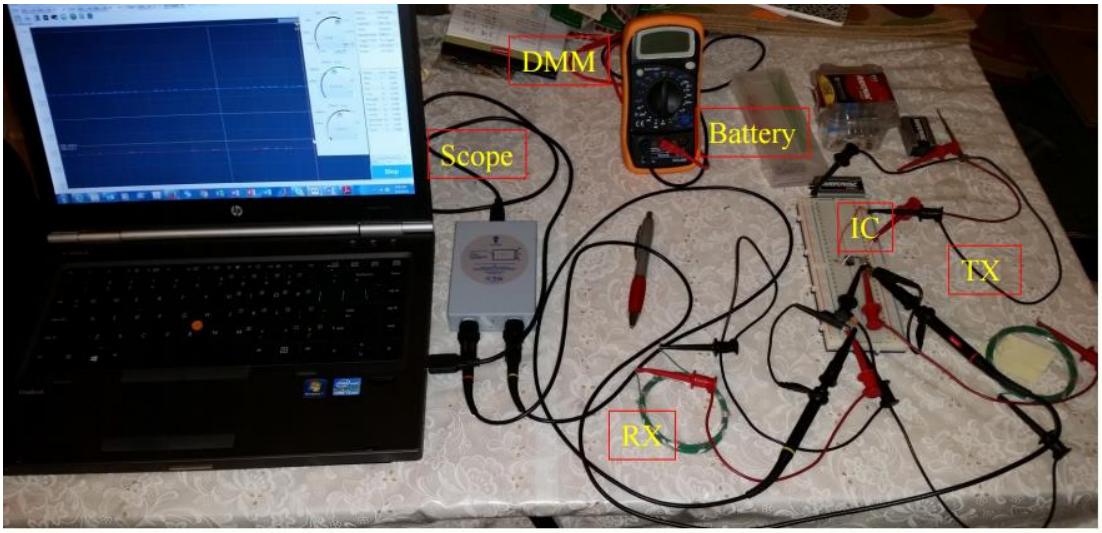

Figure 4-8: Complete test setup (Tx and Rx coils are separated for illustration only)

During the measurements, the antenna coils are placed in close proximity, as shown in Figure 4.9. WPT setup on the breadboard side is shown in Figure 4.10.

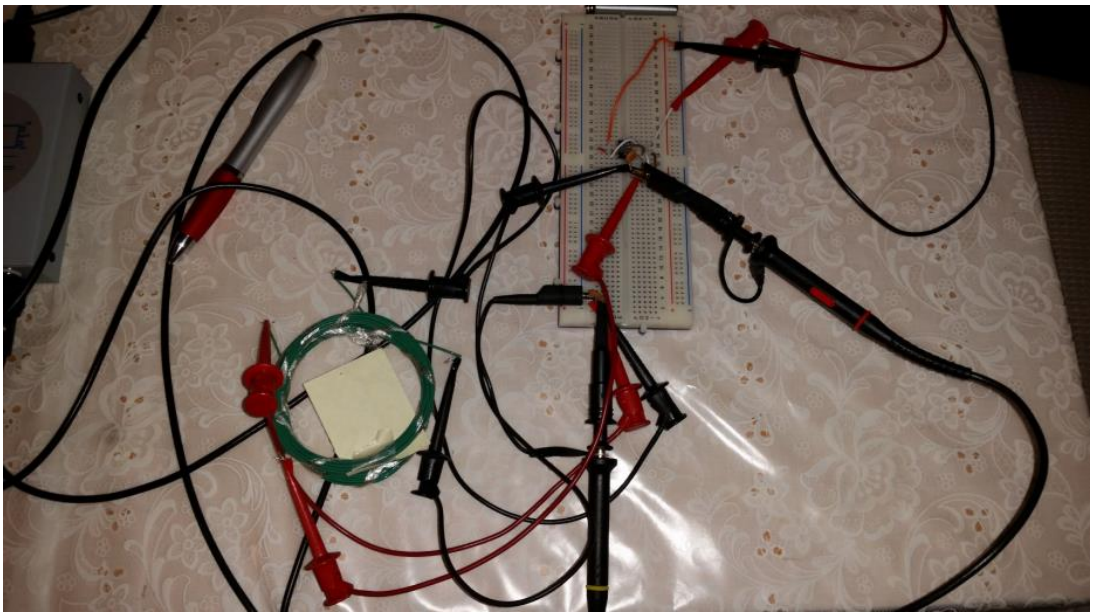

Figure 4-9: Tx and Rx coils are at a distance of d=0 cm

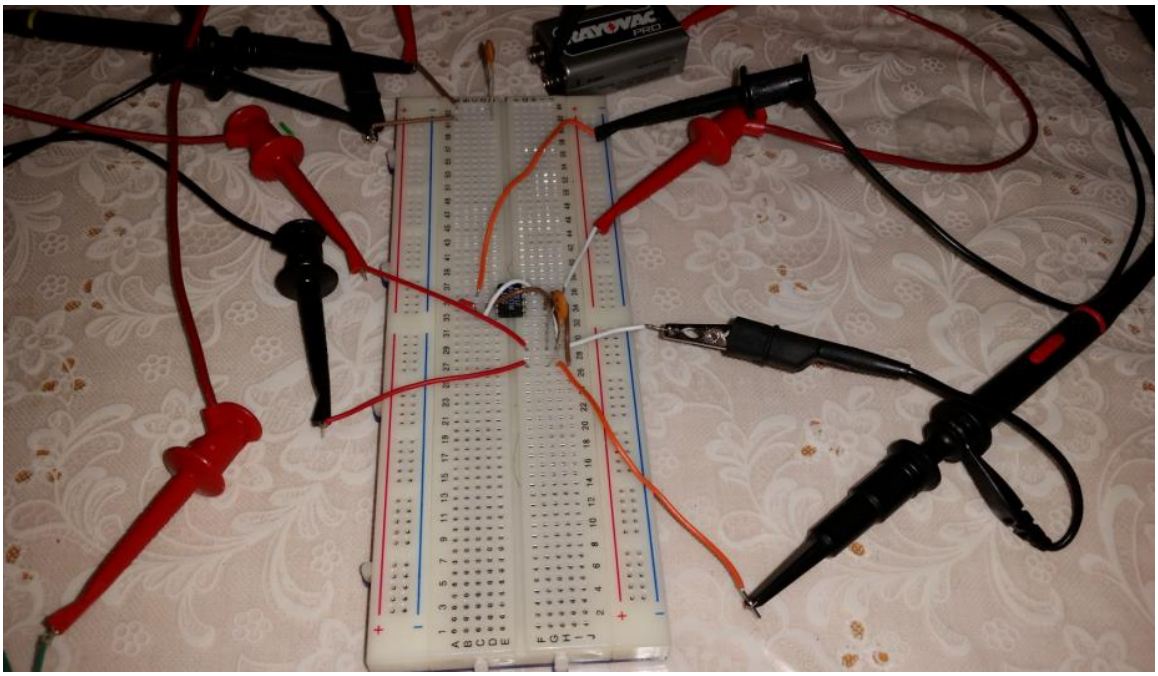

Figure 4-10: Set up on the breadboard

Table 4-1: Experiment Results

Tuning Capacitor (pF)	**Voltage at Receiver (Vpp)**
0	1.1
200	1.16
470	1.29
600	1.32
700	1.12
800	1.05

For initial test results, a self-inductance of 28µH with ~500pF is used for a resonant frequency of ~1MHz. Measurement results also show compliance with the calculations. The NTE614 is used as a varactor with a value of 33pF. As expected, optimum peak resonance occurs between 470pF to 600pF. The received signal decreases beyond this optimum point. The screen capture with both transmitted and received signals is shown in Figure 4.11. As mentioned earlier, NT955MC creates square pulses only; hence, the waveforms are square pulse signals.

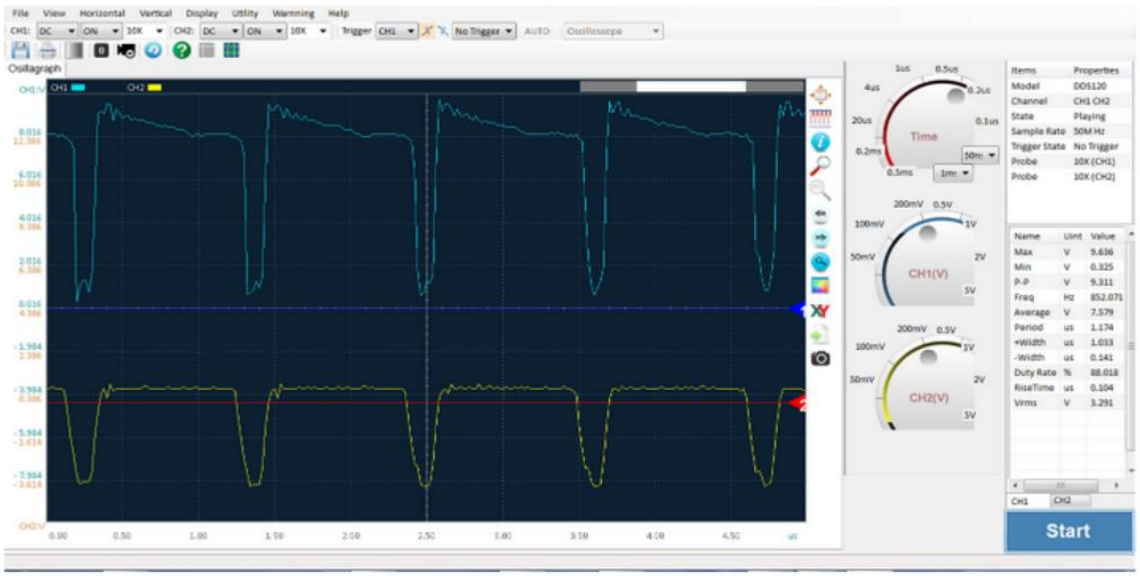

Figure 4-11: Transmitted (up) and received (bottom) voltage waveforms

4.4 Experiment Setup with Lab Equipment

During initial experiments, it is observed that there are limitations due to test equipment in terms of reaching the simulated resonant frequency. For the next phase of the experiments, an RF signal generator, a stand-alone mixed-signal oscilloscope, and a dedicated DC power supply are used.

4.4.1 Baseline Setup

The baseline circuit is set up to resonate at 13.56 MHz. Component values are shown in Table 4.2. New transmitter and receiver antenna coils are wrapped in small diameters consisting of only 2.7 turns. They are calculated to be around ~1.2 µH by using the calculator, as was done previously. Figure 4.12 shows the calculation of the self-inductances.

Round Coil Inductance Calculator

Input Parameters:

Units:	Inches		
Number of Turns - N:	2.7		
Coil Diameter - d_c:	2.3	Inches	
Choose: Pitch and Enter:	0.0174	Inches	
Operating Frequency (Optional):		kHz	
Conductor Size - d_w:	26	AWG	
Wire Diameter Including Insulation - d_i:	0.0174	Inches	Auto Calculate

Calculate

---------- Calculation Successful - No Errors ----------

Conductor Diameter:	0.0159	inches
Winding Pitch:	0.0174	inches
Coil Length:	0.05	inches
Wire Length:	19.51	inches
Skin depth/wire diameter ratio:	1.0000	
Self Inductance Correction K_S:	0.4693	
Mutual Inductance Correction K_M:	0.1536	
Base Inductance L_S:	1.2784	µH
Round Wire Corrections L_{RW}:	-0.0617	µH
Frequency Correction L_I:	0.0000	µH
Corrected Inductance:	1.2167	µH

Figure 4-12: Calculation of self-inductances

Resonant Frequency is calculated as

$$Fres = \frac{1}{2\pi\sqrt{115\text{pF}*1.2\mu\text{H}}} \sim 13.56MHz \quad (4.1)$$

Table 4-2: Baseline circuit elements and values

Component Name	**Component Value**
C_{tx_main}	115 pF
C_{rx_main}	115 pF
L_{tx}	1.2 µH
L_{rx}	1.2 µH
Fres	13.56 MHz
Vin	1.2 V
Vout	0.77 V
Conductor size	26 AWG

This designed wireless power-transfer system is shown in Figure 4.13. In this setup, where coils are aligned at the bottom, the probe at the right side and capacitors are connected to the receiver coil, and the left side coaxial cable and capacitors are connected to the transmitter coil. The RF signal source used to generate the transmitter signal, and the oscilloscope used to measure received signal are shown in Figure 4.14. Finally, measured results are shown in Figure 4.15, which is F_{res} vs. V_{out} at the receiver.

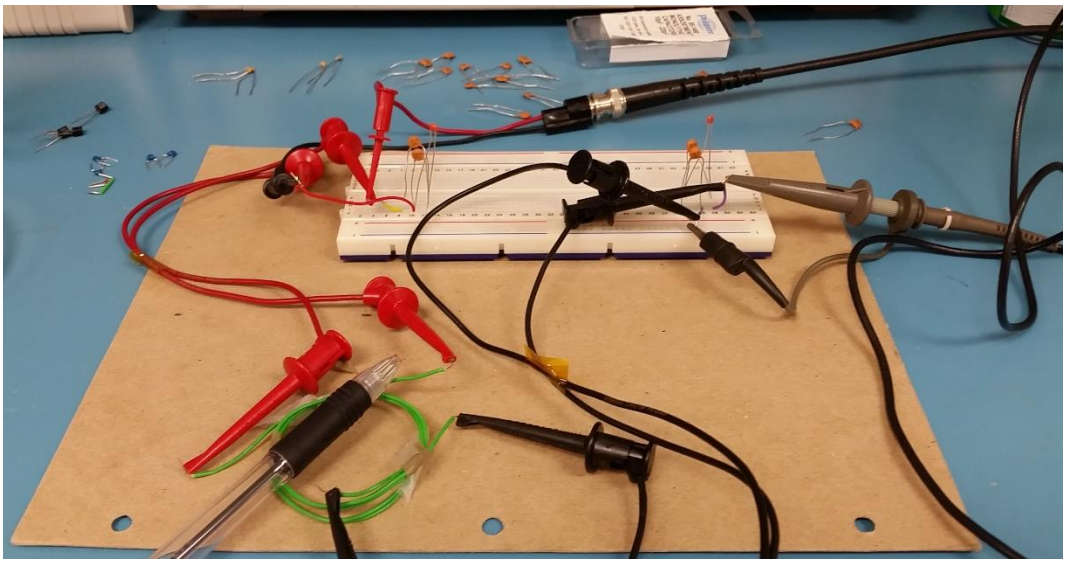

Figure 4-13: Baseline setup for full wireless power-transfer system

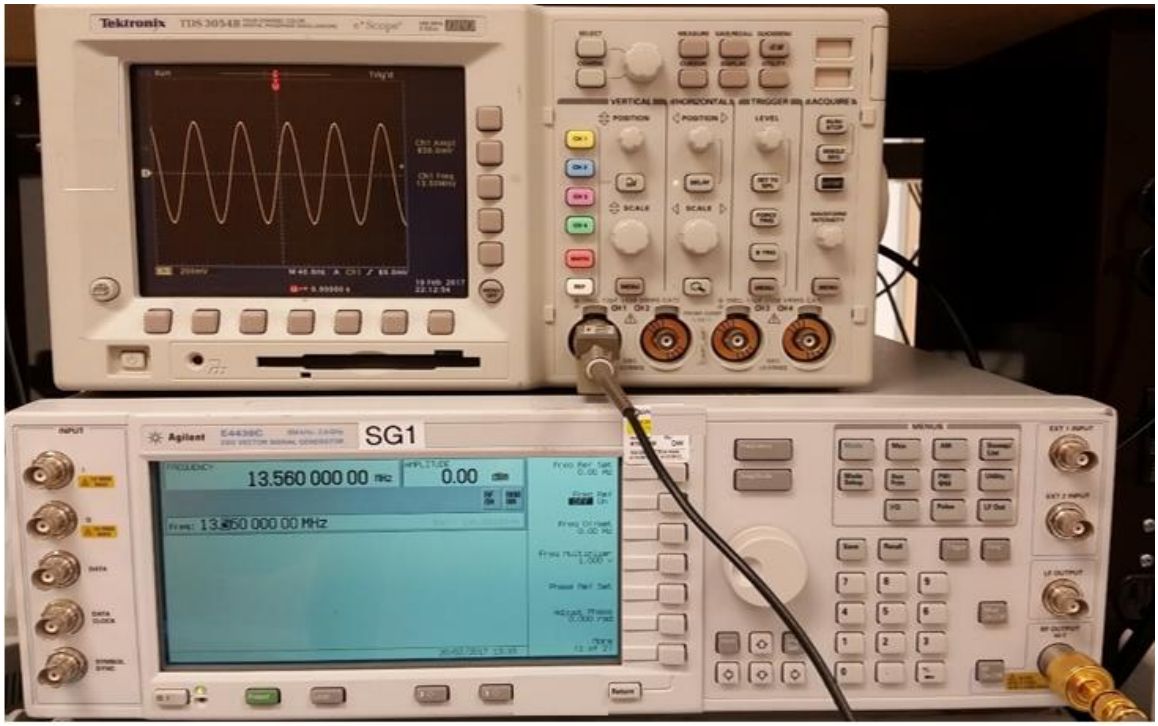

Figure 4-14: Tektronix oscilloscope (top, for received signal) and Agilent RF signal Generator (bottom, for transmitted signal)

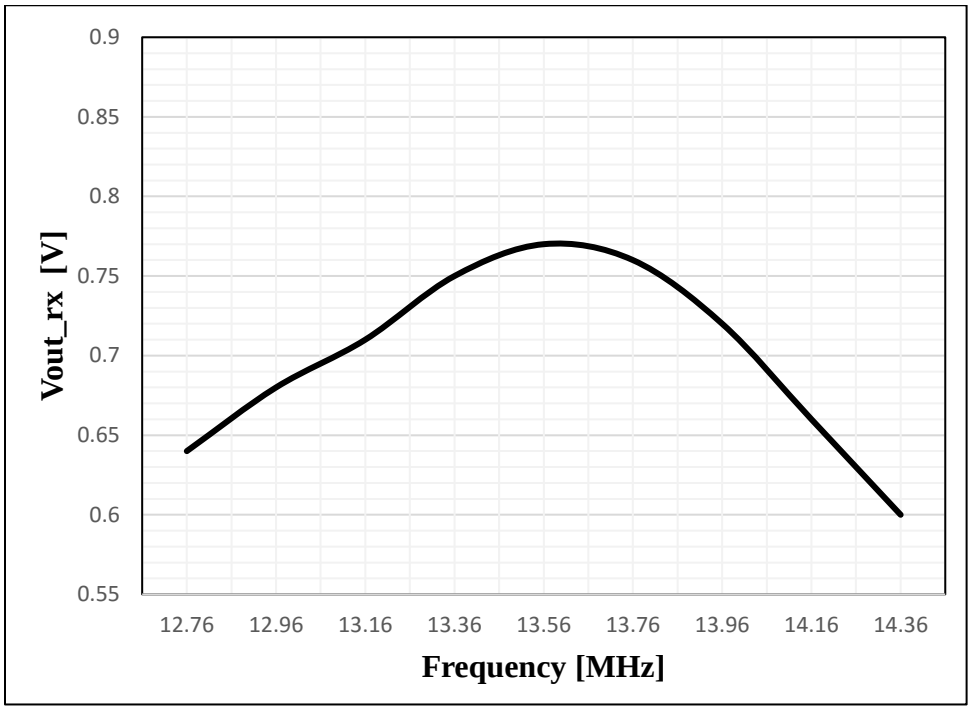

Figure 4-15: Received voltage at the resonant frequency of 13.56 MHz

4.4.2 V_{bias} vs. F_{res} Measurements

In simulations, the range of the resonant frequency can be widened by adjusting the bias voltage of the varactor and by the addition of the weighted capacitors, as shown in Figure 4.16. This concept is proven in the lab setup, as data shows in Figure 4.17.

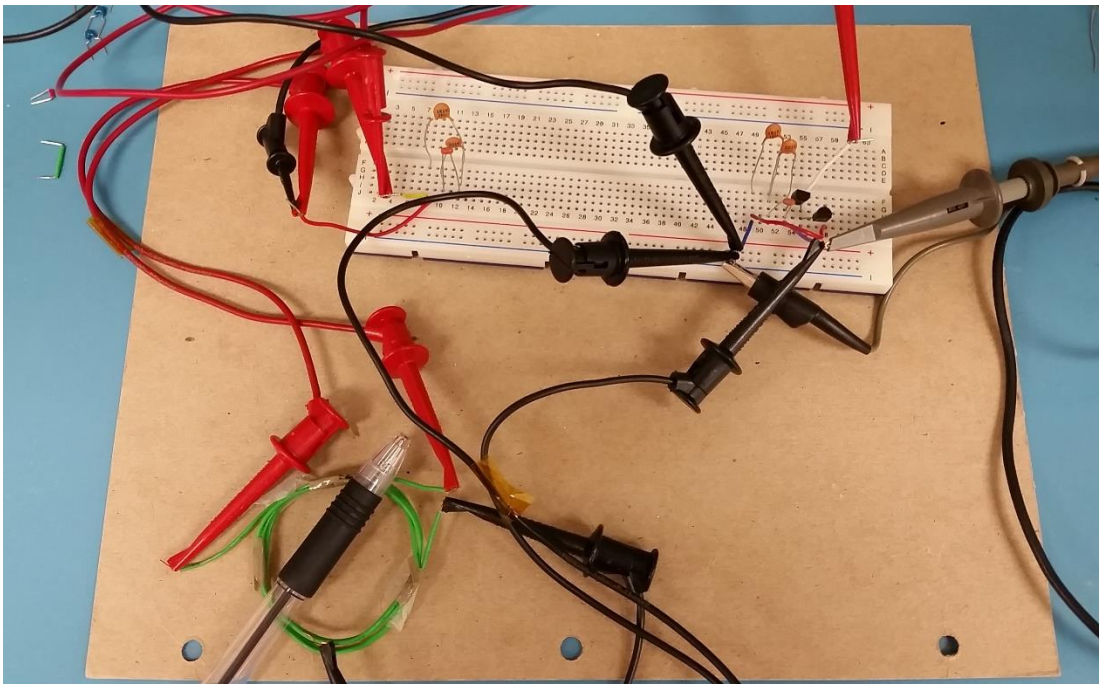

Figure 4-16: Binary capacitors and varactor are added to the WPT system

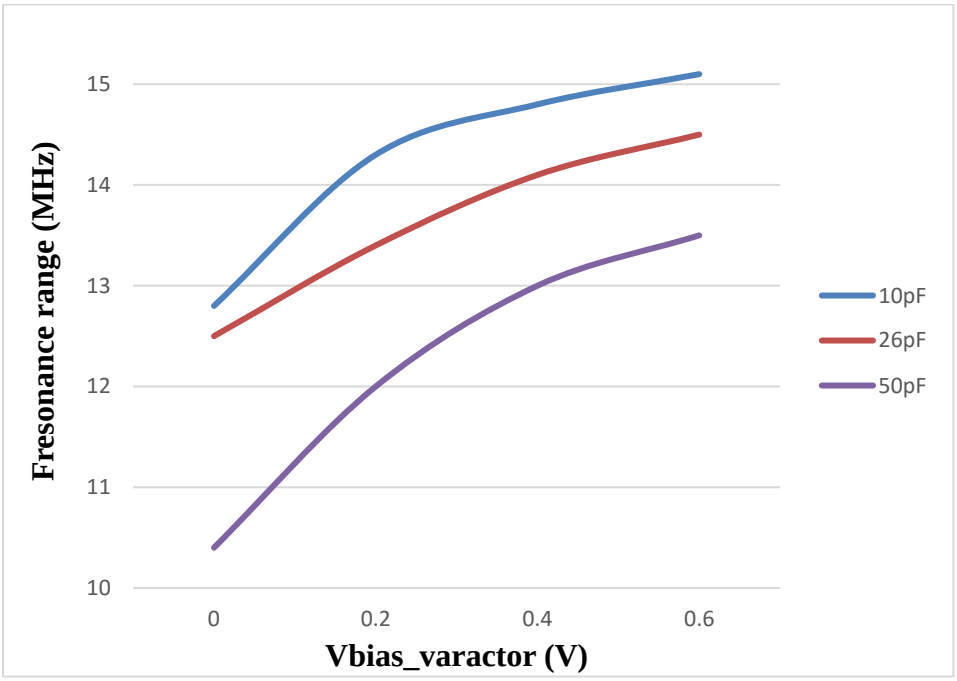

Figure 4-17: The resonance frequency range vs bias voltage of the variable capacitor

4.4.3 Detuning by Component Mismatch

To emulate one of the possible causes of detuning—component mismatch—C_{tx} is changed from 115 pF around 130 pF, while C_{rx} kept fixed at 115 pF. Figure 4.18 shows this case of detuning very clearly where the resonance frequency is shifted from 13.56 MHz to 12.5 MHz.

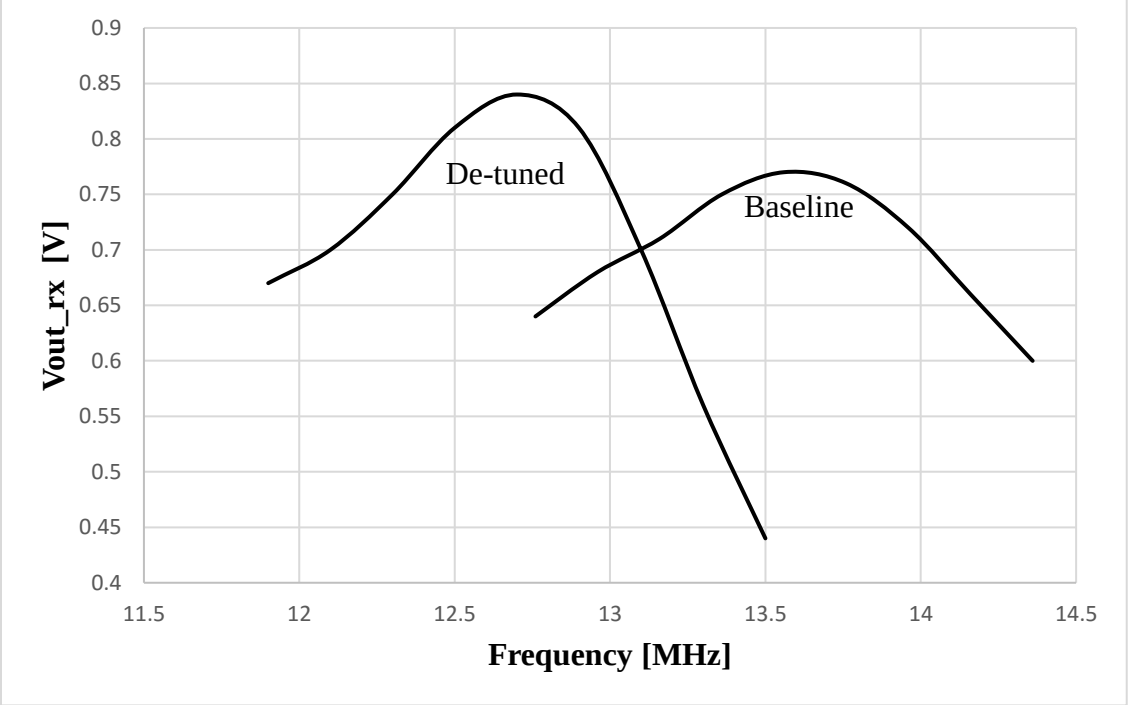

Figure 4-18: Detuning of baseline by component mismatch

By adding both MOScap and binary switches, the system was back at the baseline resonant frequency of 13.56 MHz, as shown in Figure 4.19. In this setup, the main cap is around 90 pF, the binary cap is 22 pF, and the varactor cap (22 pF) is biased at 0.2 V.

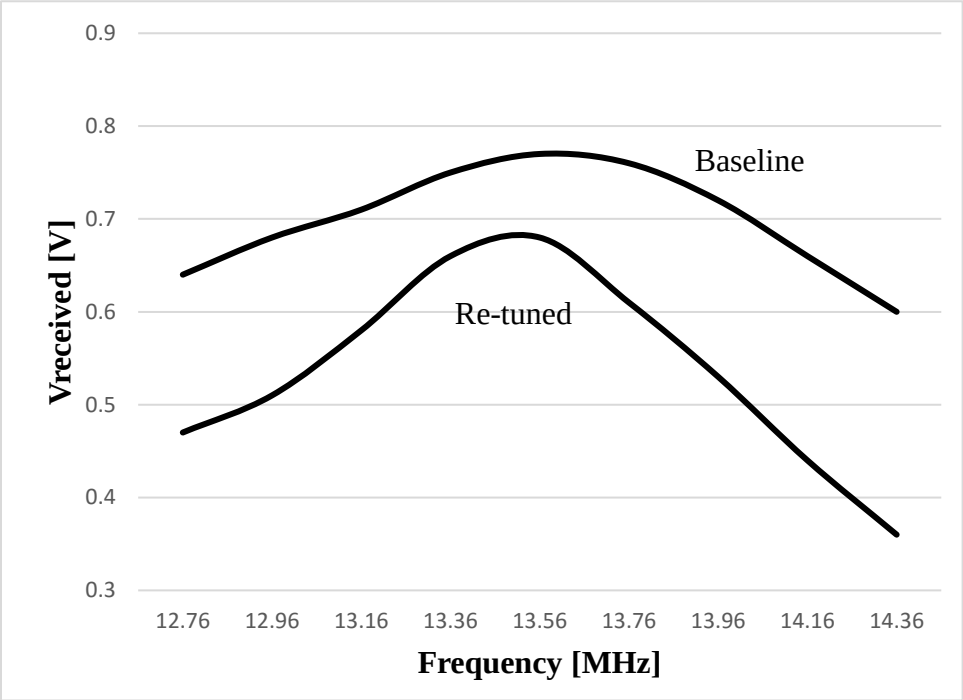

Figure 4-19: Baseline and Retuned results

4.4.4 Detuning by Misalignment

One of the weakest features of a loosely coupled system is inefficient power transfer due to misalignment of transmitter and receiver coils. This scenario is created in the lab, as shown in Figure 4.20.

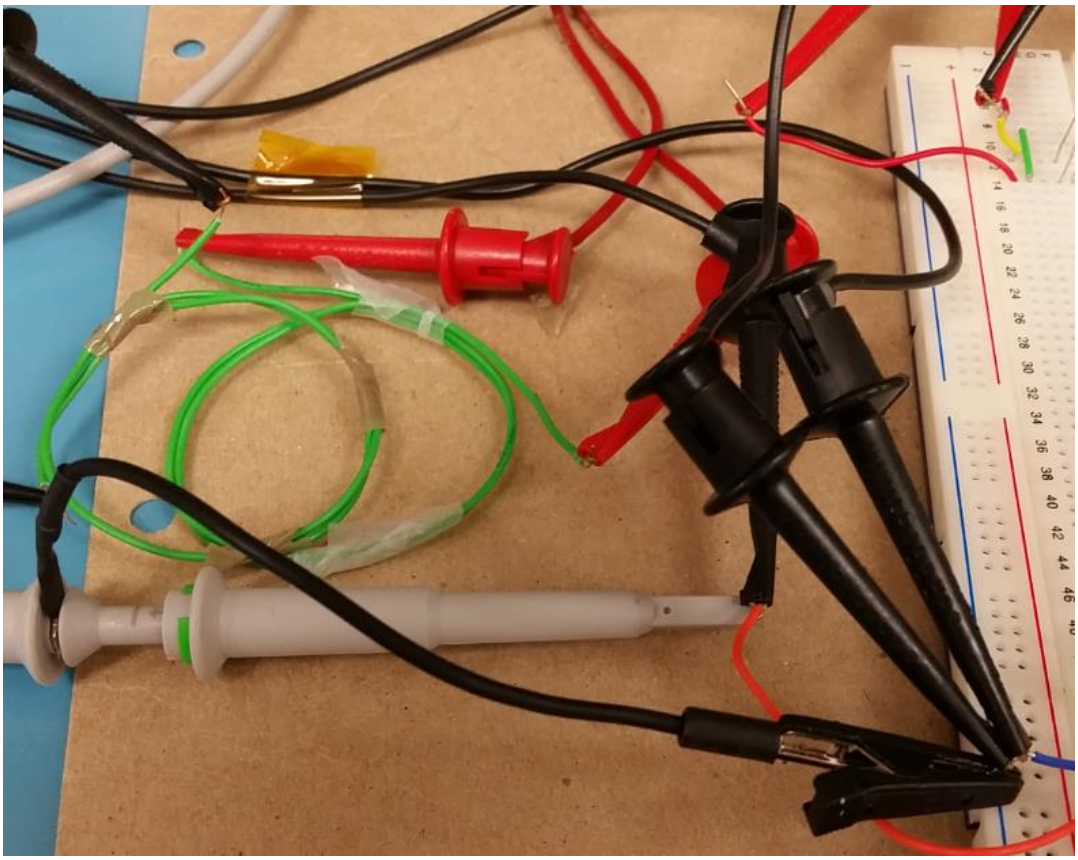

Figure 4-20: Misalignment of transmitter and receiver coils

Misalignment caused the system resonance to shift to 14.6 MHz. By modifying the bias voltage of MOSCap and adding binary switch capacitors to the system, the baseline resonant frequency was obtained at 13.56 MHz in the re-tuned system, as shown in Figure 4.21. Component values are shown in Table 4.4.

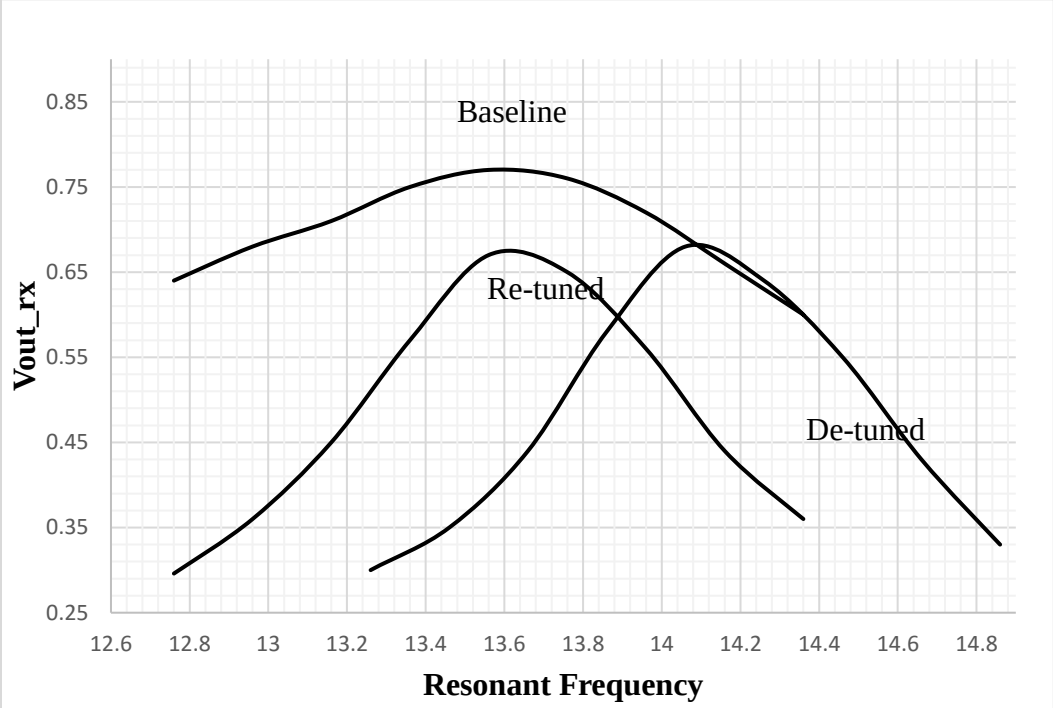

Figure 4-21: Comparison of baseline, de-tuned, and re-tuned systems

Table 4-3: Component values of baseline, de-tuned, and proposed hybrid systems

System	Crx	Cvar/Vbias	Cswitch	Ltx, Lrx
Baseline	115 pF	--/--	--	1.2 µH
De-tuned	115 pF	--/--	--	1.2 µH
Proposed Hybrid Structure	90 pF	22 pF/0.1 V	22 pF	1.2 µH

4.4.5 Effect of Distance

The final experiment is performed when the transmitter and receiver coils are both misaligned and separated from each other, as shown in Figure 4.22. The distance, *d*, between the coils is about 3cm.

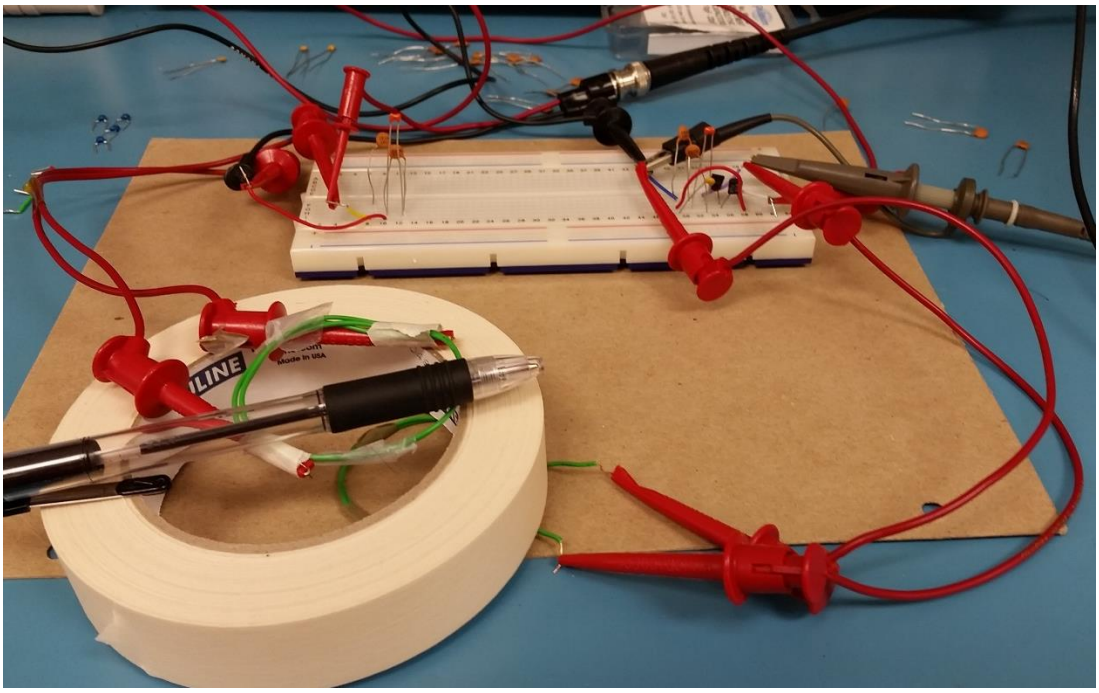

Figure 4-22: Misaligned and separated coils

A closer look at the breadboard setup is shown in Figure 4.23. Finally, tuning is successfully performed and the results are plotted in Figure 4.24.

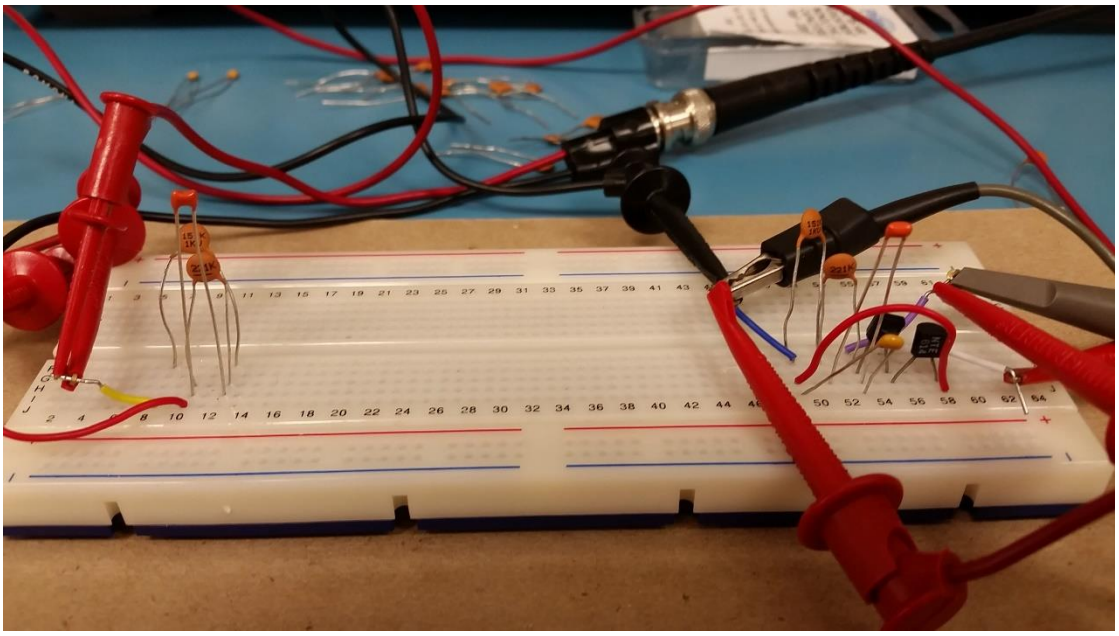

Figure 4-23: Full set of transmitter and receiver capacitors

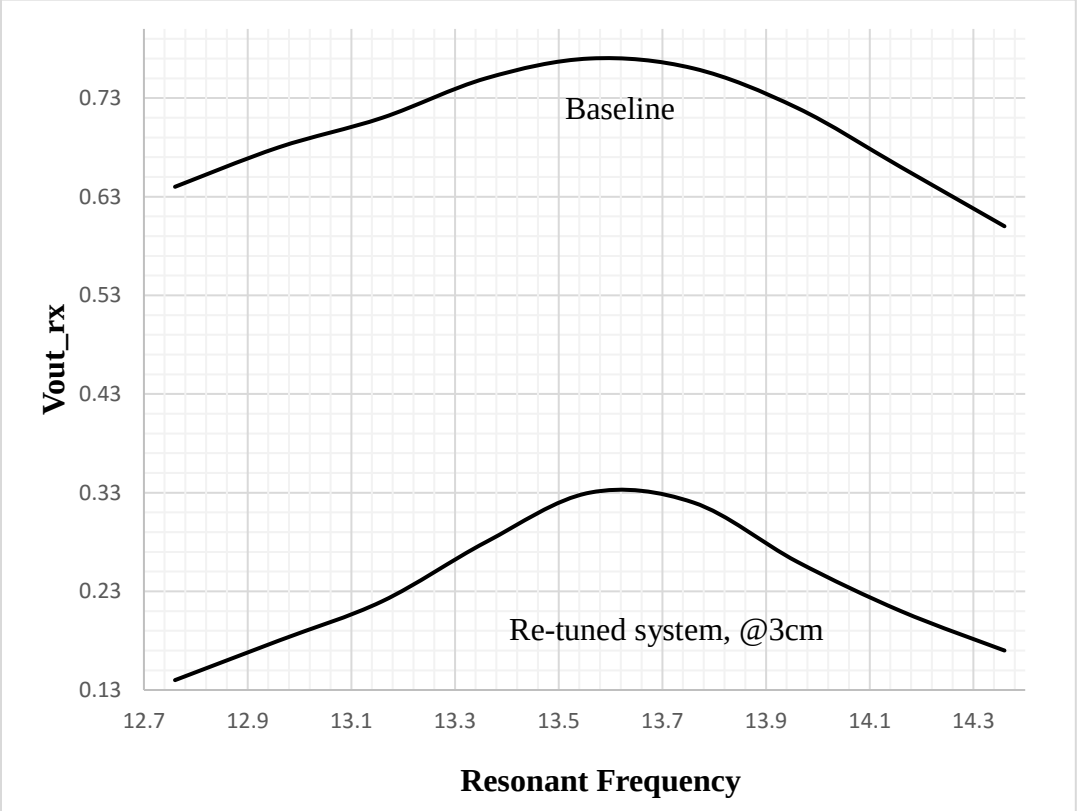

Figure 4-24: Baseline results and retuned system results

Full Test setup with live experiment results are presented in Figure 4.25.

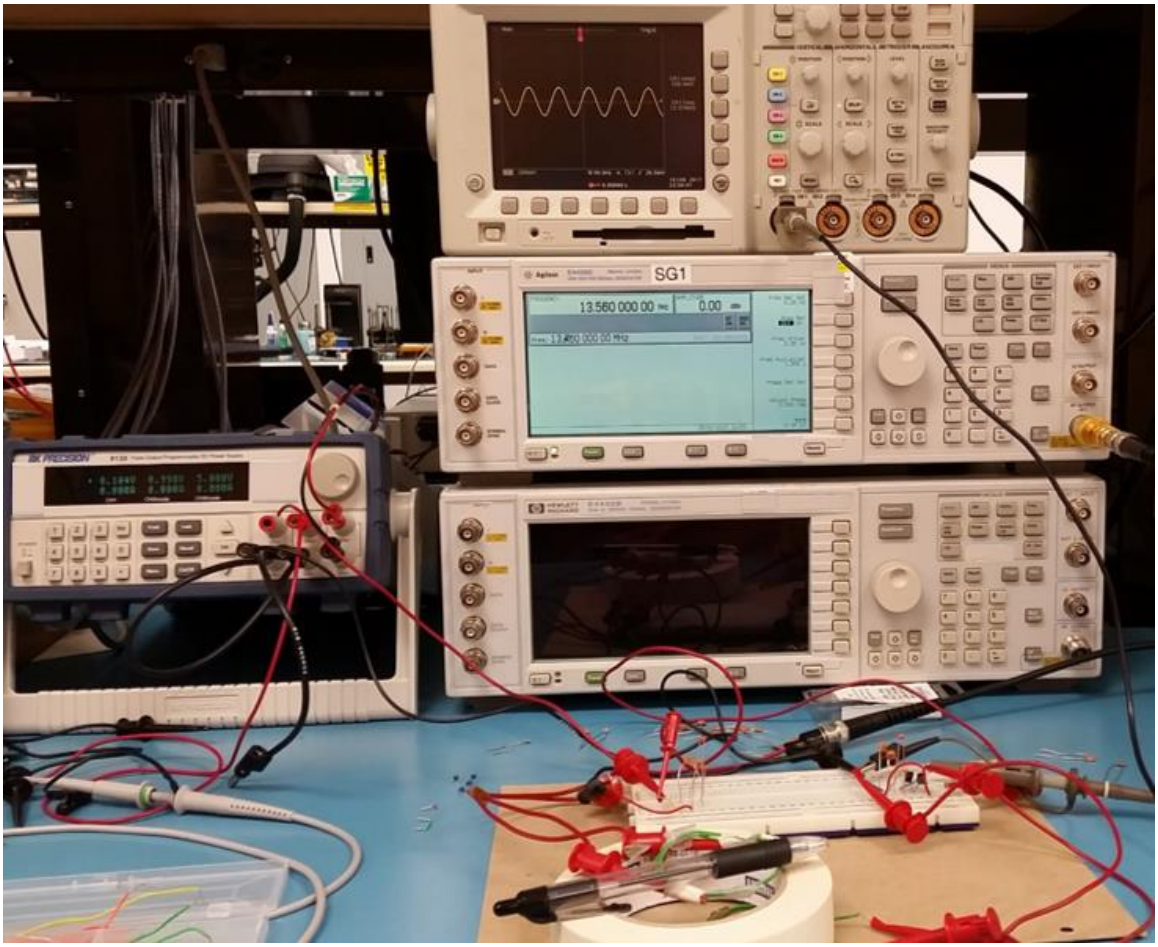

Figure 4-25: Full test setup with Bias source, oscilloscope, signal generator and tuned WPT system

4.4.6 Discussion

During the experiments, WPT is tested using two different setups. In the initial test setups, proof-of-concept is demonstrated at 1 MHz by using all discrete components even for the transmitter signal generation. The measurements are taken using low-frequency USB based oscilloscope. During this test, NEC brand power MOSFET is used as variable capacitor for tuning purposes.

Later on, this setup is carried to the high frequency range around 13.56 MHz. Signal generation is performed by using RF signal generator and measured with powerful high frequency oscilloscope. WPT antenna coils are changed to much lower range of 1.2 μH to achieve resonance at 13.56 MHz. Capacitors are in the lower tens of pFarad ranges, including main, weighted, and variable capacitors.

As seen from the test results, each of the system structures including, baseline, detuned (by component mismatch and by misalignment), and retuned are created successfully. The final component values are very close to the simulations values with resonant frequency of 13.56 MHz. As additional data point, it is shown that when the distance between transmitter and receiver coils are increased, the magnetic field strength is decreased. As shown in this part of the dissertation, WPT system can be effectively tuned by using proposed hybrid capacitor structures with great tuning-range.

5 Double–Pulse Charge Technique for Wireless and Mobile Devices

5.1 Introduction

A battery is the crucial energy source for most electronic products. With the rapid growth of various electronic devices, frequent charging of batteries has become very important. Faster charging time while ensuring the longevity of the battery is important and critical in applications such as medical implants because of the uncomfortable positioning of patients and the heating of the exposed area. The expected longevity of the battery is 10 to 15 years to avoid any unnecessary invasive operations.

5.2 General Background on Batteries

5.2.1 Cell:

A cell is a device that converts chemical energy to electrical energy for the purpose of generating or storing electrical energy. This conversion to electrical energy is done by chemical reaction, which involves movement of electrons from one material to another material via an electric circuit.

5.2.2 Battery:

A battery is collection of cells connected in series, parallel or in combination or both to provide desired voltage and capacity. Batteries are usually categorized as primary and secondary. Primary batteries are called single-use, throw-away or disposable batteries, as they are used only one time until they run empty. These batteries cannot be recharged, as the chemical reactions are not reversible and as the active materials may not return to their

original states. Carbon zinc, alkaline, lithium, silver oxide and zinc are some of the primary battery types.

Secondary batteries consist of galvanic cells that must be charged before they can be used. In these cells, the spontaneous reaction that generates current (provided by devices called chargers) is reversed so that chemical energy can be stored. Due to the nature of these cells, secondary batteries can be recharged. These batteries are generally specific to applications and require a specific charger. Additionally, they are heavier, more expensive, and have sophisticated electronics for the control and management of the power compared to their primary counterparts. The latest development in lithium batteries has made it possible to have smaller, lighter secondary batteries for portable electronics such as smart phones and digital cameras. Rechargeable alkaline, nickel-cadmium, nickel-metal hydride, lithium ion, lead-acid, and lithium polymer (li-poly) are types of secondary batteries.

5.3 Battery Charging Techniques

Charging is the process of returning energy back to the battery where the process is compatible with the working mechanisms of chemistry for a specific battery. Therefore, recharging is important, as it involves the safety of equipment, personnel, and the environment. There are different ways [21] [22] [23] [24] to charge a battery that involve different control signals such as current or voltage.

5.3.1 Constant Current (CC) Charging

This technique is the simplest form of battery charging. Constant current is applied to the discharged battery while the voltage of the battery is increased as shown in Figure 5.1. The charger needed for this technique is relatively small and inexpensive. Sometimes, gassing and overheating may occur when the battery is overcharged. The measurements and limits

of voltage or temperature can be utilized as a means of termination. This charging method is suitable for nickel-cadmium and nickel-metal batteries.

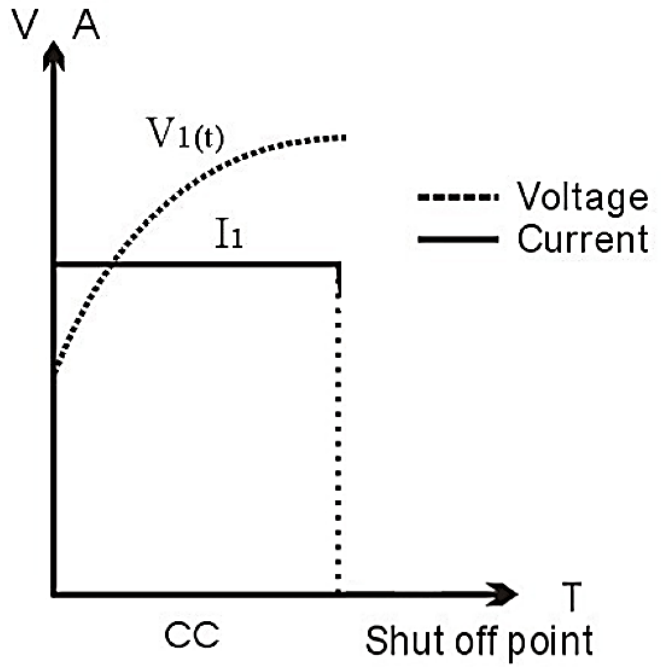

Figure 5-1: Constant current (CC) charging

5.3.2 Constant Voltage (CV) Charging

A basic DC power supply provides constant voltage charging. When the battery is discharged, its terminal voltage and equivalent internal resistance might be low, thereby causing a very large inrush current to flow, as shown in Figure 5.2. As a battery charges up, its internal resistance decreases and its terminal voltage consequently increases. Once the voltage limit is reached, the current starts to taper down. Eventually, when the battery is fully charged, it may start to take trickle current to compensate for the self-discharge of the battery. In this method, the current limitation comes either from the battery itself or from the current limiter in the charger. Primarily, lead acid and nickel-cadmium pocket

plate batteries (not sealed batteries) use this method of charging. Lithium-ion batteries are also suitable for this technique even though they require extra circuitry for the protection of the device and the user.

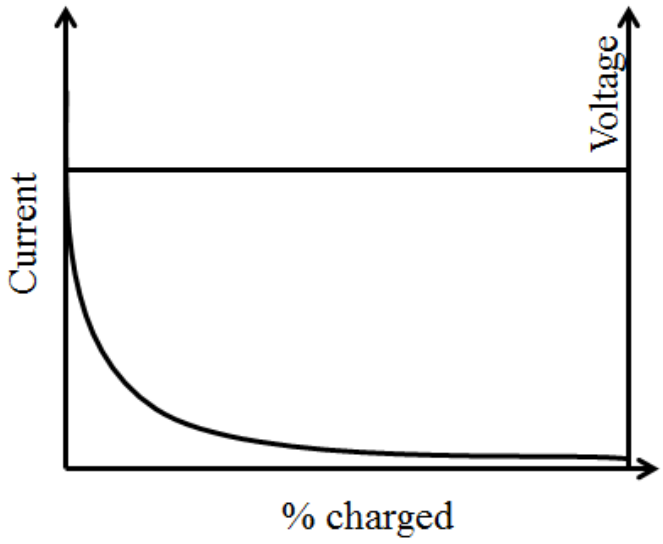

Figure 5-2: Constant voltage (CV) charging

5.3.3 Constant Current Constant Voltage (CC-CV) Charging

In this technique, constant current is applied until the battery voltage reaches a preset value. This phase is usually called bulk charging. During the next phase, the charging scheme is switched to constant voltage charging until the current reaches another preset value, as shown in Figure 5.3. Sealed lead-acid and pocket-type nickel-cadmium batteries are suitable for this technique.

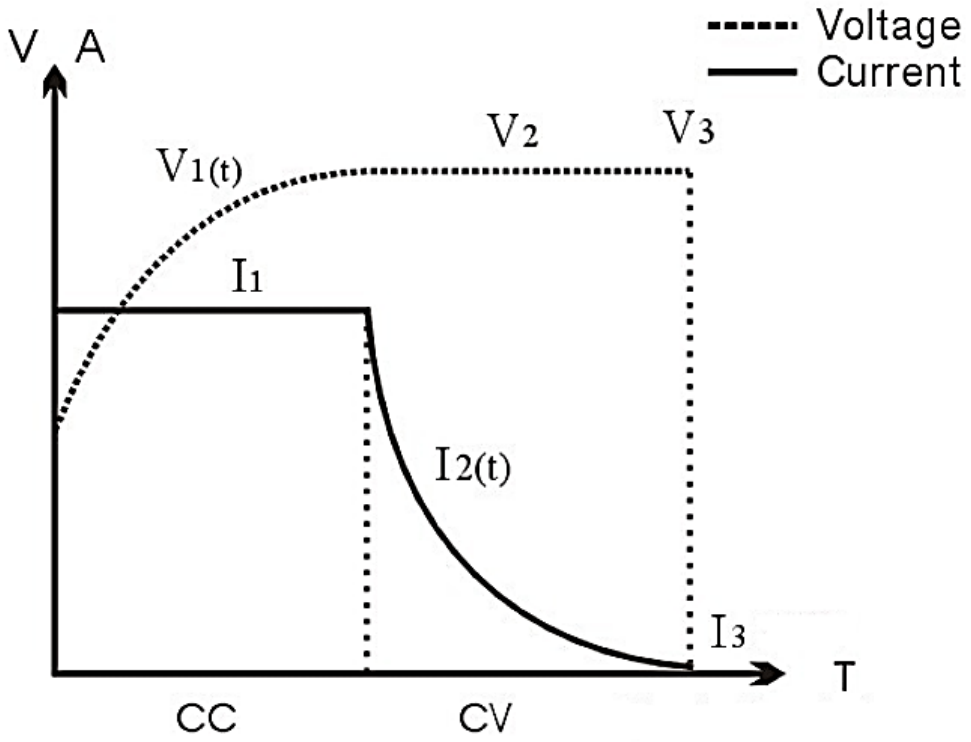

Figure 5-3: Constant current constant voltage (CC-CV) charging

5.3.4 Multi-Charging

In the multi-charging technique, a charging algorithm starts to apply the largest predefined current to the battery [25]. When the battery voltage reaches the first threshold level, current is reduced by half until the next threshold level is reached. This continues until the battery is fully charged. This concept is shown in Figure 5.4.

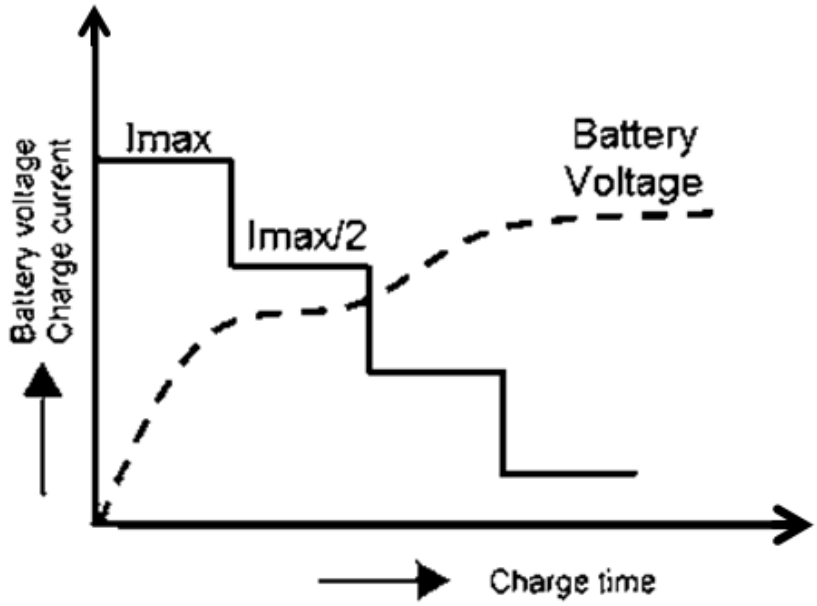

Figure 5-4: Multi-Charging (Multi-C)

5.3.5 Pulse Charging

Another technique is to apply either current or voltage pulses to the battery [26] [27]. The charging rate (based on the average current/voltage) can be precisely controlled by varying the pulse-width, rise time, frequency and amplitude of current or voltage pulses. Furthermore, there are short "rest" periods between pulses to allow the chemical reactions to stabilize in the battery. This enables the chemical reactions to keep pace with the rate of electrical energy inside the battery. Obviously, this type of control and management of the system requires complex circuitry and some sort of microprocessor.

5.3.6 Burp Charging

Lastly, burp charging is also called reflex or negative pulse charging (discharging). It can be considered the modified version of pulse charging. In this technique, the fraction of resting is replaced by negative pulses. As expected, these negative pulses depolarize the cells, releasing any gas accumulation that might have built up on the electrodes. Studies

show resting periods or negative pulses have a positive impact on the longevity of the battery. Pulse charging with negative pulses (burp charging) is illustrated in Figure 5.5.

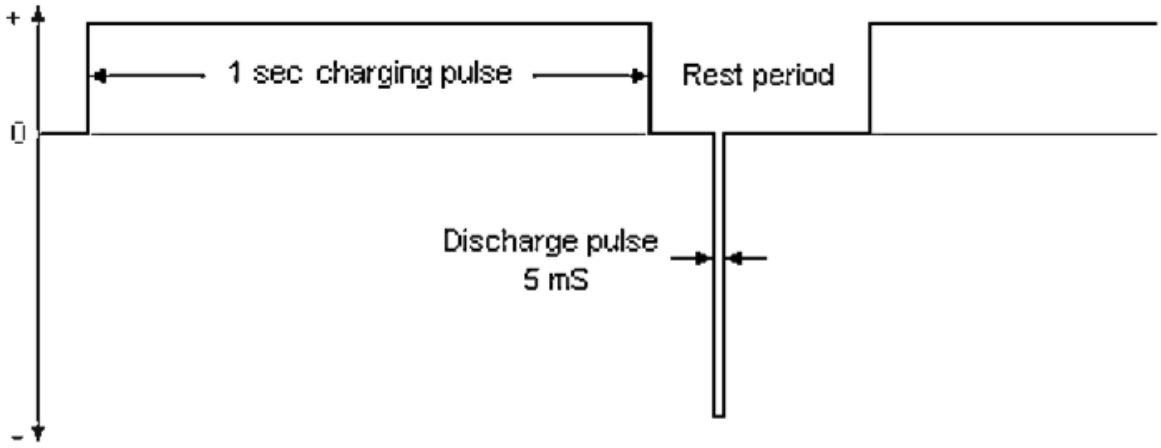

Figure 5-5: Pulse and burp charging

5.4 Proposed Battery Charging Technique

In summary, all of the methods mentioned in previous sections are targeted mainly to decrease charging time without affecting the stability of the process by providing a safe temperature and the best power efficiency for the battery. In this study, pulse charging is further explored. In pulse charging, both of the phases (charging and resting) are actively used for battery charging with various amounts of current. The method is called a double-pulse-charging system.

5.4.1 Pulse Charging Block

As a baseline, pulse charging is modeled with a current source, an inductor, two switches that use double-phase clock, and a load that may be a battery or super capacitor to be charged, as shown in Figure 5.6. The model of the battery is shown in the dashed box [28] [29] [30] [31]. The system is implemented and simulated in Cadence Virtuoso by using circuit elements from the built-in analog library. A load capacitance value of 30F is chosen. The possible leakage path is modeled by a large resistor of 1MOhm. Transient behavior during charging is modeled by a variable current of I_{load}, with amplitudes changing from 1mA to 10mA.

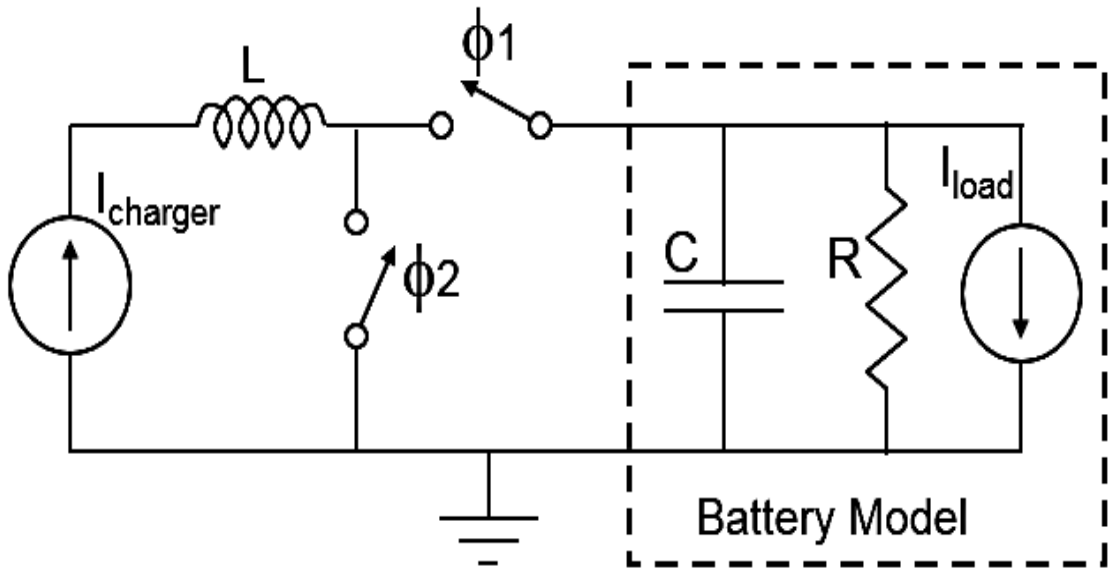

Figure 5-6: Simple model of pulse charging system

Equations 5.1 and 5.2 describe the charge preservation and stored energy in batteries, respectively.

$$Q = CV \tag{5.1}$$

$$E = \frac{1}{2} CV^2 \tag{5.2}$$

Q: Amount of charge built up in the capacitor

V: Voltage across capacitor

E: Energy supplied by the capacitor

The battery model depicted in Figure 5.6 is simulated to be charged to the final voltage of 4V in about 7k seconds, corresponding to approximately 2 hours, as shown in Figure 5.7.

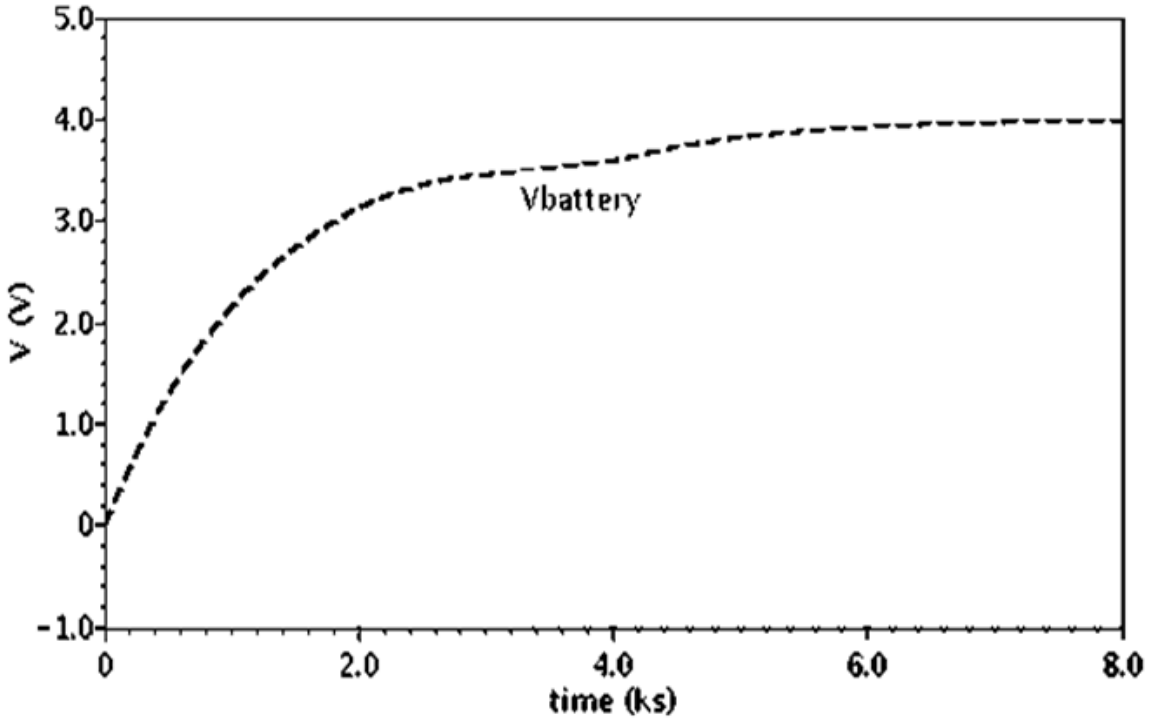

Figure 5-7: Battery charging time of pulse charging system

The amount of charge can be also expressed in terms of current flowing to the load and the time, as shown in equation 5.3. *D* is the duty cycle of the clock where current is flowing to the battery.

$$I = \frac{Q}{T.D} \tag{5.3}$$

Moreover, substituting (5.1) into (5.3) and solving for *T* will provide an estimated battery charge time as shown in (5.4):

$$T = \frac{C.V}{I.D} \tag{5.4}$$

Specifically, the two non-overlapping clock waveforms, Φ_1 and Φ_2, with a period of *T* are shown in Figure 5.8. In this example, the clocks have periods of 20ms and duty cycles of 50%. During phase Φ_1, the battery is charged to the maximum amount of current available, and during phase Φ_2, the battery is left to rest. Additionally, the pulse-widths can be varied based on a particular battery charging system.

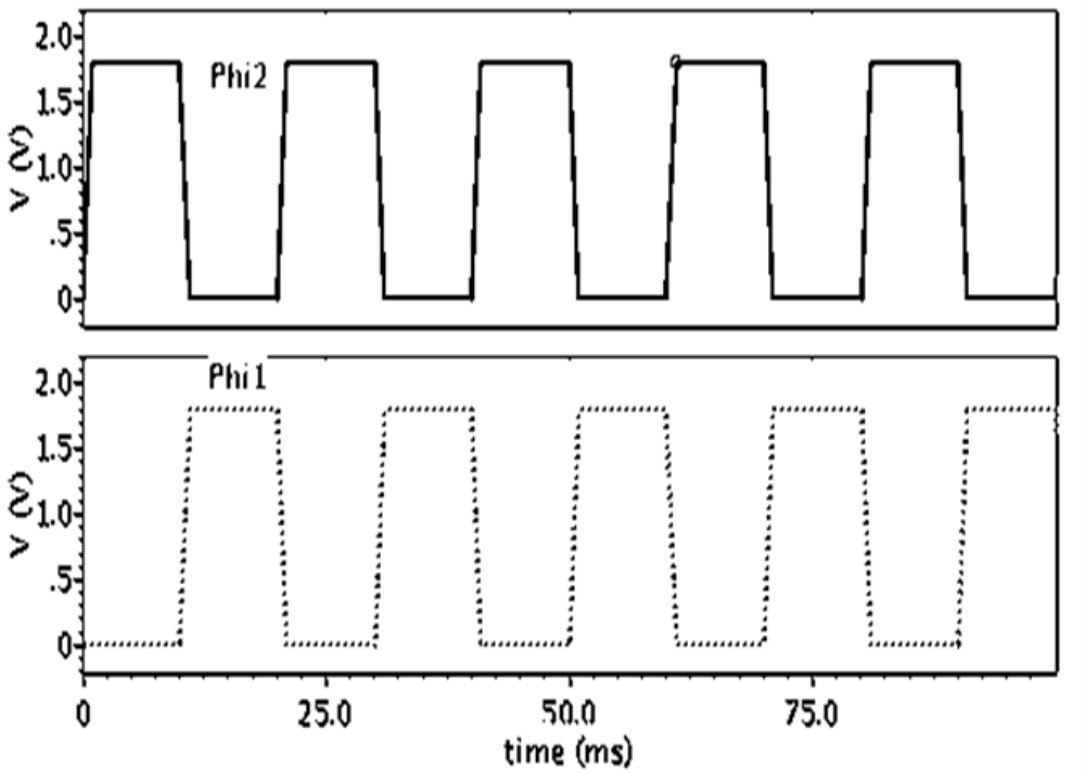

Figure 5-8: Two non-overlapping clock waveforms

5.5 Double Pulse Charging Block

A simple model of a double pulse-charging system (DPCS) is shown in Figure 5.9. The main idea in this system is to keep charging the battery with a small amount of current during the second phase, $\Phi_{2,}$ instead of leaving it idle. Correspondingly, equation (5.4) can be modified to reflect this double charging operation, as stated in equation 5.5. I_{max} is the maximum amount of current allowed by the safety limits, and I_{min} is the minimum amount of current that can still charge the battery while having very small effect on the longevity of the battery. D is the duty cycle of (DTC) of I_{max} pulse.

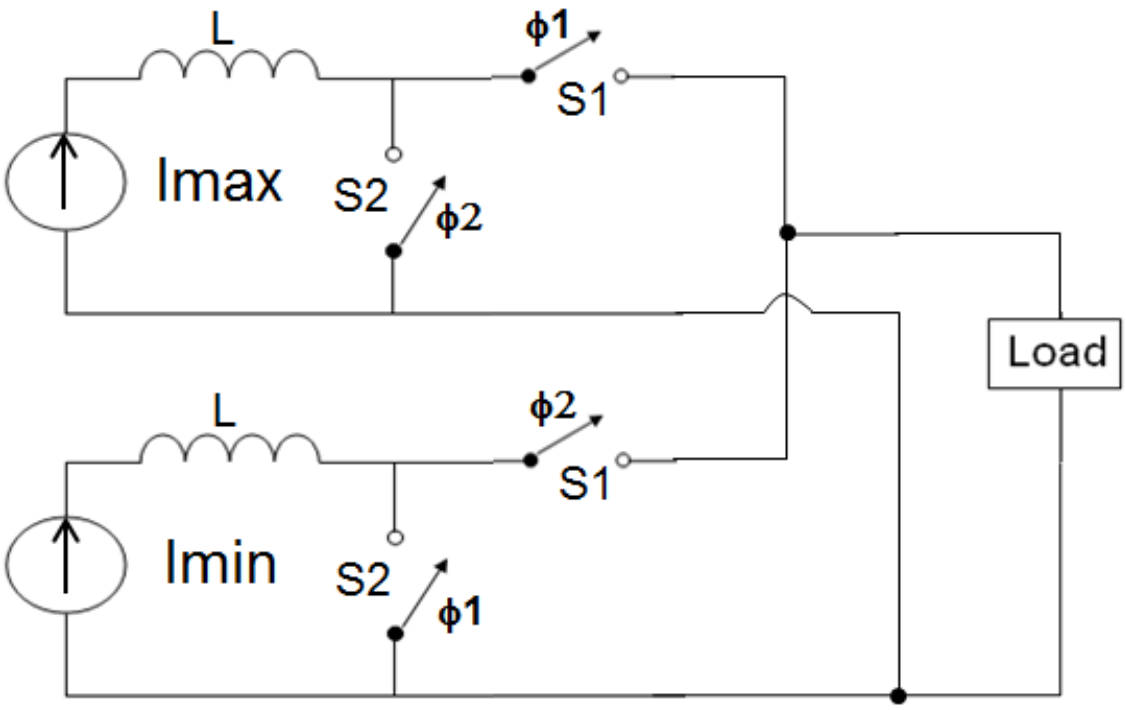

Figure 5-9: Model of double-pulse charging system

$$T = \frac{(V.C)}{[I_{max.}.D + I_{min}(1-D)]} \tag{5.5}$$

In our study, I_{max} is selected as 400mA and applied to the load during the first clock phase (Φ_1), and I_{min} is selected as 20 mA and applied during the second clock phase (Φ_2). Also, a duty cycle of 50% is selected in the simulations. Based on the circuit components, comparison of simulated battery-charging waveforms for PCS and DPCS are shown in Figure 5.10. As shown, the proposed double-pulse charging system has the advantage of faster charging time. It takes about 1.7 hours compared to 2 hours of PCS.

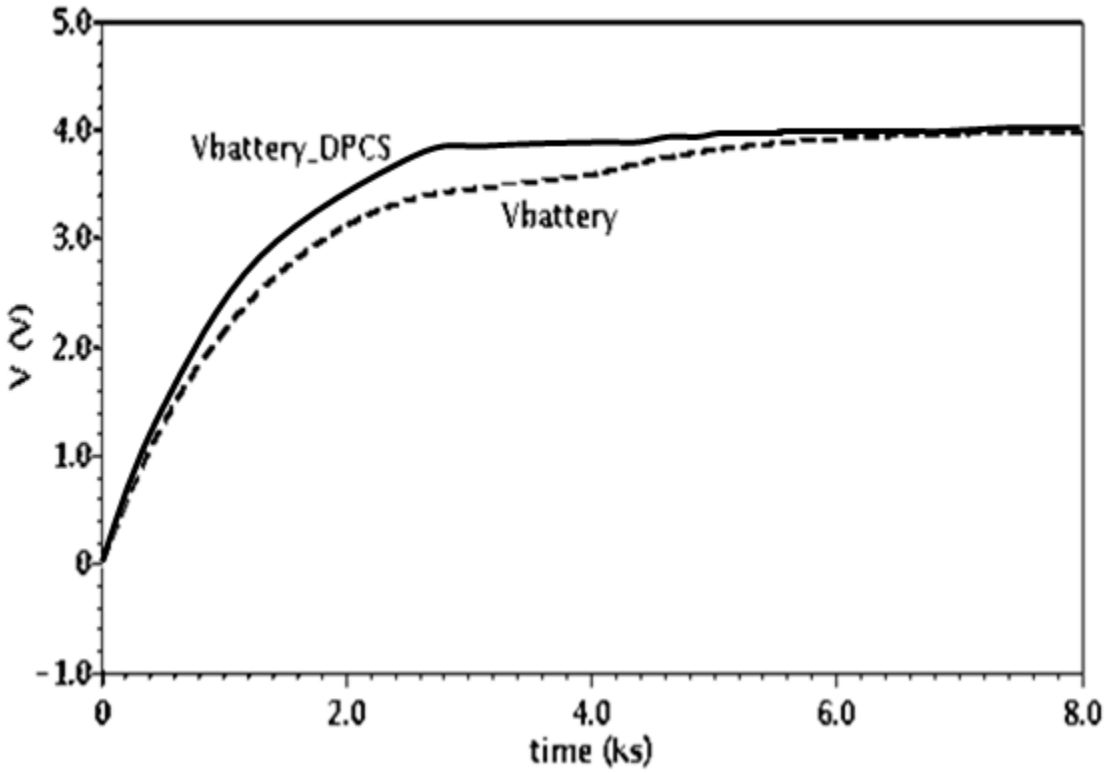

Figure 5-10 Charging time: PCS (dashed) vs. DPCS (solid)

5.6 Programmability of Double-Pulse Charging

For a given battery voltage and battery capacitance, it is possible to optimize the performance of the DPCS by modifying the amplitude of I_{max}, the amplitude of I_{min}, the pulse duration of I_{max} (pulse width as $\alpha.D$), the pulse duration of I_{min} (pulse width as $\eta.D$) and the period factor of I_{min} (β), as shown in updated equation 5.6. These options are discussed in the next subsections.

$$T = \frac{V}{\{I_{max(t)}.\alpha D + I_{min(t)}[\beta(1-(\eta D)]\}} \qquad (5.6)$$

The DTC of I_{max} and I_{min} can be controlled independently; hence, they have two different factors, α and η. In the case of both currents having more than 50% of duty cycle, there will be overlapping sections in which the battery is charged by both currents at the same time.

5.6.1 Amplitude of I_{min}

During the second phase, Φ_2, the amplitude of the minimum charging current can be varied to reach different levels of battery voltage faster. In Figure 5.11, three different output voltages—3.6V, 3.8V, and 4V—are shown at 2.8ks (~47minutes) when I_{min} is varied from 5mA to 15mA in 5mA steps. Hence, the design of DPCS can be optimized or can be integrated with multi-charge systems so that the multi-step current can be utilized.

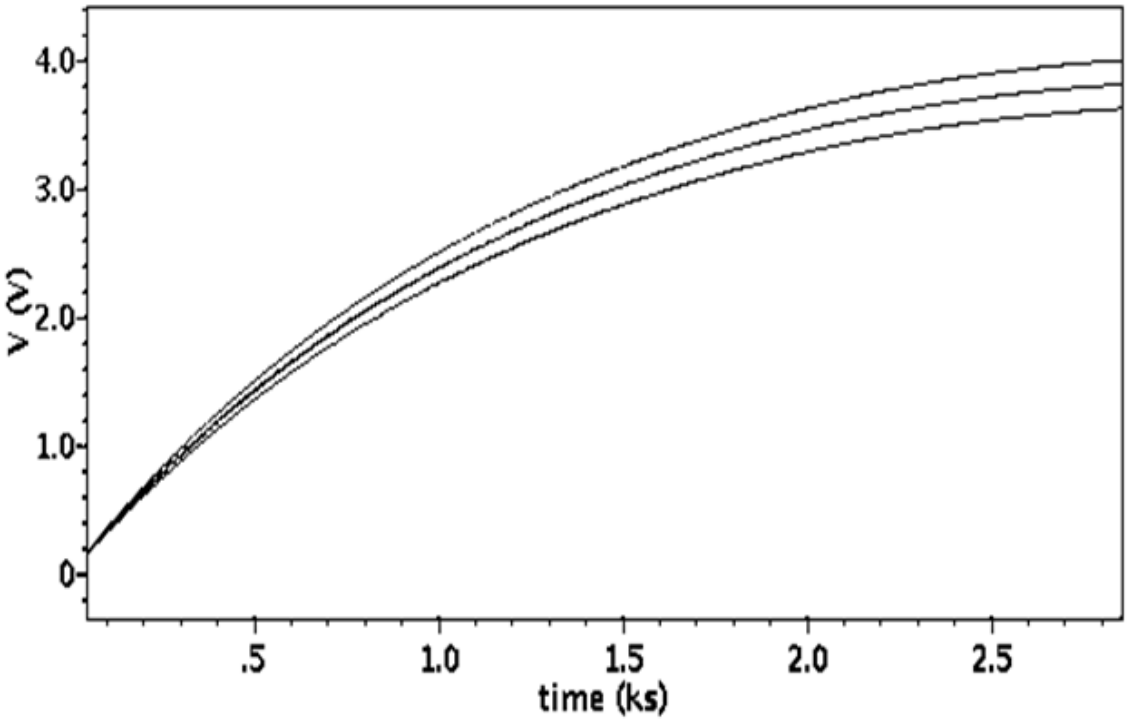

Figure 5-11: Settled battery voltages of DCPS at t=2.8ks; I_{max}=400mA, I_{min} is 5,10, and15mA.

5.6.2 Time Period of I_{min}

In addition to varying the amplitude of I_{min}; the period of the clock for I_{min} can be varied. During the first phase, Φ_1, while the maximum current always charges the battery with a clock period of 20ms, the minimum current may be able to charge the battery with a different clock period. The simulation result with two different periods of I_{min} pulse is presented in Figure 5.12. Basically, fewer I_{min} pulses will be applied to the battery when the time period is increased. This type of control will use some of the idle durations (when I_{min} is not applied) to improve battery reliability if needed without drastically sacrificing the battery charging time.

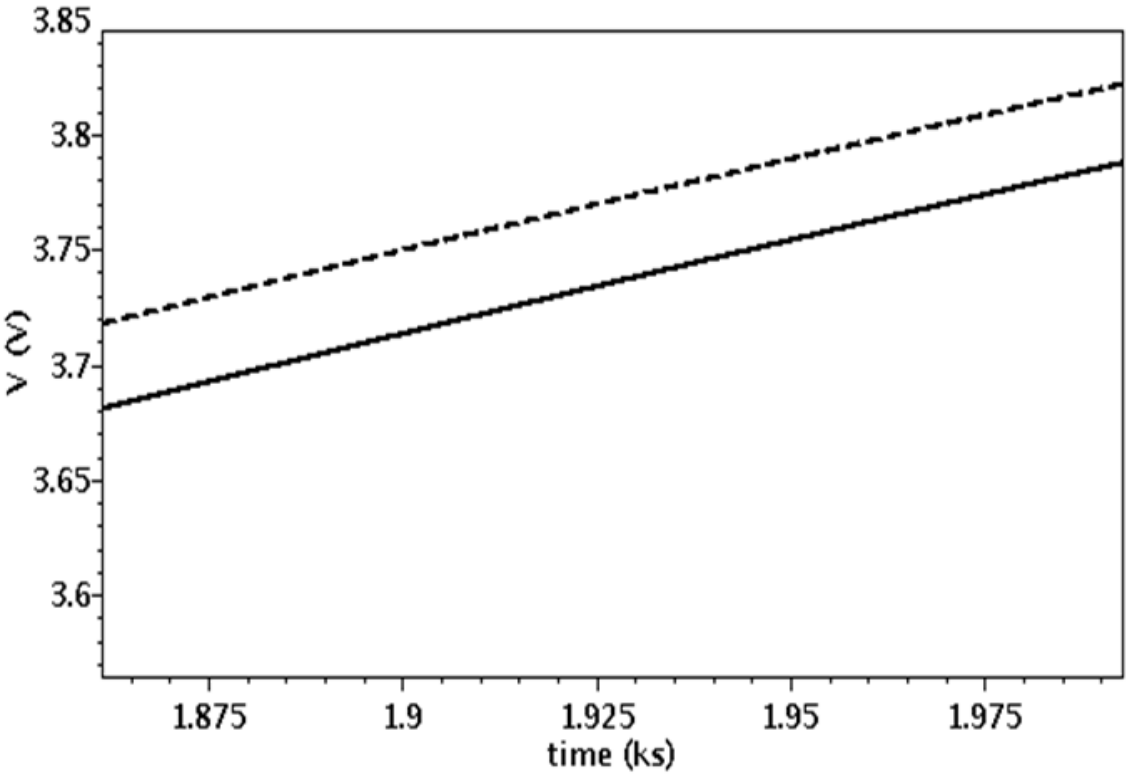

Figure 5-12 : Time period of I_{min} is varied from 20ms to 160ms

The clock period of I_{min} can be changed by using a frequency divider, as shown in Figure 5.13.

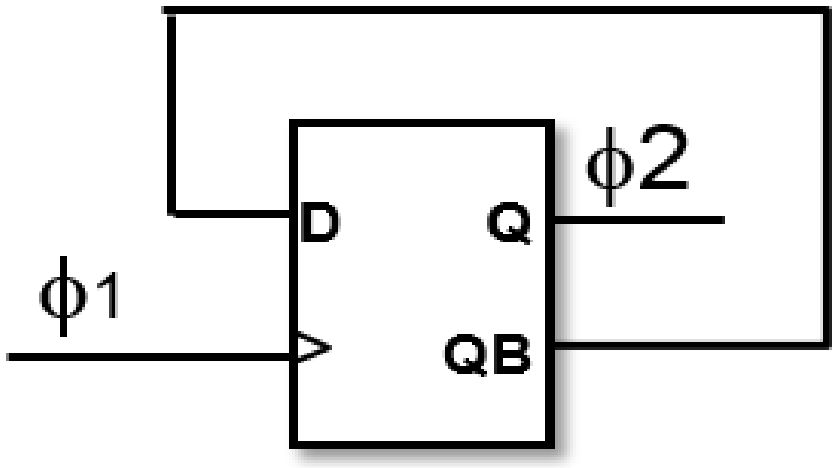

Figure 5-13: Frequency divider for I_{min} pulses

5.6.3 Duty Cycle of I_{min}

As mentioned earlier, DTC or pulse width of I_{min} also can be optimized further. The pulse width of a CMOS clock signal can be easily controlled by simple digital circuits. One example of DTC control circuit is shown in Figure 5.14. The effects of duty cycle variation on the battery voltage can be seen in Figure 5.15.

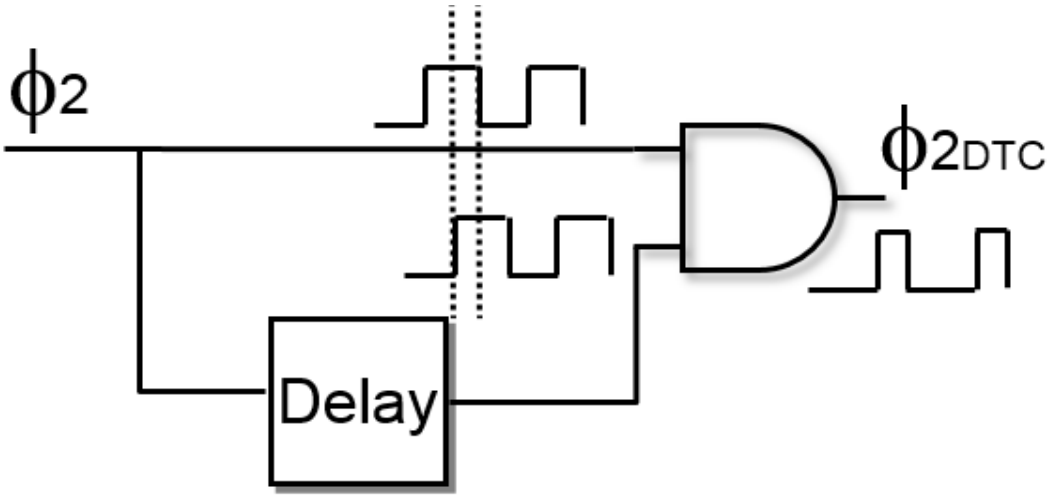

Figure 5-14: Duty cycle control circuit

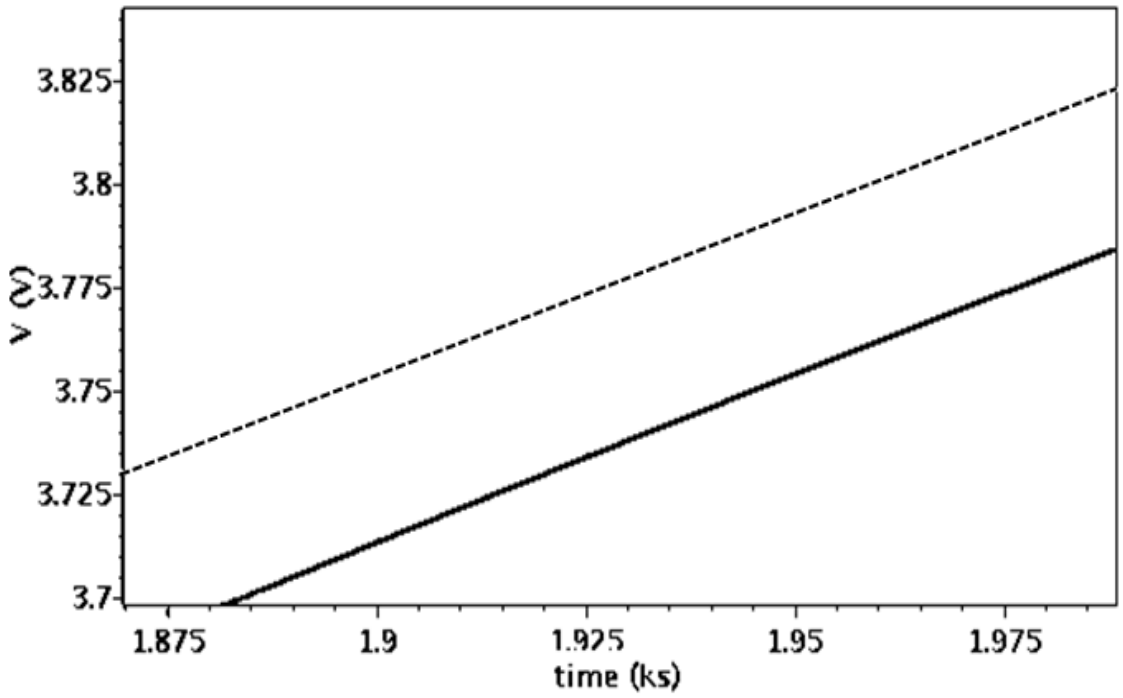

Figure 5-15: Controlling duty cycle of I_{min}; 5% (solid), 45% (dashed)

5.6.4 Amplitude and Duty Cycle of I_{max}

Obviously, amplitude and duty cycle variations of I_{max} will have larger impacts on the final battery voltage than I_{min}. Simulation results with different amplitudes of I_{max} are shown in Figure 5.16. This method can be considered a combination of Multi-C and DPCS.

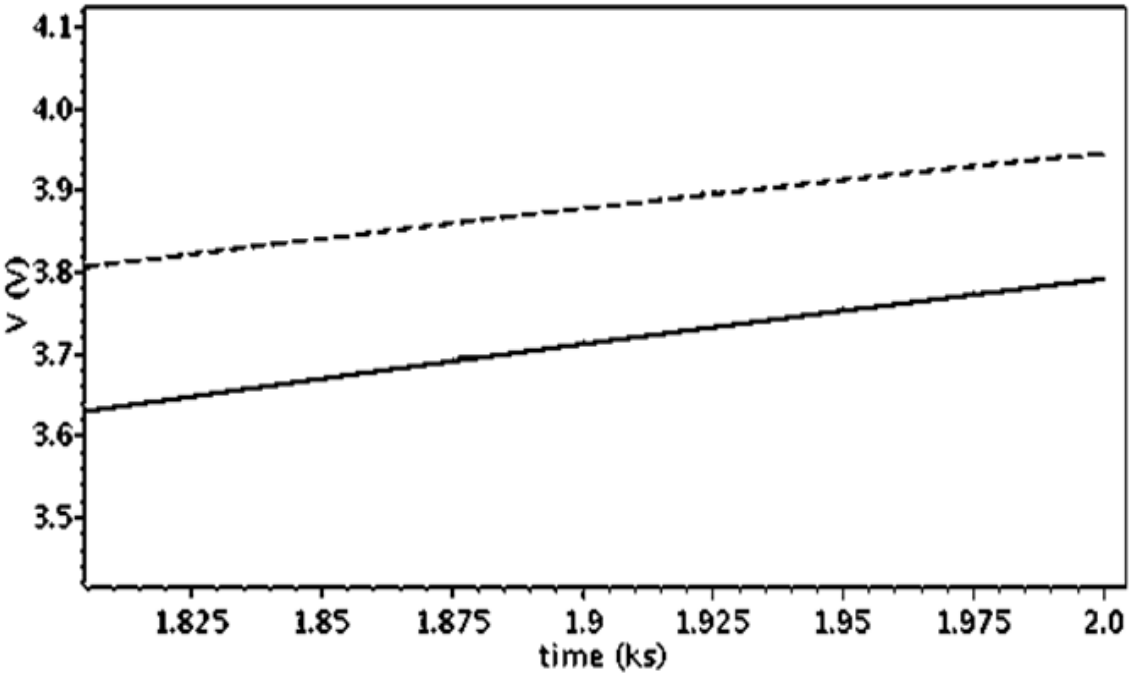

Figure 5-16: Amplitude variations of I_{max} ; 400mA and 600mA

5.7 Application of the DCSP to a Wireless Power-transfer system

As the final step of the study, an inductively coupled, wireless power-transfer system is considered for the adaption of the DPCS system to be used in battery charging. As explained in Chapter I, in a WPT system, the strength of the magnetic field between the coils of the transmitter and the receiver mainly depends on the mutual inductance and the coupling coefficient, which is affected by the geometry of coils and the distance between

them. These two factors (mutual inductance, *M*, and the distance between the coils, γ(t),) are inserted into the final equation (5.7):

$$T = \mathrm{M} \cdot \gamma_{(t)} \cdot \left\{ \frac{(V \cdot C)}{I_{\max(t)} \cdot (\alpha \cdot D) + I_{\min(t)} \cdot [\beta \cdot (1 - \eta \cdot D)]} \right\} \tag{5.7}$$

Consecutively, circuit-level simulations are performed to determine whether DPCS can be successfully integrated into a wireless power-transfer system by using a CMOS 65nm process. A simulation model of the DPCS system with wireless-power-transfer is shown in Figure 5.17, where the antenna of WPT is chosen with a self-inductance of 1µH and a resonance capacitor of 8pF. The coupling frequency is around 60 kHz. The same battery model is used in the WPT charging simulations.

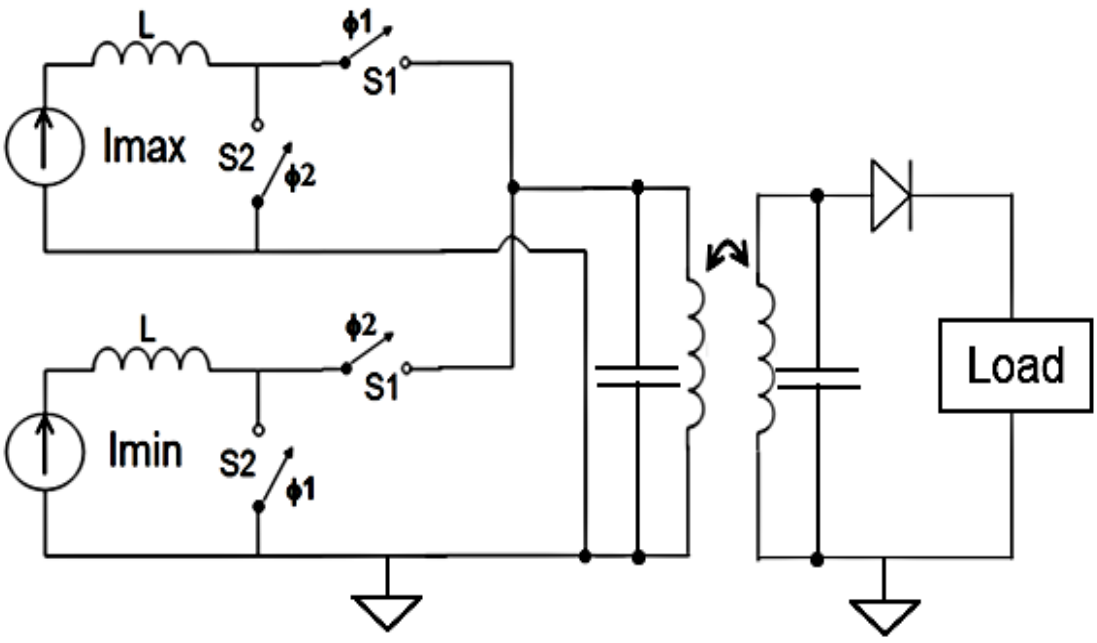

Figure 5-17: DPCS wireless power-transfer system model.

The simulation results are captured around 10s, as shown in Figure 5.18 for DPCS and PCS when I_{max} is 400mA and I_{min} is 20mA. Duty cycle is 50% and clock period is 20ms. As the simulation result shows, DPCS integrated WPT system is charging 5% more compared to PCS integrated WPT; hence, it will charge the battery faster.

Compared to earlier simulations, battery voltage in WPT will take longer to charge due to weak coupling coefficient between the coils. Coupling coefficient may vary for loosely couple systems and in this study; it is selected as 0.5.

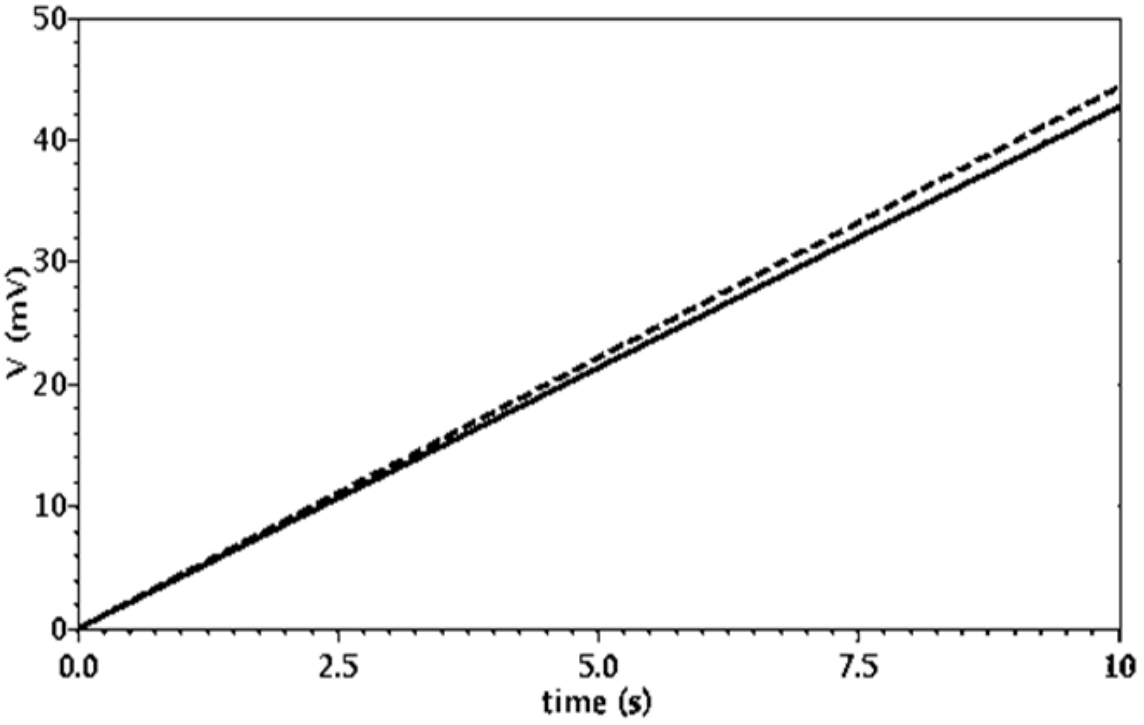

Figure 5-18: Comparison of DPCS (dashed) vs PCS in WPT system.

5.8 Discussion

A new method called a double pulse charging [37-38] system is proposed. DPCS offers good trade-off between PCS and CC systems to improve battery life. The effects of pulse

charging on the cycling characteristics of Li-ion batteries are well studied and summarized in [32] [33] [34]. PCS keeps battery impedance close to fresh batteries and has a better charge-recharge cycle characteristic—about 15% more than that of the CC system with a charging current of 500mA-1A. For instance, the CC system is shown to provide 1Ah with 600 cycles, whereas PCS provides 1.15Ah with 600 cycles in lab experiments [31] [33]. This performance improvement in cycle life comes with a charge-time penalty and the proposed DPCS system helps to improve charging speed. The chemical and longevity experiments are out of scope of this work. However, based on the comparison of CC and PCS systems, it is expected that DPCS will stay less than 15% of capacity improvement and between 1Ah to 1.15Ah for 600 cycles depending on the programmability options shown in Section IV.

The proposed method is also integrated into a wireless power-transfer system. DPCS offers a robust compromise between longevity of battery life and faster charging time; hence, it provides efficient, improved, and faster battery charging compared to PCS. Novel design techniques such as multi-level current pulses, both during charge and idle phases, programmable clock periods; and variable pulse widths are also studied. These improvements will give greater flexibility and ensure automated system control in future mobile applications and in other electronic devices that use wireless power transfer.

6 Class-E Amplifier and Unit Antenna Design for Wireless Power Transfer

6.1 Complementary Class-E Amplifier for Wireless Power Transfer

6.1.1 Power Amplifiers

Amplifiers are one of the fundamental groups of elements in circuit design that work on the principle of producing high power levels to drive output devices, antennas, or loads. Power amplifiers usually consists of a signal pick-up transducer, followed by a small signal amplifier, a large signal amplifier, and an output transducer. The main interests of these circuits are the maximum power-handling capacity, power efficiency, and impedance matching to the output device.

The power transistors may be categorized as the transistors that can handle more than 1Amp of collector (or drain current). They are fabricated a little differently than the regular signal transistors, as stated below.

1. The base is thicker to handle a large amount of current.
2. The collector (or drain) region is made larger to dissipate the heat that may develop during the operation.
3. The emitter and base layer are heavily doped.

Power amplifiers can be divided in three main categories:

1. DC Amplifiers are used to drive motors and different types of actuators.
2. Audio-power amplifiers raise the power levels of audio-frequency range (20 Hz- 20 kHz) signals from less than a watt to several hundred watts.

3. Radio-power amplifiers are used to amplify a specific or narrow band of radio frequencies while rejecting all other frequencies. They may raise the power levels to several thousand watts.

6.1.2 Classification of Power Amplifiers

According to Sokal [34], power amplifiers can be classified into three categories as below:

1. The linear class includes A, B, C, and F1. The transistor is a current source; AC current and AC voltage are proportional to the AC input-drive voltage of V_{input}. Transistor's on-voltage does not saturate.
2. The switching class includes D, E, F2, F3, and S. The transistor operates as a switch in on/off conditions. The transistor's "on" voltage saturates towards zero.
3. The mixed-mode class includes linear B and C. The operation of the transistor is the combination of both linear and switching class amplifiers.

6.1.3 Class-E Amplifiers

A typical class-E power amplifier (PA) is shown in Figure 6.1. It consists of a single-pole switch, a matching network, and a load. The matching network and the load can change based on the overall system requirements. The inductor, called an RF choke, provides a constant current from V_{DD}, and it is assumed that it has no series resistance.

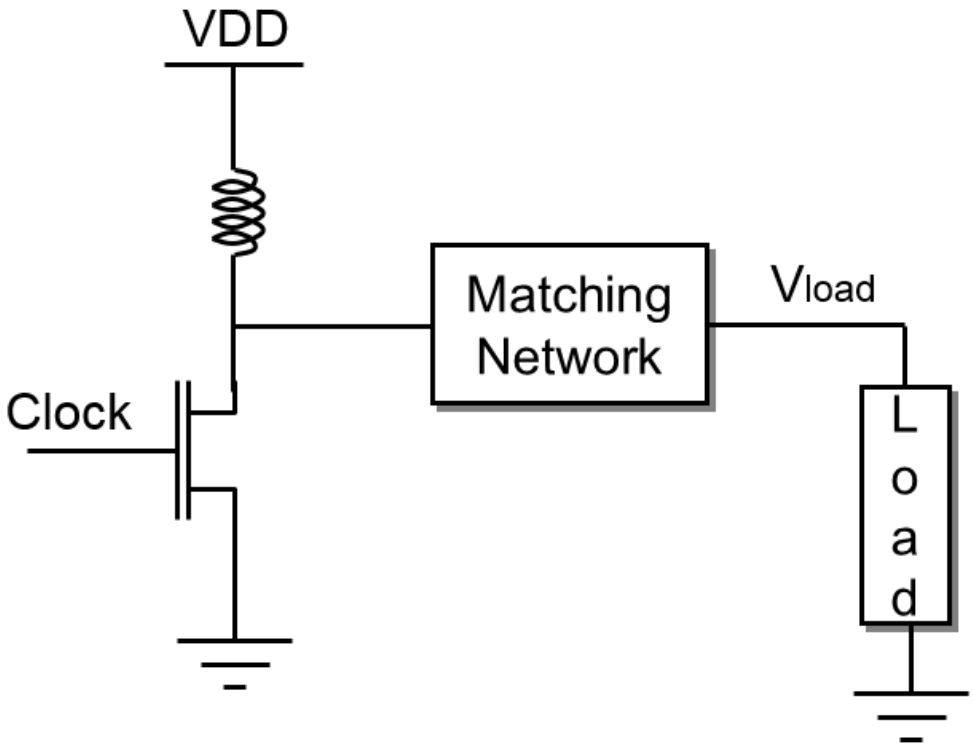

Figure 6-1: Typical Class-E amplifier

Furthermore, the shunt capacitor C_m in Figure 6.2 is used to ensure zero-voltage switching for the transistor where the switching is assumed to be lossless (zero saturation voltage, zero saturation resistance, infinite off resistance) and instantaneous. Together, RLC circuitry creates a resonance condition to provide constant current from the supply while converting the digital signal into a sinusoidal output with a zero DC offset.

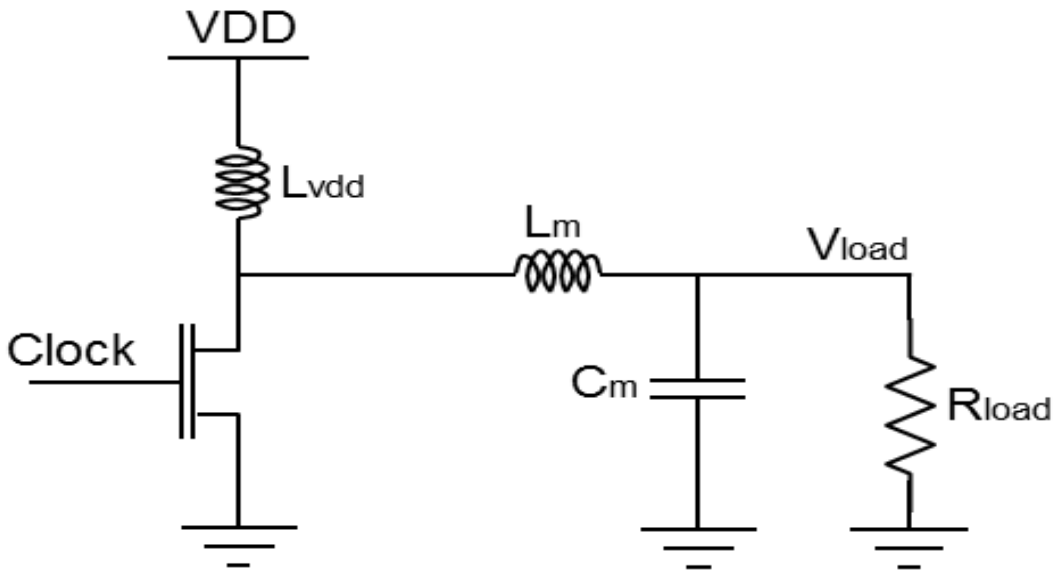

Figure 6-2: Single ended Class-E amplifier

In Class-E amplifiers, efficiency is maximized by minimizing power dissipation while still providing a desired output voltage. Unquestionably, a transistor should able to sustain high voltage over one part of an RF period, while it should able to conduct high current over another part of an RF period. In a Class-E amplifier, the circuit is designed such that high voltage and high current stages do not exist at the same time, so that, for a given time frame, the power consumption of the transistor is very low. This concept is shown in Figure 6.3.

During the ON state, the voltage is nearly zero when high current is conducting.

During the OFF state, the current is zero when there is high voltage across the transistor.

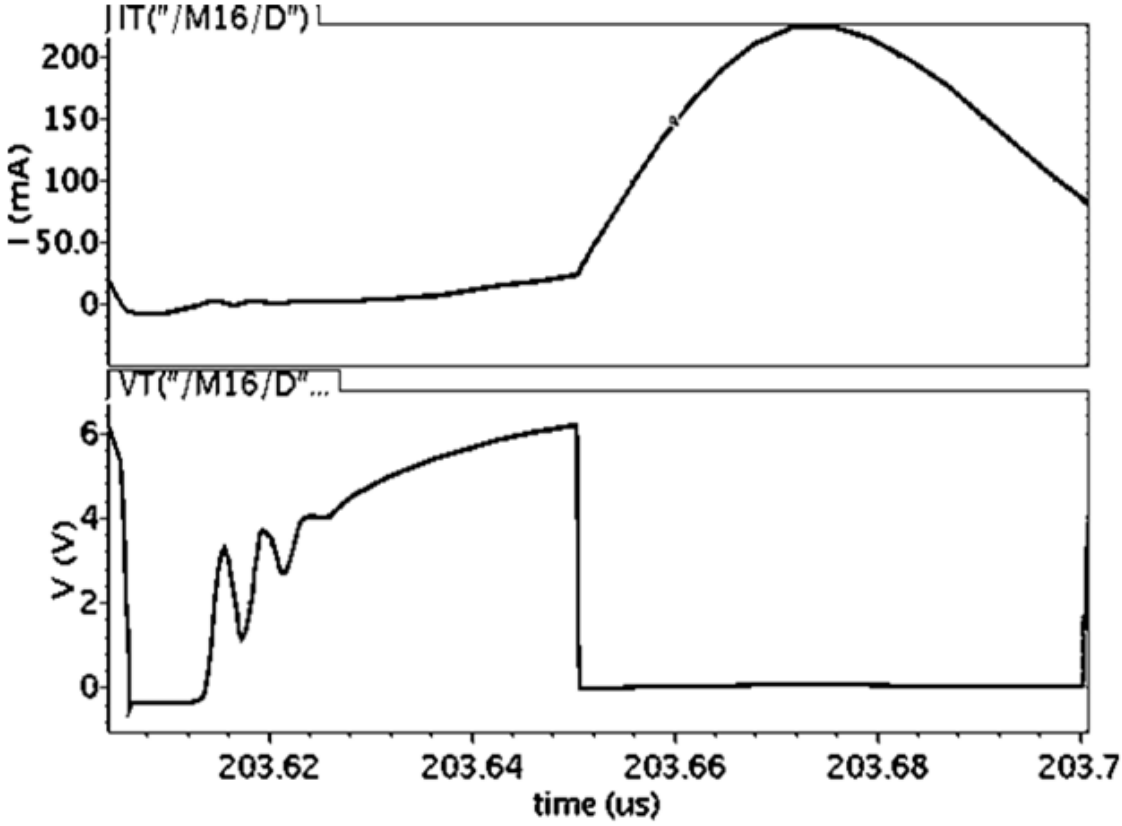

Figure 6-3: Current (upper) and voltage (lower) waveforms of the switching device

In particular, the single-ended, Class-E amplifier depicted in Figure 6.3 is simulated in Cadence. In this circuit, the matching network is designed as a simple LC filter, in which an inductor is connected between the load and the switching device in series. Afterward, a capacitor is connected after the inductor and it is in parallel with the load.

In Class-E amplifiers, the input device is designed not only to provide a large amount of currents to the load, but also to switch more quickly depending on the frequency of the signal. Due to large current requirements, the size of the switching transistor is usually made as large as possible. As a result, the large switches have small on-resistances. On the

other hand, it is not possible to make the switches infinitely large due to the unwanted contribution of parasitic circuit elements, so the optimum point should be chosen. Circuit elements and their values for the single-ended, Class-E amplifier in Figure 6.3 are summarized in Table 6-1.

Table 6-1: Circuit parameters of single-ended, Class-E amplifier

Definition	**Values**
Switching Frequency	13.56 MHz
Matching Capacitor (C_m)	0.275 nF
Matching Inductor (L_m)	0.5 µH
Load Impedance (R_{load})	50 Ω, 100Ω
Supply Inductor (L_{vdd})	30 µH
V_{load} (Vpp)	6 V@ 50Ω, 12V at 100Ω
Power Supply (Vdd)	2 V
Switch Dimension (W/L)	40µm / 0.06µm
Number of Unit Switches	30

Simulations are performed to show the amplitude of output signal at the load vs. the number of unit switch devices in the amplifier of the transmitter. The unit size of the switch is designed to be 40µm/0.06µm. As shown in Figure 6.4, the multiplier value of the switch is varied from 1 to 200 in steps of 20, and the simulations are completed for load resistances of 50Ω and 100Ω. The signal amplitude is at its maximum of 6V and 12V for 50Ω- and

100Ω-load resistances, respectively, and the number of unit devices is around 30. After this point, there is not much improvement, due to parasitic effects of the semiconductor devices.

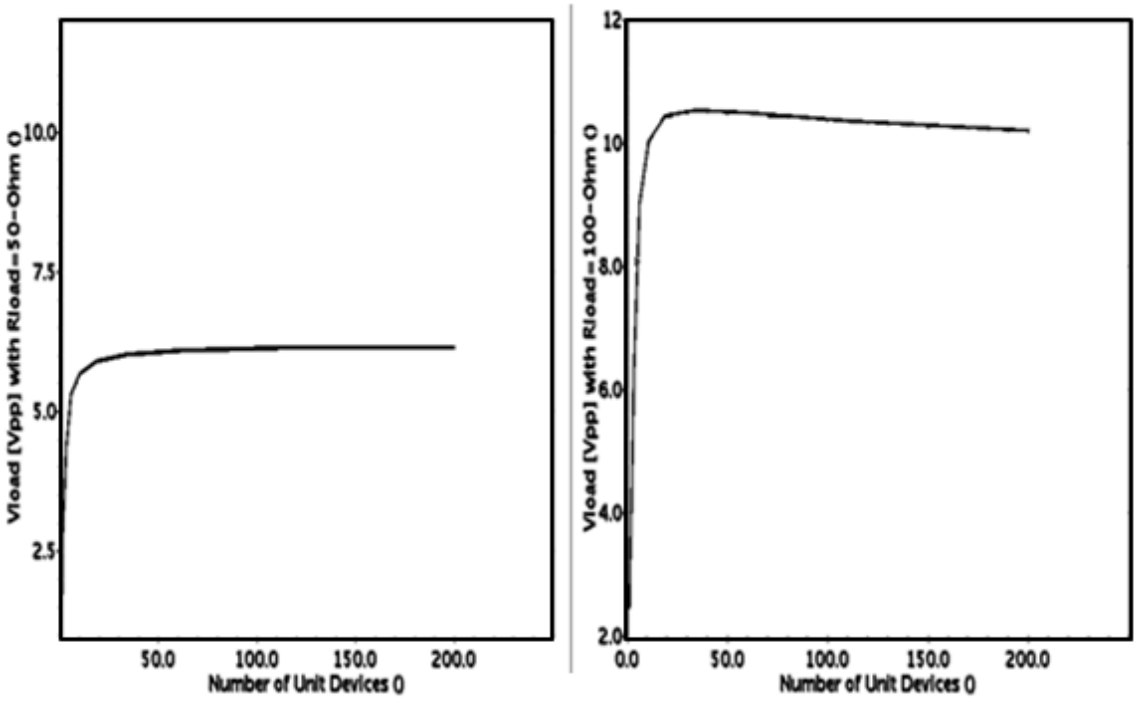

Figure 6-4: Output voltage of single-ended Class-E amplifier with R_{load}=50Ω(left) and R_{load}=100Ω (right)

When the switching transistor in Figure 6.4 is turned on, magnetic flux occurs on the RF–choke inductor, which is connected to V_{dd}. This energy stored in the inductor in the form of current is propagated to the load when the switch is off. Specifically, the power transferred to the load can be increased significantly with an LC network in between. This filter circuit is needed to remove higher-order harmonics. The output signal resonating at 13.56MHz is shown in Figure 6.5.

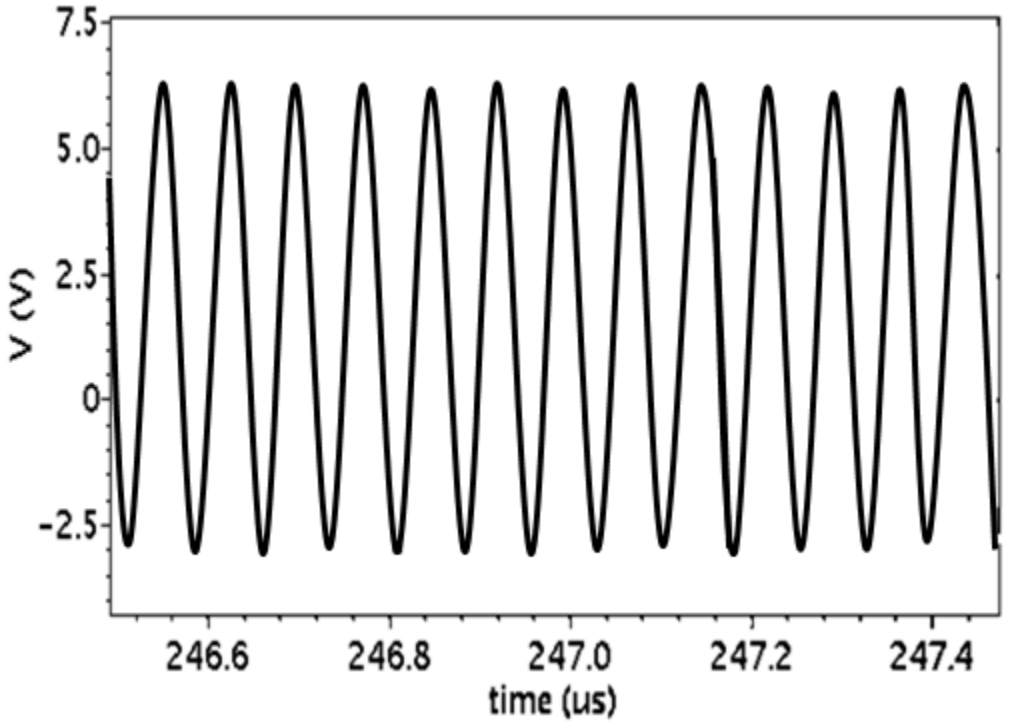

Figure 6-5: Output voltage of Class-E amplifier at the load (50Ω)

6.1.4 13.56 MHz WPTS with Single-ended Class-E Amplifier

Finally, parallel compensated (both primary and secondary) wireless power-transfer system with a single-ended Class-E amplifier in Figure 6.6 is simulated. Similarly, the dimension of the main switch element is chosen to be the same as that of the single-ended Class-E amplifier. The rest of the circuit elements are summarized in Table 6-2. This is a loosely coupled WPTS with a coupling coefficient of 0.01.

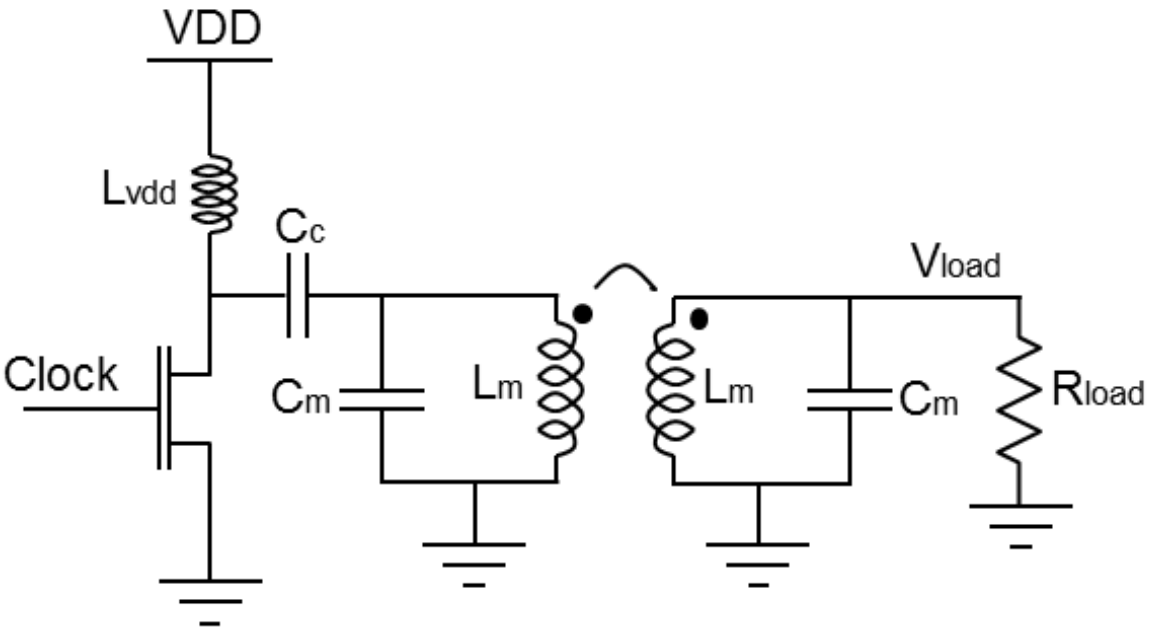

Figure 6-6: Single-ended Class-E amplifier with WPTS

Table 6-2: Circuit parameters of WPTS

Definition/Parameters	**Values**
Resonant Frequency (F_r)	13.56 MHz
Transmitter/Receiver Capacitor (C_m)	0.275 nF
Transmitter/Receiver Inductance (L_m)	0.5 µH
Coupling Coefficient (k)	0.01
Matching Capacitor (C_c)	10 pF
Load Impedance (R_{load})	50 Ω

Simulation results of transmitted and received signals are shown in Figure 6.7. The received signal amplitude is about 62.16 mVpp.

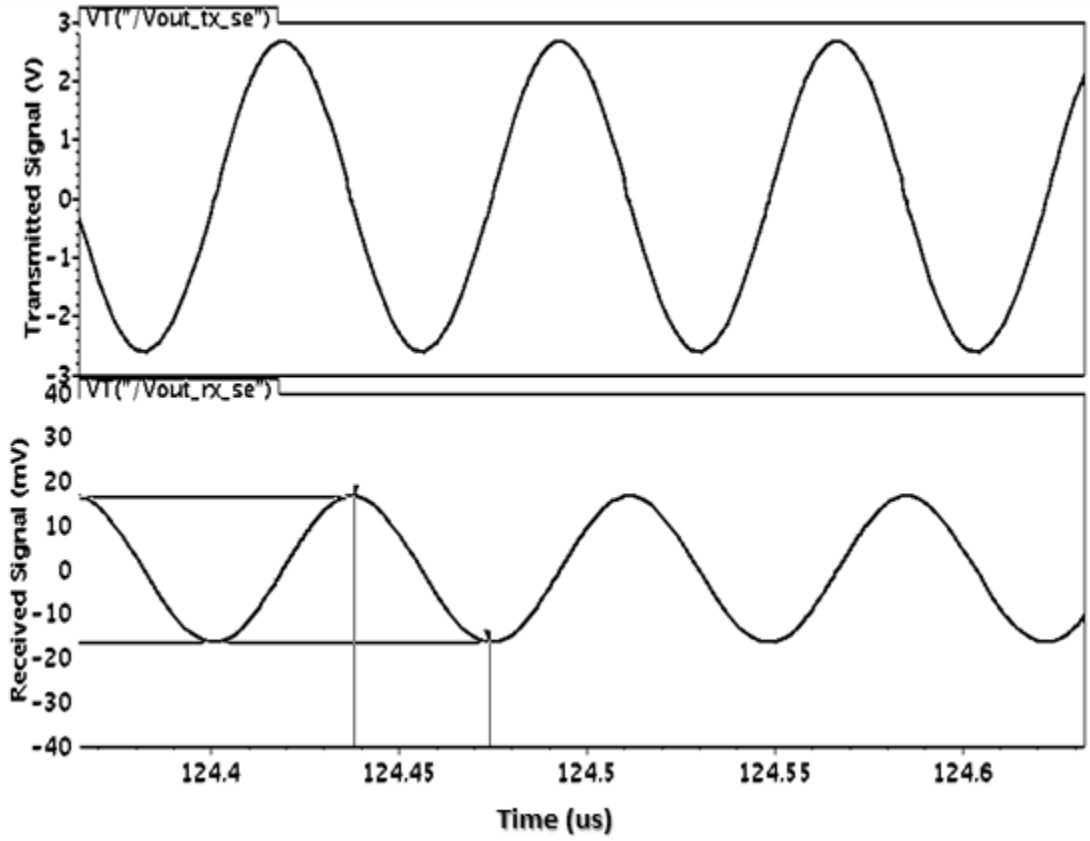

Figure 6-7: Transmitted signal (upper) and received signal (lower)

6.1.5 Complementary Class-E Amplifier for WPTS

The proposed WPTS is shown in Figure 6.8 for the final analysis. In this model, the complementary stage of Class-E amplifier is added to the previous structure. The circuitry in the dashed box is the complementary stage, which is active in alternating phase compared to the circuitry out of the dashed box. Basically, this complementary part of the whole system can be enabled by using a pass-gate controlled EN logic signal. On the other

hand, the single-ended architecture can be activated by an EN_b logic signal. When EN_b is active and high, the gate of the complementary main switching transistor inside the dashed box is pulled low and hence is disabled. At the same time, the bottom terminal of the lower coil is also shorted to ground by a shunt pass-gate. This second pass-gate disables the complementary coil. Potentially, this WPTS can work either in low-power mode (single-ended) or high-power mode (complementary).

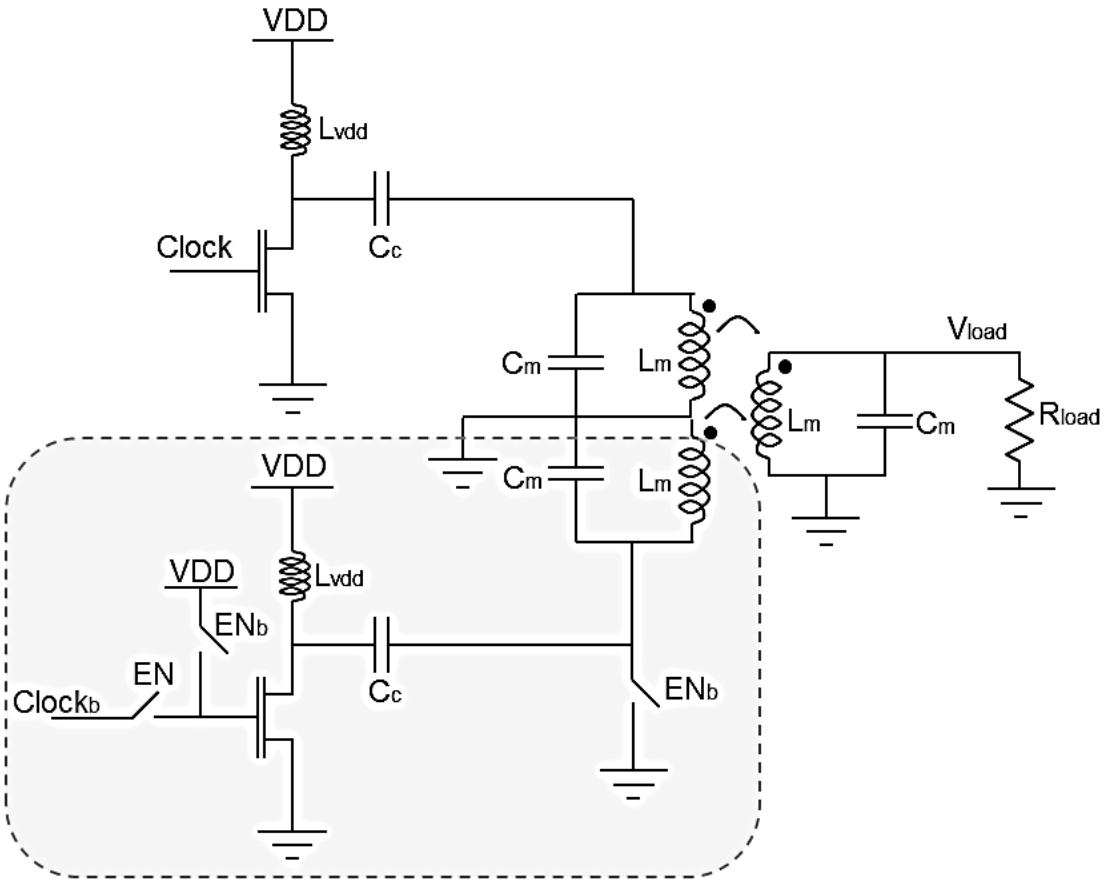

Figure 6-8: Proposed Class-E WPTS model

A complementary structure is simulated, and its resulting waveforms are shown in Figure 6.9. By using this full architecture, the received signal amplitude is doubled, as seen in Table 6.3.The transmitted signal from each coil of the complementary Class-E WPTS architecture is still the same as that of the single-ended Class-E WPTS. At the same time, the final signal amplitude of the differential signal at the transmitter coils is 12Vpp.

Table 6-3: Transmitted and received signal values in two architectures

Circuit	**Transmitted Signal [V]**	**Received Signal [mV]**
Single Ended Class-E	6	62.2
Complementary Class-E	6	123.3

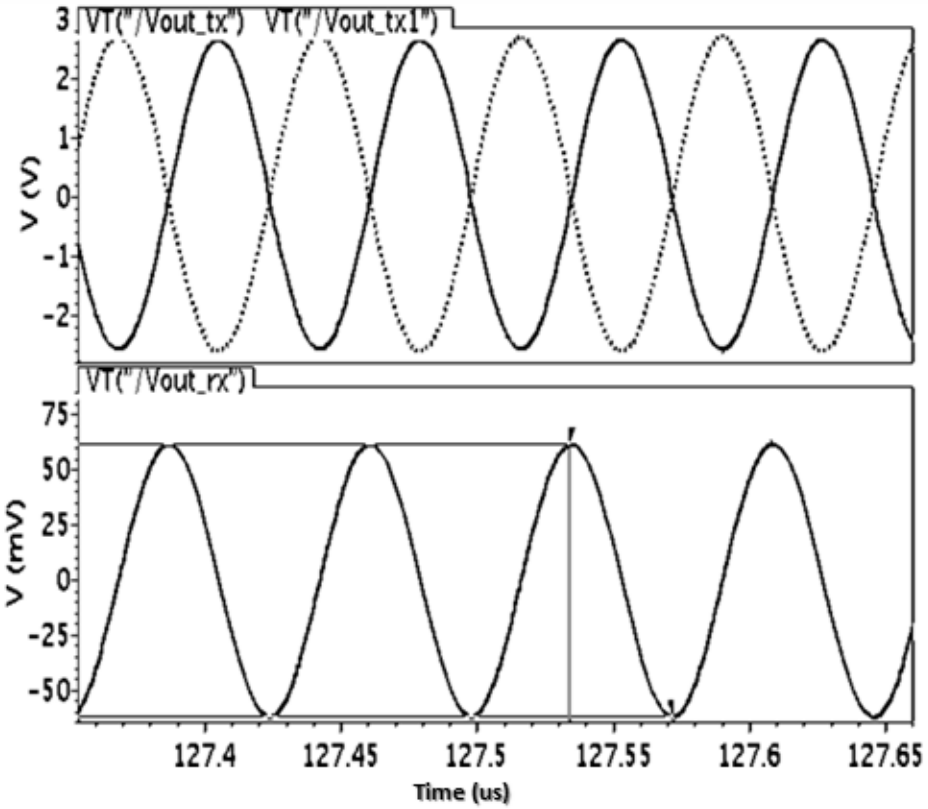

Figure 6-9: Transmitted (upper) and received (lower) signals in proposed system

6.1.6 Discussion

A new method [39] is proposed to improve power transfer between the transmitter and receiver of a WPTS. The proposed method dynamically changes the configuration of Class-E power amplifiers based on the power needs of the system. This architecture can be used to increase the flexibility of reconfigurable paths and to ensure automated system control. This technique will also reduce the power consumption of the circuit elements when the receiver is close and has a good power link with the transmitter.

6.2 Unit Antenna based Wireless Power Transfer

6.2.1 Introduction

One of the requirements for robust wireless power transfer is a system that can quickly recover from any side effects of misplacement of the antennas. Most of the power is transferred when the resonance happens between the transmitting and receiving antennas. Antenna arrays on either side can help with this issue.

6.2.2 Baseline System Simulations

An ideal (without any resistive losses) parallel compensated WPTS in Figure 6.10 is simulated under no-load conditions.

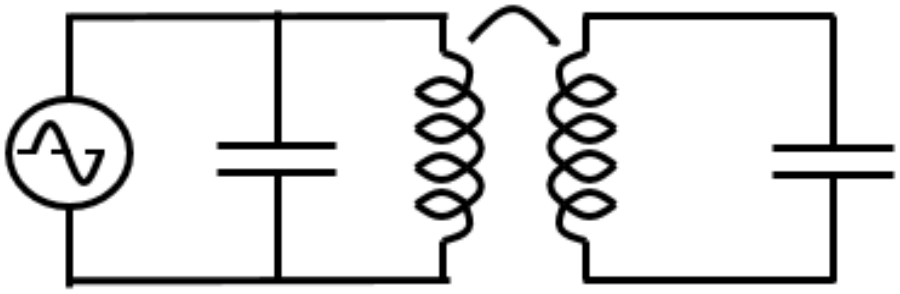

Figure 6-10: Parallel compensated WPT system

Simulated transmitted and received signals are shown in Figure 6.11. This system is designed to resonate at 13.56MHz. Circuit elements are chosen for mobile applications so that sizes of both antennas and compensation capacitors are widely available using discrete components. Circuit parameter values are shown in Table 6-4.

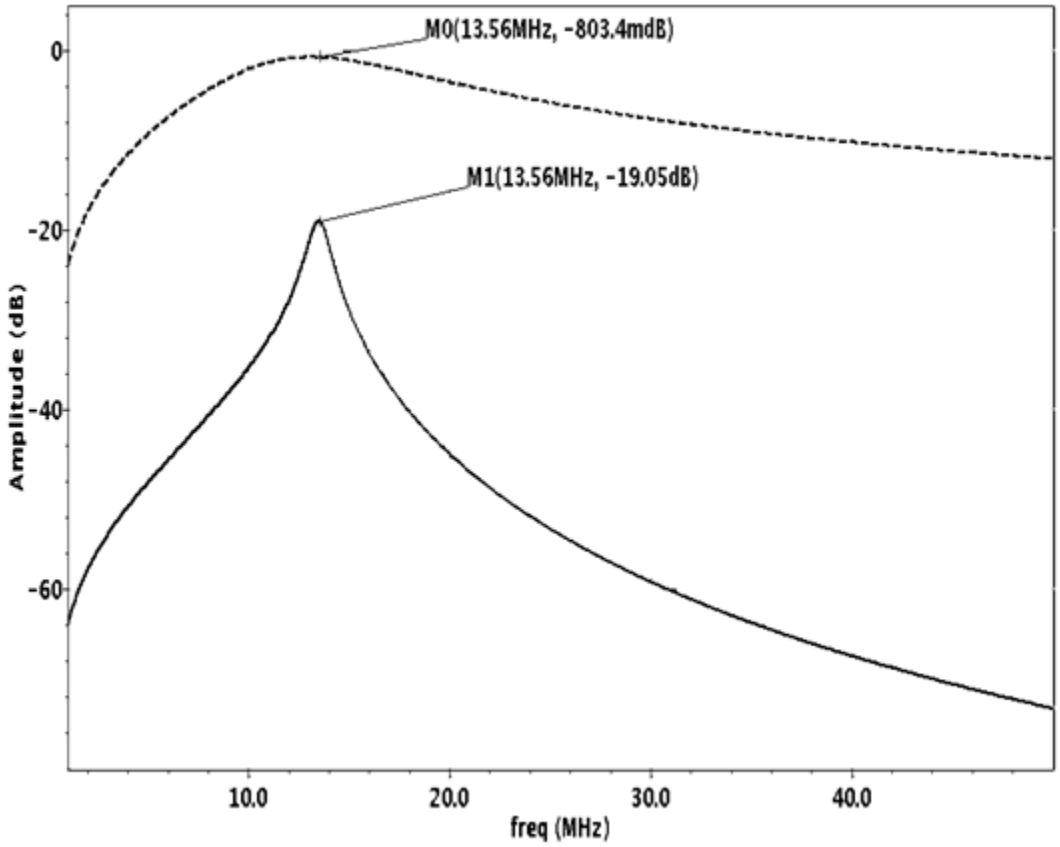

Figure 6-11: Transmitted signal (dashed) and received signal (solid)

Table 6-4: Circuit Parameters

Definitions/Parameters	**Values**
Resonant Frequency (F_r)	13.56 MHz
Primary Capacitor (C_P)	0.335 nF
Unit Primary Inductance (L_p)	0.5 µH
Secondary Capacitance (C_s)	0.335 nF
Secondary Inductance (L_s)	0.5 µH
Coupling Coefficient (k)	0.01
Primary Excitation Voltage (V_p)	1 V

6.2.3 Proposed Tuning Structure

In this study, we propose a unit antenna array-based antenna structure as shown in Figure 6.12 to provide easy tuning and enhancement for a WPTS.

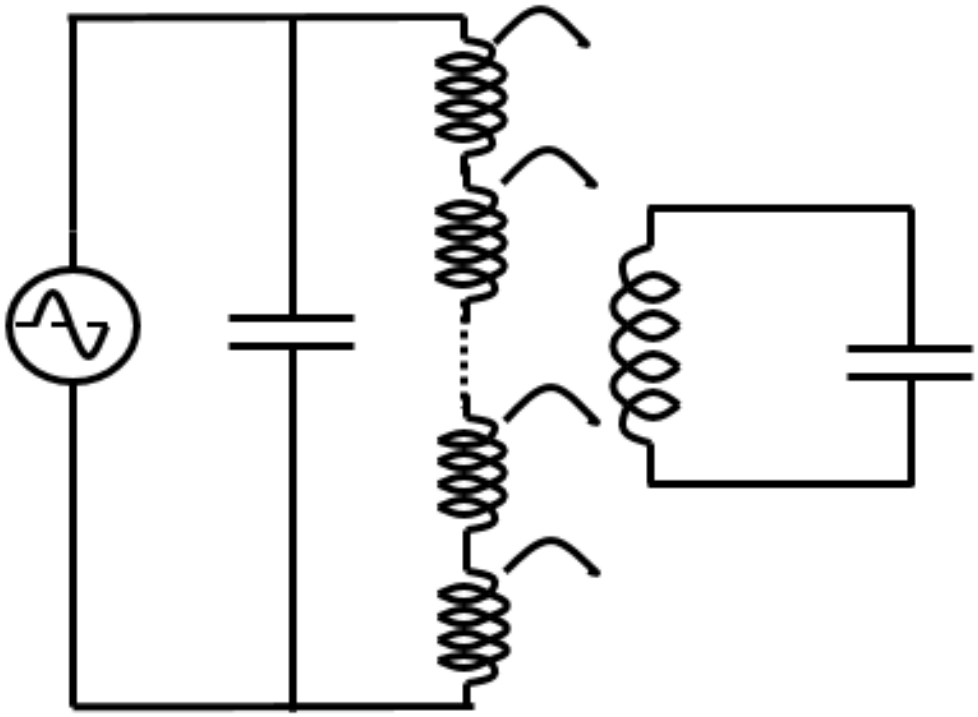

Figure 6-12: Unit antenna array based transmitter

Detuning may happen due to distance between the receiver and transmitter, the orientation of the antennas relative to each other, environmental effects, and component mismatches. In our simulations, detuning is emulated by creating a mismatch between the compensation capacitors of the transmitter and receiver. Figure 6.13 shows two different transmit signals: one is tuned to 13.56 MHz, and the other is out of resonance. With a detuned signal, the amplitude is dropped about 1.5dB and the peak resonance is shifted away from 13.56MHz.

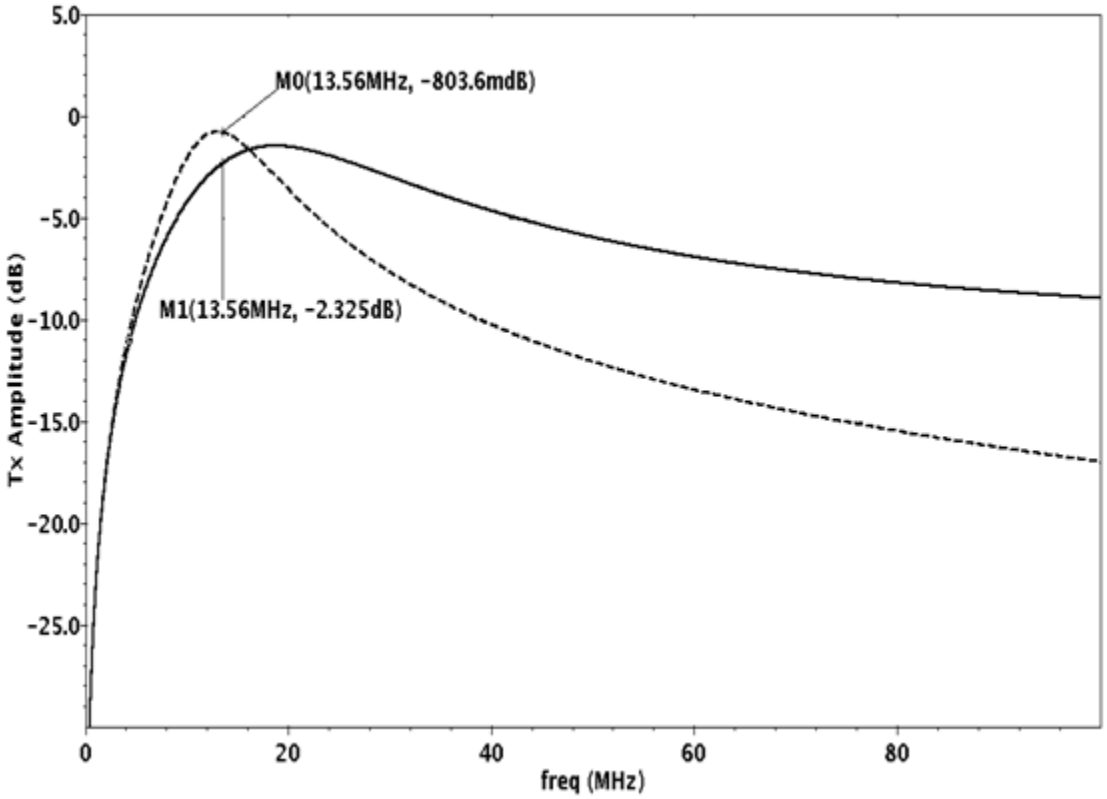

Figure 6-13: Transmitted signals, tuned (dashed), de-tuned (solid)

The effects of a detuned transmitter on the receiver are shown in Figure 6.14. The amplitude of the received signal dropped by 1.5dB.

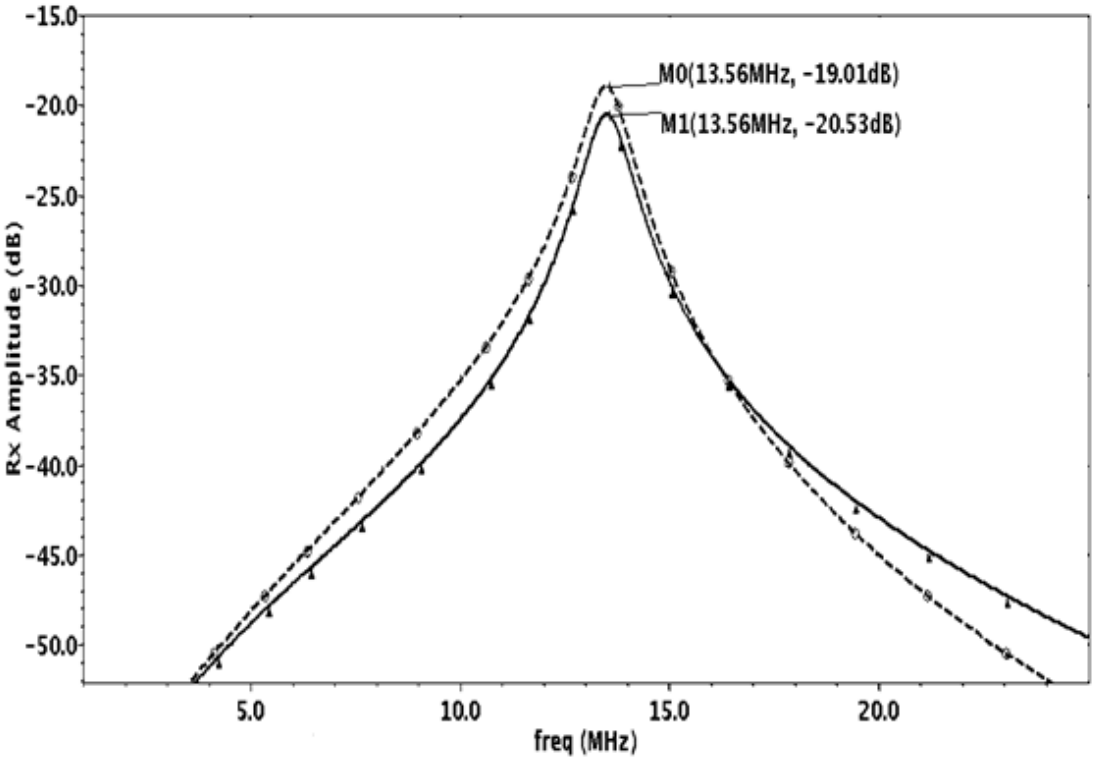

Figure 6-14: Received signals, tuned (dashed), de-tuned (solid)

To re-tune the system, an array of unit antennas are used in the proposed system so that the individuals units can be added to or removed from the primary. Afterwards, two different unit arrays are simulated and compared. The first structure is based on the unit antenna value of 0.125μH, and the second structure is based on the unit antenna value of 0.250μH. In both simulations, extra antenna elements are added to compensate for the detuning. Even though the first structure may provide better granularity in tuning due to a smaller inductor value, it may take extra space and may not be possible for compact applications. The circuit elements of these two structures are shown in Table 6.5. One thing to note is that when unit antenna size is decreased, mutual inductance is scaled down accordingly based on (4).

Table 6-5: Values of circuit parameters for proposed transmitter structures

Circuit	Tx Cap [nF]	Antenna [µH]	Number of Unit Antennas	Rx Signal [dB]
Baseline	0.335	0.5	1	-19.01
Detuned Structure	0.165	0.5	1	-20.53
Structure-1	0.165	0.125	6	-19.32
Structure-2	0.165	0.250	3	-19.32

Structures with different unit antenna sizes are simulated and compared to that of the ideal case and detuned structure. Figure 6.15 shows the amplitude of received signals in the frequency domain. Amplitude is improved and almost matches the ideal case with a 0.3dB difference.

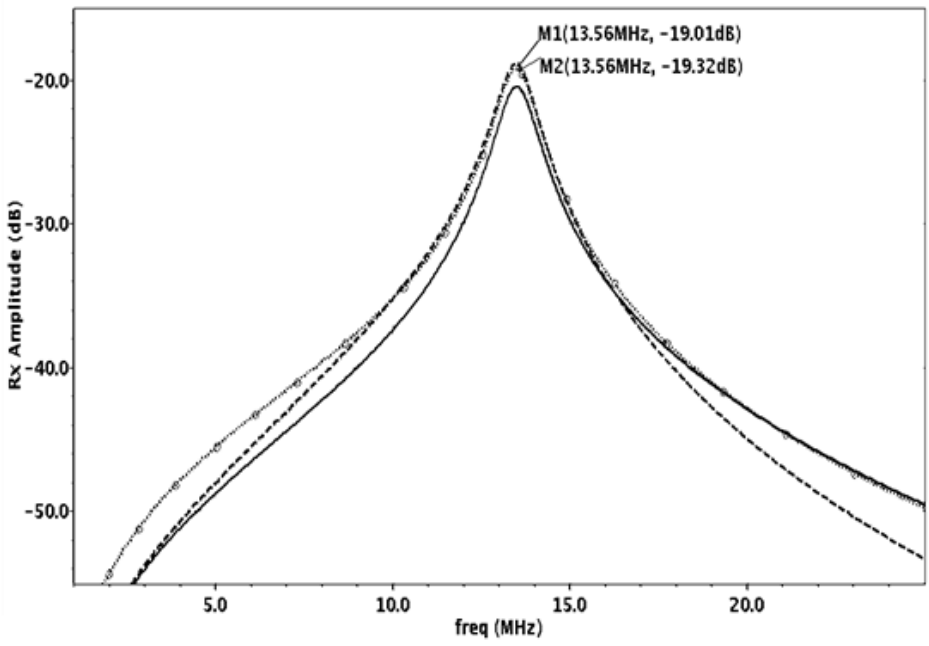

Figure 6-15: Received signals, tuned (dashed), de-tuned (solid/lowest), re-tuned with proposed structure (dotted/diagonal)

The same structure is also proposed for the receiver side. In this particular simulation, the receiver antenna is assumed to be mismatched from the transmitter antenna by 0.1 µH, and its value is simulated as 0.4 µH. To compensate for the mismatch, a unit antenna of 0.125µH is used in the receiver, as shown in Figure 6.16.

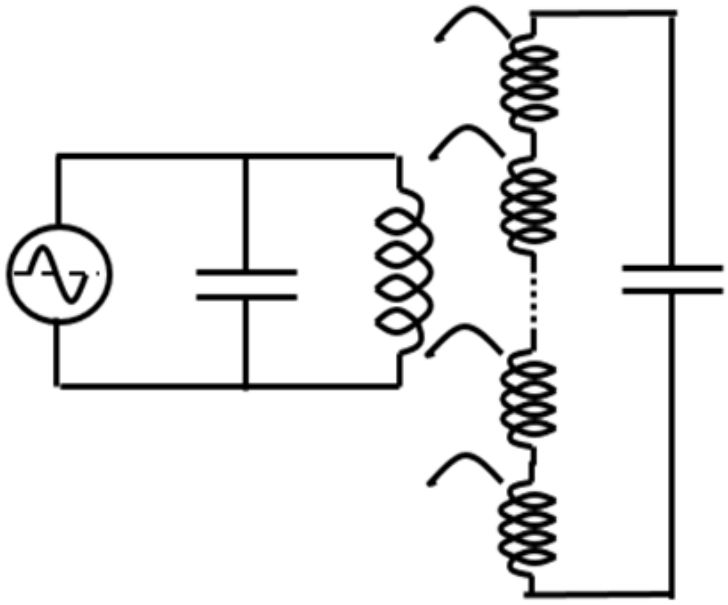

Figure 6-16: Unit antenna array based receiver structure

Table 6-6: Comparison of result from different system structures

Circuit	Antenna [µH]	Unit Antenna [µH]	Rx Signal [dB]
Baseline	0.5	----	-19.01
Detuned Structure	0.4	----	-29.09
Structure-1	0.4	0.125	-20.31

Simulation results in Figure 6.17 show that the resonance of the calibrated system is shifted back close to its ideal resonance frequency of 13.56MH. Considering original resonance

frequencies, the received signal amplitude of the tuned system is about 1.3dB lower than that of ideal value; at the same time, it is much better than that of detuned system (by 10 dB).

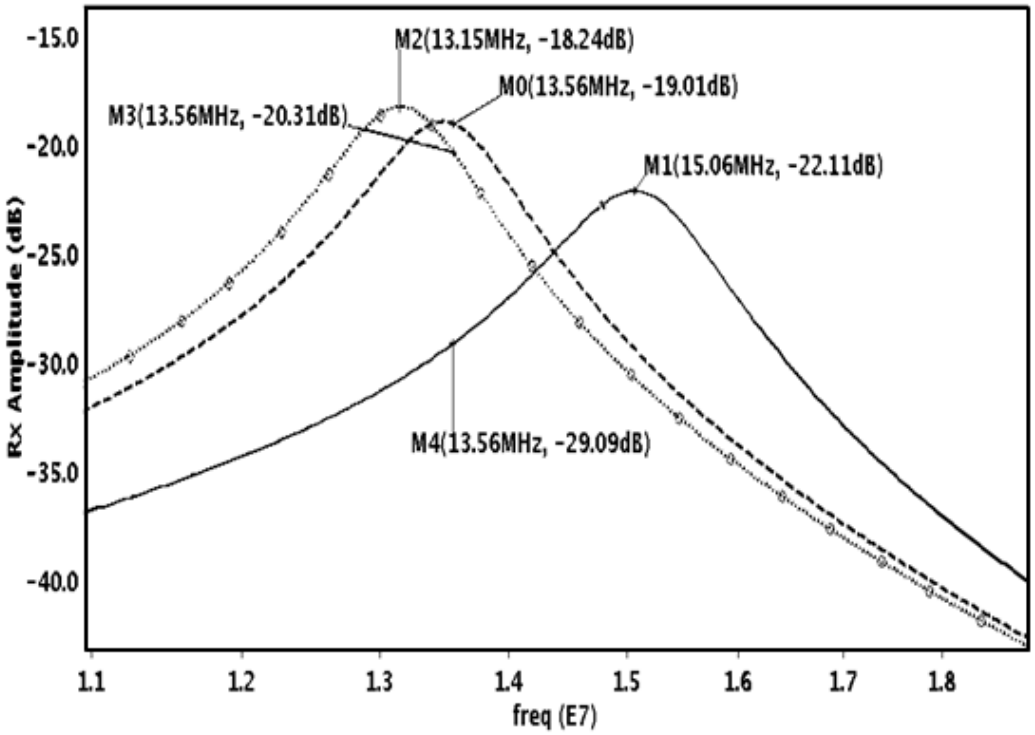

Figure 6-17: Received signals, tuned (dashed), de-tuned (solid), re-tuned with proposed structure (dotted/diamond)

6.3 Discussion

In this section, a unit antenna-based WPT system [40] for a tunable antenna system is presented. It is successfully demonstrated that the proposed structure can provide compensation when the system is out of tune from the desired resonant frequency. These structures enable designers to optimize both transmitters and receivers by connecting/disconnecting a certain number of unit antenna elements. The proposed method can be used for multi-frequency tuning for different receivers.

7 Summary and Concluding Remarks

Wireless power transfer, especially resonant inductive coupling, has started to penetrate into our daily lives. This technology would be very beneficial for extending portable consumer electronics into the energy domain and hence cutting the last wires/cables needed for electronic devices. The research in WPT has been extremely productive in recent years. Mobile phones have already started to use WPT, and automotive technology is the next big consumer market to embrace this trend.

With this increased enablement of the technology, new challenges and research topics are opened up. Specifically, the efficiency of power transfer, the tuning of the WPT system, and health risks associated with its implementation are few of these important research areas.

In this dissertation, improved tuning techniques are proposed for WPT system such as hybrid capacitive tuning, unit antenna tuning, and complementary Class-E amplification stages. The study explores a new technique for battery charging.

These techniques are simulated and have proven to be effective to improve tuning range of the WPT system at the RF front-end. In particular, the hybrid capacitor architecture for WPT resonance tuning is tested by using discrete IC and passive components. Test results also show improved results and the feasibility of good tuning between transmitter and receiver of WPT system.

Proposed methods may stimulate new architectures and future research in the WPT area. This will further improve electronic systems and facilitate faster, more efficient, and robust power transfers.

Bibliography

[1] C. Capps. (2001). *Near Field or far field?* [Online].
Available: https://people.eecs.ku.edu/~callen/501/Capps2001EDNpp95.pdf.

[2] O. H. Stielau and G. A. Covic, “Design of loosely coupled inductive power transfer systems,” in *Proc. IEEE 2000 International Conf. on Power System Technology*, Australia, 4-7 Dec., 2000, pp.85-90.

[3] Riehl, P. S.; Satyamoorthy, A.; Akram, H.; Yen, Y.-C.; Yang, J.C.; Juan, B.; Lee, C.-M.; Lin, F.-C.; Muratov, V.; Plumb, W.; Tustin, P.-F.; “Wireless Power Systems for Mobile Devices Supporting Inductive and Resonant Operating Modes,” *IEEE Tran. On Microwave Theory and Techniques*, vol. 63, no. 3, pp. 780-790, Mar. 2015.

[4] Y. Lim, H. Tang, S. Lim and J. Park, "An adaptive Impedance-Matching Network Based-on a Novel Capacitor Matrix for Wireless Power Transfer," *IEEE Trans. on Power Electronics*, vol. 29, no. 8, pp. 4403-4413, Aug. 2014.

[5] W. Zhou and H. Ma, "Design considerations of compensation topologies in icpt system, " in *Proc. IEEE Applied Power Electronics Conference*, Anaheim, CA, 2007, pp. 985-990.

[6] K. Okada, K. Limura, N. Hoshi and J. Haruna, "Comparison of Two Kinds of Compensation Schemes on Inductive Power Transfer Systems for Electric Vehicle," in Proc. *IEEE Vehicle Power and Propulsion Conf.*, Seoul, Korea, 2012, pp. 766-771.

[7] R. Jegadeesan and Y. -X. Guo, "Toplogy selection and efficiency improvement of inductive power links," *IEEE Trans. on Antennas and Propagation*, vol. 60, no. 10, pp. 4846-4854, Oct. 2012.

[8] K. Ogawa, N. Oodachi, S. Obayashi and H. Shoki, "A study of efficiency improvement of wireless power transfer by impedance matching," in *Proc. IEEE MTT-S International Microwave Workshop on Innovative Wireless Power Transmission*, Kyoto, Japan, 2012, pp. 155-157.

[9] P. P. Mercier and A. Chandrakasan, "Rapid Wireless Capacitor Charging uisng a Multi-Tapped Inductively Coupled Secondary Coil," *IEEE Trans. on Circuits and Syst. I, Reg. Papers*, vol. 60, no. 9, pp. 2263-2272, Sep. 2013.

[10] Y. K. Jung and B. Lee, "Design of adaptive optimal load circuit for maximum wireless power transfer efficiency," in *Proc. Asia-Pacific Microwave Conference*, Seoul, Korea, 2013, pp. 1221-1223.

[11] H. -M. Lee, K. -Y. Kwon, W. Li and M. Ghovanloo, "A power efficient switched-capacitor stimulating system for electrical/optical deep brain stimulation," *IEEE J. Solid-State Circuits*, vol. 50, no. 1, pp. 360-374, Jan. 2015.

[12] J. Lee, Y. -S. Lim, W. -J. Yang and S. -O. Lim, "Wireless power transfer system adaptive to change in coil separation," *IEEE Trans. on Antennas and Propagation*, vol. 62, no. 2, pp. 889-897, Feb. 2014.

[13] J. D. Heebl, E. M. Thomas, R. P. Penno and A. Grbic, "Comprehensive Analysis and Measurement of Frequency-Tuned and Impedance-Tuned Wireless Non Radiative Power Transfer Systems," *IEEE Antennas and Propagation Magazine*, vol. 56, no. 5, pp. 131-148, Oct. 2014.

[14] K. Buisman, C. Huang, A. Akhnoukh, M. Marchetti, L.C.N. de Vreede, L.E. Larson, and L.K. Nanver, "Varactor Topologies for RF adaptivity with improved power handling and linearity," in *Proc. IEEE/MTT-S Internationsl Microw. Symp.*, Honolulu, Hawaii, 2007, pp. 319-322.

[15] K. Buisman, C. Huang, P. J. Zampardi and L. de Vreede, "RF Power Insentive Varactors," *IEEE Microw. Wireless Comp. Lett.*, vol. 22, no, 8, pp. 418-420, Aug. 2012.

[16] C. C. Hu, "MOS Capacitor," in *Modern Semidconductor Devices for Integrated Circuits*, Prentice Hall, 2009, ch. 5, pp. 157-193.

[17] N. Keskin and H. Liu, “Tuning of a wireless power transfer system with a hybrid capacitor array,” *The Cambridge Journals on Wireless Power Transfer*, vol. 3, no. 1, pp. 9-14, , Mar. 2016.

[18] A. P. Sample, B. H. Waters, S. T. Wisdom and J. R. Smith, "Enabling seamless wireless power delivery in dynamic environment," in *IEEE Proceedings*, vol. 101, no. 6, pp. 1343-1358, Jun. 2013.

[19] X. Lai and F. Yuan, "Remote calibration of wireless power harvest," in *Proc. IEEE Int. Midwest Symp. on Circuits and Systems*, Columnbus, OH, 2013, pp. 501-504.

[20] R. Saltanovs, "Multi-capacitor circuit application for the wireless energy tranmission system coils resonant frequency adjustments," in Proc. *IEEE Wireless Power Transfer Conf.*, Boulder, CO, 2015, pp. 1-3.

[21] Cadex Electronics, *Battery University* [Online]. Available: http://www.batteryuniversity.com

[22] Woodback Communications ltd. (2005). *Electropedia Battery and Energy Technologies* [Online]. Available: http://www.mpoweruk.com

[23] B. Tsenter and F. Schwarzmiller, "Universal Charge Algorithm for Telecommunication Batteries," in *Proc. Battery Applications and Advances Conf.*, Long Beach, CA, 1997, pp. 233-238.

[24] R. C. Cope and Y. Podrazhansky, "The art of battery charging," in *Proc. Battery Applications and Advances Conf.*, Long Beach, CA, 1999, pp. 233-235.

[25] R. Awwad, R. Das, T. Arabi and H. Hajj, "A fast charging Multi-C technique for mobile devices," in *Proc. Energy Aware Computing Conf., Cyprus*, 2012, pp. 1-7.

[26] L. R. Chen, "A design of optimal pulse charge system by frequency varied Technique," *IEEE Trans. on Industrial Electronics*, vol. 54, no. 1, pp. 398-405, Feb. 2007.

[27] J. Zhang, J. Yu, C. Cha and H. Yang, "The effects of pulse charging on inner pressure and cycling characteristics of sealed Ni/MH batteries," *Journal of Power Sources*, vol. 136, no. 1, pp. 180-185, Sep. 2004.

[28] S. -J. Huang, F. -S. Pai and B. -G. Huang, "A matching design for ultra-capacitor and Li-Ion battery cooperation in electrical wheel motors," in *Proc. IEEE SICE Conf.*, Taipei, Taiwan, 2010, pp. 2646-2649.

[29] G. A. Rincon-More and M. Chen, "Accurate electrical battery model capable of predicting runtime and I-V performance," *IEEE Trans. on Energy Conversion*, vol. 21, no. 2, pp. 504-511, Jun. 2006.

[30] R. Carter, A. Cruden, P. J. Hall and A. S. Zaher, "An improved lead-acid battery pack model for use in power simulations of electric vechicles," *IEEE Trans. on Energy Conversion*, vol. 27, no. 1, pp. 21-28, Mar. 2012.

[31] C. Blanco, L. Sanchez, M. Gonzalez, J. C. Anton, V. Garcia and J. C. Viear, "An equivalent circuit model with variable effective capacity for LiFePO4 batteries," *IEEE Trans. on Vehicular Technology*, vol. 63, no. 8, pp. 3592-3599, Oct. 2014.

[32] J. Li, E. Murphy, J. Winnick and P. A. Kohl, "The effects of pulse charging on cycling characterisctis of commercial lithium-ion batteries," *Journal of Power Sources*, vol. 102, no. 1, pp. 302-309, Dec. 2001.

[33] B. N. Popov, P. Ramadass, B. S. Haran and R. E. White, "Capacity Fade of Li-ion cells at elevated temperautes cycled using pulse and DC charging protocols," in *Proc. Electrochemical Society Workshop*, San Francisco, CA, 2001.

[34] B. N. Popov, A. Durairajan, Y. Podrazhansky and R. C. Cope, "Capacity fade of Li-ion cells:Comparison of DC and ENREV chraging protocols," in *Proc. Applications and Advances Conf.*, Long Beach, CA, 2000, pp. 185-191.

[35] N. Jamal, S. Saat and A. Z. Shukor, "A study on performance of different compensation topologies for loosley coupled inductive power transfer systems," in *Proc. IEEE Control System, Computing and Engineering Conf.*, Penang, Malaysia, 2013, pp. 173-178.

[36] B. Peschiera and S. S. Williamson, "Review and Comparison of Inductive Charging Power Electronic Converter Topologies for Electric and Plug-in Hybrid Electric Vehicles," in *IEEE Transportation Electrification Conf.*, Detroit, MI, 2013, pp. 1-6.

[37] N. Keskin and H. Liu, “Fast Charging Method for Wireless and Mobile Devices using Double-Pulse Charge Technique,” in *Proc. IEEE Wireless Power Transfer Conference*, Jeju, Korea, 2014 pp. 44-47.

[38] N. Keskin and H. Liu, “Double-pulse charge technique for wireless and mobile devices,” *Kluwer Academics Analog Integrated Circuits and Signal Processing*, vol. 86, no. 2, pp. 299-305, Feb. 2016.

[39] N. Keskin and H. Liu, “Complementary Class-E Amplifier for Wireless Power Transfer,” in *Proc. IEEE Electronic Components and Technology Conference*, San Diego, CA, 2015, pp. 2235-2240.

[40] N. Keskin and H. Liu, “Unit Antenna Based Wireless Power Transfer Systems,” in *Proc. IEEE Electronic Components and Technology Conference* San Diego, CA , 2015, pp.1828-1833.